Faculdade de Engenharia da Universidade do Porto
Instituto de Ciências Biomédicas Abel Salazar

FACULDADE DE ENGENHARIA
UNIVERSIDADE DO PORTO

INSTITUTO DE CIÊNCIAS BIOMÉDICAS ABEL SALAZAR
UNIVERSIDADE DO PORTO

NUCLEIC-ACID BASED STRUCTURES AS SMART NANOTOOLS IN NEUROTHERAPEUTICS

Joana Alexandra Silva

Dissertation submitted in partial fulfilment of
the requirements for the degree of
Master in Bioengineering
Molecular Biotechnology

Supervisor: Dr. Pedro Moreno
Co-supervisor: Prof. Dr. Ana Pêgo

September 2016

ABSTRACT

Current challenges posed to neuroscientists relate to the development of effective therapeutic approaches based on the advances accomplished by basic scientific research. In the neurotherapeutic field, the translation from laboratory into clinic has been limited by the general unmet need for an effective and safe *in vivo* approach, amplified by the extraordinary complexity and specificity of the nervous system.

Both therapeutic and biomarker molecules have been suggested as potential future options for applications in effective treatments and as diagnostic tools, however the search for an efficient delivery system and a sensitive sensing platform continues. Although several nanotechnological tools have entered clinical trials, with some having been approved for clinical applications, there is still a major requirement to be met: achieving maximal efficacy and specificity with minimal toxicity and side-effects.

DNA nanotechnology has been recently regarded as a possible key to address this need. Through strictly defined and predictable base-pairing rules, high order nanostructures with controllable size, shape and surface chemistry can be generated as a population of molecularly identical structures. Additionally, structured DNA has been proved to present good biocompatibility, enhanced resistance to enzymatic digestion as well as capacity for cell internalization, with no induced cytotoxicity or immune response. The multitude of different nanoarchitectures that have already been studied and reported confirms the robustness and potential of this type of structures for biotechnological applications, with promising results towards achieving a safe and efficient delivery of therapeutic agents and sensing probes.

Here, we report a newly designed neuronal-targeting tetrahedral DNA nanostructure (TDN). Novel TDN sequences were designed and optimized for an efficient assembly, bearing three single stranded DNA (ssDNA) “anchors” for further conjugation with the neuronal targeting peptide, Tet1. DLS analysis of the TDN revealed an approximate diameter of around 13 nm, in accordance with expected values. Visual confirmation of the structure was done by AFM analysis, which resolved pyramid-like structures with height values very close to predicted ones.

Targeting properties were accomplished through annealing the ssDNA anchors in the TDN with complementary ssPNA-Tet1 conjugates. Cellular uptake studies confirmed the ability of TDN structures to be internalized by neuronal type cell lines. In differentiated neuronal-like cells, we were able to show a significant enhancement of cell uptake by TDN structures bearing 1-3 PNA-Tet1 conjugate molecules, involving receptor-mediated uptake interactions through the Tet1 binding receptor, Gt1b. In addition, TDN-Tet1 systems proved to be highly specific, as no uptake was observed in a non-neuronal cell line, NIH 3T3, with no Gt1b receptor expression at the surface.

Results suggest that the newly designed TDN-Tet1 system holds great promise as an efficient nanotool for neurotherapeutic applications, being the first reported DNA-based structure efficiently targeting neuronal cells.

KEYWORDS: DNA Nanotechnology · DNA tetrahedron · Biosensors · Nanodevices · Neuronal targeting · Neurotherapeutics · Self-assembly · Smart delivery vectors

SUMÁRIO

Atualmente, uma das maiores limitações na neurociência relaciona-se com o desenvolvimento de terapias eficazes baseadas nos avanços da investigação cientifica fundamental. Na área da neuroterapêutica, a translação laboratório-clínica tem sido limitada pela necessidade geral de um sitema com eficiência e segurança *in vivo*, limitação essa amplificada pela imensa complexidade e especificidade do sistema nervoso.

Várias compostos terapêuticos e biomarcadores têm surgido como potenciais futuros candidatos para aplicações em tratamentos eficazes e plataformas de diagnóstico, respetivamente, no entanto a procura por sistemas de entrega adequados ou soluções de diagnóstico precisas continua. Apesar de vários e diferentes sistemas nanotecnológicos terem sido desenvolvidos e testados em ensaios clínicos, com alguns exemplos de aprovações para comercialização, existe ainda um importante requisito por cumprir: alcançar máxima eficácia e especificidade com níveis mínimos de toxicidade e efeitos adversos associados.

A nanotecnologia de DNA tem sido recentemente considerada uma possível solução face às necessidades indicadas. Em consequência das estritamente definidas e previsíveis regras de emparelhamento, complexas estruturas podem ser geradas, com um rigoroso controlo sobre o tamanho, a arquitetura e adicionais caracteristicas, originando populações de estruturas molecularmente idênticas. Adicionalmente, DNA em estrutura tem provado apresentar biocompatibilidade adequada, melhorada resistência a digestão enzimática, bem como capacidade de internalização celular, não induzindo atividade citotóxica ou resposta imunológica. A multiplicidade de diferentes estruturas estudadas até ao momento confirma a robustez e potencial deste tipo de estruturas para aplicações biotecnológicas, com resultados promissores no que respeita à sua integração numa segura e eficaz entrega de agentes terapêuticos e sensores biológicos.

No presente trabalho, é descrito o design de um inovador tetraedro de DNA (TDN – do inglês "tetrahedral DNA nanostructure") com um "target" específico para células neuronais. Novas sequências foram desenhadas e otimizadas para um "assembly" eficiente numa estrutura tetraédrica, expondo três âncoras de DNA de cadeia simples (ssDNA – do inglês "single stranded DNA") para posterior incorporação do péptido Tet1. Análise por DLS revelou um diâmetro aproximado à volda dos 13 nm, concordante com valores esperados. Análise por AFM permitiu a confirmação visual da estrutura, evidenciando arquiteturas semelhantes a pirâmides com valores de altura muito próximos dos valores previstos.

As propriedades de targeting foram conseguidas através do "annealing" entre as âncoras de ssDNA do TDN e moléculas de ssPNA complementares conjugadas com o péptido Tet1 (conjugados ssPNA-Tet1). Estudos de internalização celular confirmaram a superior capacidade de internalização do TDN não modificado, por células neuronais. Em células neuronais diferenciadas, observámos um aumento significativo da internalização celular de estruturas TDN com 1-3 conjugados PNA-Tet1 incorporados, resultado de interações específicas com o recetor para o péptido Tet1, Gt1b. Adicionalmente, os sistemas TDN-Tet1 provaram a sua especificidade, uma vez não terem demonstrado internalização por uma linha celular não-neuronal, NIH 3T3, a qual não expressa o recetor Gt1b à superfície.

Os resultados obtidos sugerem que o inovador sistema TDN-Tet1 aqui estudado apresenta um grande potencial para o seu desenvolvimento numa ferramenta útil à neuroterapêutica, sendo a primeira estrutura de DNA com um "targeting" específico para células neuronais desenhada e reportada.

PALAVRAS-CHAVE Nanotecnologia de DNA · Tetraedro de DNA · Biosensores · Nanodispositivos · Targeting neuronal · Neuroterapêutica · Self-assembly · Vetores de entrega inteligentes

ACKNOWLEDGMENTS

Chega ao fim uma das primeiras etapas da minha vida, a vida de estudante. Ao longo destes anos, tudo o que de bom vivi partilhei-o com outros, e é a eles que devo o ter chegado aqui com um sorriso na cara e no coração. Gostaria de expressar os meus sinceros agradecimentos a todos aqueles que das mais variadas formas me apoiaram na realização do presente trabalho. Não posso, no entanto, deixar de agradecer de forma especial aos seguintes:

Antes de mais, agradeço a quem me deu tudo, aos meus papis, por serem quem são, por terem feito de nós tudo o que de bom somos e por nos terem proporcionado tanto, muito além das suas possibilidades.

À Ana, a minha pessoa preferida, por ser tão original, justa, determinada e forte, sobretudo forte. Mereces tudo e muito mais, mereces ser feliz todos os dias, mais do que qualquer um.

Agradeço ao Yuri, todo o amor, todas as partilhas, todo o apoio e constante incentivo, incondicionalmente.

Agradeço aos meus amigos, cada um tão especial: à Sara, pelo seu enorme coração; à Inês, por ter sempre os pés na terra e a cabeça nos sonhos; à Elsa, por ser a amiga mais leal; à Lisa, por todas as confidências; à Joana, por todos os disparates e também pela sensatez, quando necessários; à Rita, pelas gargalhadas contagiantes; à Eva, por estar sempre a sorrir e de bem com a vida; ao Luís, pelo constante apoio e preocupação.

Agradeço aos meus pilares: Shica, Bárbara, Carlos, Joana Rui, Rita, Patrícia e Joana Cabrera, por estarem sempre onde estão e pelo incentivo e carinho constantes em todos os momentos da minha vida pessoal e académica.

Agradeço a todo o grupo nBTT, às pessoas com quem tive o prazer de trabalhar diariamente e que tão bem me integraram. Todas elas merecem um agradecimento especial, seja pela constante disponibilidade, pelos inúmeros incentivos ou pelo bom-humor contagiante. Devo um agradecimento especial à Ana Gerós, ao Luís Leitão, à Daniela Barros, à Estrela e à Ana Freitas, por terem dado animação extra a todos os dias mais cinzentos, tornando-os mais fáceis; à Carla Gomes, à Isabel Amaral, à Sofia Santos e à Daniela Sousa pelas dicas e a total disponibilidade no esclarecimento de dúvidas.

Um agradecimento especial é também devido aos técnicos Maria Lázaro e Ricardo Vidal, pela sua preciosa ajuda no set-up, respetivamente, das experiências de Image Stream e da célula zeta para altas concentrações.

Gostaria de agradecer à Ana Paula Pêgo, pela co-orientação deste trabalho, por todas as críticas e sugestões sempre pertinentes e valiosas.

Por último, agradeço ao meu orientador, Pedro Moreno, pela confiança demonstrada desde o ínicio e pela fantástica orientação e dedicação ao longo da realização deste trabalho, mostrando-se sempre presente e disponível para esclarecer qualquer dúvida ou dissipar qualquer hesitação. Agradeço a enorme partilha de conhecimentos e experiência científica, os quais contribuiram para um grande enriquecimento do presente trabalho e da minha experiência pessoal. Muito obrigada!

The research described in this dissertation was financed by:

- Santa Casa da Misericórdia de Lisboa—Prémio Melo e Castro (grant MC-1068-2015)

- Project NORTE-01-0145-FEDER-000008 , supported by Norte Portugal Regional Operational Programme (NORTE 2020), under the PORTUGAL 2020 Partnership Agreement, through the European Regional Development Fund (ERDF)

- Fundo Europeu de Desenvolvimento Regional funds through the COMPETE 2020 - Operacional Programme for Competitiveness and Internationalisation (POCI), Portugal 2020, and by Portuguese funds through FCT - Fundação para a Ciência e a Tecnologia/ Ministério da Ciência, Tecnologia e Ensino Superior in the framework of the project "Institute for Research and Innovation in Health Sciences" (POCI-01-0145-FEDER-007274)

"The Brain is wider than the Sky
For put them side by side –
The one the other will contain
With ease – and You beside."

Emily Dickinson

TABLE OF CONTENTS

ABSTRACT II
SUMÁRIO IV
ACKNOWLEDGMENTS VI
LIST OF FIGURES XII
LIST OF TABLES XVI
ABBREVIATIONS XVIII

CHAPTER 1 SCIENTIFIC BACKGROUND 1

1.1. INTRODUCTION 2
1.2. DNA NANOTECHNOLOGY 2
1.2.1. STRUCTURAL ASSEMBLY METHODS 3
1.2.2. IN SILICO DESIGN OF SEQUENCES 5
1.2.3. THE ADVANTAGES OF STRUCTURED DNA AS A NANOTOOL 5
1.2.3.1. PNA: a promising strategy for functionalization 7
1.3. AIMING AT NEUROPROTECTION AND NEUROREGENERATION 7
1.3.1. STRATEGIES FOR NEURONAL TARGETING 8
1.3.2. POTENTIAL OF DNA-BASED DELIVERY VECTORS FOR NEUROTHERAPEUTIC AGENTS 9
1.3.3. POTENTIAL OF DNA-BASED SMART SENSING DEVICES IN NEUROTHERAPEUTICS 11
1.3.4. DNA-BASED THERANOSTICS PLATFORM 12
AIM OF THE THESIS 14

CHAPTER 2 MATERIALS AND METHODS 15

2.1. MATERIALS 16
2.2. IN SILICO DESIGN OF NOVEL TDN2 SEQUENCES 16
2.3. ASSEMBLY AND PURIFICATION OF TDNS 17
2.4. CHARACTERIZATION OF TDNS 18
2.4.1. GEL ELECTROPHORESIS ANALYSIS 18
2.4.2. DYNAMIC LIGHT SCATTERING 18
2.4.3. ATOMIC FORCE MICROSCOPY 18
2.5. ASSEMBLY AND CHARACTERIZATION OF TDN-TETT1 SYSTEM 18
2.6. CELL CULTURE 19
2.6.1. ND7/23 DIFFERENTIATION 19
2.6.2. IMMUNOCYTOCHEMISTRY 19
2.7. CELLULAR ASSOCIATION AND UPTAKE STUDIES 19
2.7.1. CONFOCAL MICROSCOPY ANALYSIS 19
2.7.2. FLOW CYTOMETRY ANALYSIS 20
2.7.3. IMAGE STREAM ANALYSIS 20
2.8. STATISTICAL ANALYSIS 20

CHAPTER 3 RESULTS AND DISCUSSION 21

3.1. PROTOCOL OPTIMIZATION USING PREVIOUSLY STUDIED TDN SEQUENCES 22
3.1.1. TDN1 ASSEMBLY BY THE MULTISTRAND APPROACH: ANNEALING OF FOUR DNA STRANDS PRE-DESIGNED TO HYBRIDIZE INTO A TETRAHEDRON 22
3.1.2. TDN1 EXTRACTION AND PURIFICATION FROM POLYACRYLAMIDE GELS 24
3.2. ASSEMBLY AND CHARACTERIZATION OF NEWLY DESIGNED TDN2 SEQUENCES 26

3.2.1. DESIGN OF A NOVEL DNA TETRAHEDRON 26
3.2.2. PAGE ANALYSIS OF TDN2 27
3.2.3. DLS ANALYSIS OF TDN2 29
3.2.4. AFM ANALYSIS OF TDN2 30
3.2.5. INITIAL ASSESSMENT OF THE NOVEL TDN2 CELLULAR UPTAKE 31
3.3. DEVELOPMENT AND CHARACTERIZATION OF THE CELLULAR MODEL FOR UPTAKE STUDIES 32
3.4. ASSESSMENT OF THE PNA-TET1 EFFICIENCY BY CONJUGATION WITH STREPTAVIDIN-BIOTIN SYSTEM 33
3.5. TDN NEURONAL TARGETING BY TET1 PEPTIDE 39
3.5.1. PAGE CHARACTERIZATION OF THE TDN-TET1 SYSTEM 39
3.5.2. IN VITRO UPTAKE STUDIES OF TDN-TET1 40

CHAPTER 4 CONCLUSION AND FUTURE PERSPECTIVES 47

SUPPLEMENTARY INFORMATION 51

REFERENCES 57

LIST OF FIGURES

Figure 1 Synthetic (left) and design (middle) schemes of DNA constructed (a) cube, (b) tetrahedron and (c) polypodna, specifically a hexapodna.

Figure 2 (a) Double (left), triple (middle) and paranemic (right) crossover motifs. (b) Tetrahedron, dodecahedron and buckyball assembled from three-point star building blocks. (c) Icosahedron assembled from six-point star motifs, bearing an aptamer (in blue) on one of the strands.

Figure 3 DNA origami design concept. (a) Cylinder representation of single-layer DNA origami objects and (b) respective single-layer scaffold. (c) Examples of respective staples layout (colored segments) for the desired folding of the scaffold.

Figure 4 (a) Design principles for controlling twists and curvatures (left) and bending bundle with base-pair deletions, in orange, and insertions, in blue (right). (b) Schematic representation of DNA hemisphere (left), sphere (middle) and nanoflask (right) structures.

Figure 5 (a) Schematic representation of the tetrahedral oligonucleotide nanoparticle (ONP) showing site-specific hybridization of siRNA strand (left) and orientation of the ligand (in the form of bullet shapes on ends of siRNA strands - right). (b) Serum IFN-α levels 6 hours after administration of control PBS, ONP or lipofectamine (LF), showing no induced serum immune response with the ONP.

Figure 6 Chemical structure of a DNA-PNA hybrid duplex. Backbones composition is depicted for each single strand: an uncharged glycine-based backbone in PNA and a negatively charged phosphate backbone in DNA.

Figure 7 (a) Schematic representation of the self-assembly of DNA nanotrains from two short DNA strands upon initiation from a targeting aptamer. Resultant nanotrains were loaded with Dox by intercalation. (b) DNA nanorobot schematic representation in a closed (top) and open (bottom) conformation. In the presence of the target antigen, the aptamer will bind it, displacing the complementary strand and opening the structure for payload exposure.

Figure 8 (a) Schematic representation of nano-SNEL, with the molecular beacon sensor indicated and its fluorophore and quencher molecules in red and black, respectively. (b) Schematic representation of the DTMB (DNA tetrahedron-based molecular beacon with the loop and stem portions incorporated in one of the sequences, and the fluorophore (F) and quencher (Q) incorporated in another sequence.

Figure 9 Scheme of the eight different robot types, each presenting its own task: three effector robots E, F and G, carrying a different drug; four positive regulators, P1 and P2 as opening keys to F, P3 and P4 as opening keys to G; and a negative regulator N that inactivates G opening. Two first-layer gates, AND and OR, control their own drug release and the release of a third drug on a second-layer gate, XOR (top). Examples of distinct drug combinations according to different protein cues present are represented (bottom).

Figure 10 UV shadowing technique. In this technique, the gel is placed on plastic wrap over a silica-coated TLC plate on which UV light is shone upon. The dye in the UV-fluorescent plate is excited, while nucleic acids absorb the light, casting a shadow against the fluorescent background.

Figure 11 Summary of the optimized TDN purification protocol. The first four steps consist of the optimized Crush&Soak protocol, with a manual cutting of the pieces and an incubation time of 48 h at 4˚C. The following steps correspond to the buffer exchange protocol, using Amicon centrifugal filter devices.

Figure 12 PAGE analysis of the step-by-step assembly of the TDN with the representation of one, two, three or all four sequences in the gel. On the left of the gel, schematic representations of presumed formed structures are presented.

Figure 13 Percentage of TDN in each sample according to the annealing protocol: 2 h 30 min (SLOW) or 30 s (FAST), comparing a range of different final strands concentrations. Data results from one experiment.

Figure 14 PAGE analysis of annealed strands comparing three different buffers and three different final strands concentrations. Displayed percentages on the bottom indicate the percentage of TDN in each lane. Note: this gel was run in TBE 1x, and not in TBE 1x 12.5 mM MgAc2, which explains the different migration of the bands and the localization of the TDN1 band at around 200 bp instead of 250 bp as previously indicated. The tetrahedron band is schematically indicated to the left of the gel.

Figure 15 Tetrahedron recovery after purification by the Spin-X and the Crush&Soak methods.

Figure 16 TDN recovery (left) and purity (right) after purification following altered Crush&Soak protocols as analyzed by PAGE.

Figure 17 Representation of the novel TDN design, wavy lines representing the anchor sequences, which have the same pre-defined sequence (as determined for high affinity binding to a 15-mer PNA sequence) and arrows representing the 3’ ends of the sequences (left). Segmentation of the tetrahedron design into 3 regions without pseudoknots for NUPACK analysis and sequence design (right).

Figure 18 (a) NUPACK generated sequences from a maximum probability of defects of 3.1 % (top). Minimum free-energy structures of the resultant sequences for the 3 segmented regions of the TDN. (b) Output sequences representation in a tetrahedral structure. Green bases are unpaired, red bases represent the 5’ ends of sequences.

Figure 19 Stepwise assembly of novel TDN2 sequences by combining equimolar quantities of combinations of strands. On the left of the gel, schematic representations of the presumed structures are presented.

Figure 20 PAGE analysis of annealed strands comparing three different buffers and final strands concentrations. Indicated percentages specify the percentage of TDN2 in each lane. The tetrahedron band is schematically indicated to the left of the gel.

Figure 21 PAGE analysis of the hybridization of the TDN2 anchors with a complementary DNA strand (rc18) at different ratios. The tetrahedron band is schematically indicated to the left of the gel. Inset: bands corresponding to 1, 2 and 3 hybridized linker DNAs - bottom to top, respectively - are highlighted.

Figure 22 TDN2 size distribution by intensity of scattered light. Mean hydrodynamic diameter as wells as the standard deviation are indicated above the graph.

Figure 23 AFM liquid analysis of TDN2. Inset: proposed scheme of the resolved structure, highlighting what resembles three upper edges and the triangular base of the tetrahedron.

Figure 24 Image Stream Cytometry analysis of the cellular uptake of untreated ND7/23 cells (CTR – pointed grey graph) and cells incubated with FAM-labeled TDN2 (TDN2 – blue graph). Cellular uptake was assessed according to the fluorescence intensity in (a) the whole cell, (b) cellular membrane and (c) cytoplasm. Median intensity values of each analyzed sample are indicated in the table below each graphic. Data from (b) and (c) were obtained through the use of membrane and cytoplasm masks for the analysis of the fluorescence intensity.

Figure 25 Representative images of NF-H (green) expression in differentiated and not differentiated ND7/23 cells. Nuclei are stained with Hoechst 33342 (blue). White arrows indicate neurite-like extensions formed by differentiated cells. Scale bars: 100µm.

Figure 26 FACS analysis of Gt1b expression in differentiated and not differentiated ND7/23 cells and in NIH 3T3 cells, as a negative control. Represented in grey is the unstained sample. The blue colored data corresponds to the anti-Gt1b stained sample. Median Gt1b intensity values of stained samples are

indicated on histograms. Displayed percentages on dot plots indicate the frequency of the Gt1b positive cells in the population.

Figure 27 Schematic representation of the StvBiot-Tet1 (left) system and corresponding control StvBiot-rcON (right).

Figure 28 PAGE analysis of the optimal ratio for the conjugation of (left) Streptavidin/Biotin-ON and (right) Streptavidin/Biotin-ON-Tet1. The Stv/Biot-ON band is indicated.

Figure 29 ND7/23 cell association of StvBiot conjugated to either a (a) control reverse complementary ssDNA or (b) the targeting peptide Tet1. Scale bars: 25 µm. (c) Orthogonal views from different planes (x/y, x/z or y/z) of StvBiot-Tet1 treated cells confirm that the 488 labeled system localizes inside the cell (left) and co-localizes or is in close proximity with Gt1b receptor (middle and right). Scale bars: 15 µm.

Figure 30 Cell association of StvBiot-rcON (blue) or StvBiot-Tet1 (orange) assessed by flow cytometry. A histogram of the cell signal intensity at 488nm is represented on the left with untreated cells in grey and cells incubated with either StvBiot-rcON in blue or StvBiot-Tet1 in orange. On the right the percentage of 488 positive cells is depicted graphically, considered taking into account the autofluorescence signal of untreated cells (CTR). Results obtained from two independent experiments.

Figure 31 PAGE analysis of the system TDN-Tet1. On the left, two different ratios were tested as well as different temperatures for the annealing between the ssDNA anchors of TDN and the complementary ssPNA of the PNA-Tet1 conjugate: an incubation of 3 min at 40˚C and cooling down to 20˚C in 1 hour or an incubation of 1 hour at room temperature. On the right, three ratios were tested, with an incubation of 1 hour at room temperature. The tetrahedron band is schematically indicated to the left of the gel. Inset: for clarity purposes, a higher contrast image indicates the presence of higher mass structures close to the tetrahedron band.

Figure 32 Confocal analysis of differentiated ND7/23 cells incubated with naked TDN and TDN-Tet1 systems for 1 hour at 37˚C. (a) Incubations done at a final concentration of 0.05 µM of each system. Arrows point to TDN-Tet1 structures in close proximity to the nuclei. Scale bars: 15 µm. (b) Orthogonal views (x/y, x/z or y/z) of cells incubated at a concentration of 0.025 µM with each system indicate the co-localization of the FAM-labelled TDN-Tet1 and the Gt1b signals (bottom), while no apparent co-localization exists in the signals from the naked TDN and the Gt1b receptor (top). Nuclei are stained with Hoechst 33342 (blue), FAM-labelled TDNs are represented in green and Gt1b receptor in red. Scale bars: 25 µm.

Figure 33 Representative confocal images focusing on differentiated ND7/23 cells showing neurite-like extensions (highlighted by a white dotted line in the brightfield images) after incubation for 3 hours with either the naked TDN (top) or the TDN-Tet1 (bottom) system at a concentration of 0.025 µM. White arrows indicate sites of co-localization of the TDN-Tet1 signal (green) and the Gt1b receptor signal (red). Scale bars: 10 µm.

Figure 34 a and b) Confocal microscopy representative images of differentiated ND7/23 cells incubated with naked TDN and neuronal targeting TDN-Tet1 systems for 2 hours at 4˚C (0.025 µM). (b) Duplicate images for clarity purposes, brightfield and FAM-TDN merged images elucidate the localization of the structures within the cell. Scale bars: 25µm. Nuclei are stained with Hoechst 33342 (blue), FAM-labelled TDNs are represented in green and Gt1b receptor is stained in red.

Figure 35 Image Stream analysis of untreated differentiated ND7/23 (CTR - grey) and differentiated ND7/23 incubated with FAM-s4b (green), FAM-TDN (blue) and FAM-TDN-Tet1 (orange). (a) Cellular uptake was assessed according to the fluorescence intensity in the cell, as depicted in the representative histogram (left). Cellular intensity is translated into median values graphically represented (right). Results obtained from three independent experiments. (b) Fluorescence spots in the cells were measured, making use of spot masks and spot-counting features. A representative histogram of spot-count normalized frequencies is on the left, zoomed in on the right. * denotes statistical significance between samples, using repeated measures one-way ANOVA statistical analysis. * $p < 0,05$; ** $p < 0,01$; *** $p < 0,001$;

Figure 36 Image Stream analysis of untreated (CTR - grey) cells and NIH 3T3 cells incubated with FAM-s4b (green), FAM-TDN (blue) and FAM-TDN-Tet1 (orange). (a) Cellular uptake was assessed according to the fluorescence intensity in the cell, illustrated in the representative histogram (left), and translated into graphically represented median values (right). Results obtained from three independent experiments. (b) Fluorescence spots in the cells were measured, making use of spot masks and spot-counting features. A representative histogram of spot-count normalized frequencies is on the left, zoomed in on the right. * denotes statistical significance between samples, using repeated measures one-way ANOVA statistical analysis. **** p < 0,0001.

LIST OF TABLES

Table 1 Examples of reported nucleic-acid based structures and their potential biological applications.

Table 2 Stability of the purified TDN1 for 4 weeks at 4˚C, as indicated by the purity of the samples run in polyacrylamide gels (hyphens mark samples which were not analyzed on the indicated time-point due to sample extinction; t=0 samples were analyzed immediately after purification).

Table 3 Percentages of number and volume occupied by the 1st peak, and PDI values obtained for each measurement.

ABBREVIATIONS

AD Alzheimer’s disease

AFM Atomic Force Microscopy

ALS Amyotrophic Lateral Sclerosis

BBB Blood-brain barrier

BCNU Carmustine

Biot Biotin

CNS Central nervous system

DNA Deoxyribonucleic acid

DLS Dynamic Light Scattering

Dox Doxorubicin

DRG Dorsal root ganglion

DX Double crossover motif

FRET Fluorescence resonance energy transfer

GDNF Glial cell line-derived neurotrophic factor

HD Huntington disease

HPLC High-Performance Liquid Chromatography

IFN Interferon

LF Lipofectamine

MDR Multidrug resistance

MFE Minimum free-energy

NF-H Neurofilament-heavy

ON Oligonucleotide

ONP Oligonucleotide nanoparticle

PCR Polymerase chain reaction

PD Parkinson’s disease

PEG Polyethylene glycol

PEI Polyethyleneimine

PNA Peptide nucleic acid

PNS Peripheral nervous system

PX Paranemic crossover motif

RNA Ribonucleic acid

SEC Size Exclusion Chromatography

Stv Streptavidin

TDN Tetrahedral DNA nanostructure

TeNT Tetanus toxin

TX Triple crossover motif

VEGF Vascular endothelial growth factor

CHAPTER 1

SCIENTIFIC BACKGROUND

1.1. INTRODUCTION
1.2. DNA- NANOTECHNOLOGY
    1.2.1. STRUCTURAL ASSEMBLING METHODS
    1.2.2. IN SILICO DESIGN OF SEQUENCES
    1.2.3. THE ADVANTAGES OF STRUCTURED DNA AS A NANOTOOL
        1.2.3.1. PNA: A PROMISING STRATEGY FOR FUNCTIONALIZATION
1.3. AIMING AT NEUROPROTECTION AND NEUROREGENERATION
    1.3.1. STRATEGIES FOR NEURONAL TARGETING
    1.3.2. POTENTIAL OF DNA-BASED DELIVERY VECTORS FOR NEUROTHERAPEUTIC AGENTS
    1.3.3. POTENTIAL OF DNA-BASED SMART SENSING DEVICES IN NEUROTHERAPEUTICS
    1.3.4. DNA-BASED THERANOSTICS PLATFORM

1.1. INTRODUCTION

In spite of the huge development and advances accomplished in the last decades, there is still a lack of a successful therapy for most neuropathies. Due to the special complexity and sensitivity of the neural network, exceptional measures must be taken to address neurological issues.

There is a growing demand for novel options of safe and specific delivery of therapeutic molecules (such as small drugs, proteins and nucleic acids-based drugs) to the central and peripheral nervous system for the treatment of neurodegenerative diseases and nerve injury, as well as new biosensors that could provide early detection of biomarkers associated with some of the abovementioned conditions. Of special interest is the development of new tools that could provide both detection and actuation in neurological conditions, thus providing potential neuro-theranostics platforms.

A recently emerged attractive nanomedicine tool is based on the construction of nucleic acids-based 2D and 3D structures able to act as nanodelivery tools or biosensing devices. DNA nanotechnology principles provide the unique ability to precisely engineer a nanostructure at the atomic scale, allowing for unprecedented control in the construction of such systems. The produced DNA-based nanostructures can be made as a population of molecularly identical structures with strictly defined architecture, features and composition. The attractiveness of these systems also lies in the fact that functionalization can be accomplished by simply assembling molecules of interest to DNA nanostructures with nanometer-scale precision. In addition, a plethora of different tailor-made DNA devices can be made to respond to a wide range of biological cues and easily integrated into DNA-based nanostructures, facilitating the development of intelligent devices.

Thus, DNA nanotechnology principles allow the engineering of "smart" DNA-based nanostructures, with strictly defined characteristics, providing novel options for future neurotherapies.

In the present work, we aim to explore the potential of this novel technology to develop tailor-made nucleic-acid based structures as potential neuron-targeted delivery devices, paving the way for applications as therapeutic molecule carriers and diagnostics.

1.2. DNA NANOTECHNOLOGY

The pioneer of DNA nanotechnology was Ned Seeman, who proposed, in 1982, the creation of regular 3D lattices of DNA that could serve as scaffolds for binding of biological macromolecules (Seeman, 1982). This revolutionary idea broadened the DNA boundaries, giving rise to the realization of DNA as more than a genetic information carrier. DNA started to be studied as a building material, revealing an enormous scope of applications by the rational design of nanostructures with one, two or three dimensions.

DNA is a double helix self-assembling biopolymer, whose formation is directed by canonical Watson-Crick base pairing (Watson & Crick, 1974). DNA is also a chemically stable, easy to functionalize and relatively inexpensive material, which can be completely chemically synthesized. In DNA nanotechnology, single-stranded short overhangs, denominated sticky ends, can be used to connect independent DNA molecules, allowing for a controlled assembly of multiple molecules. The combined use of sticky ends at junction points and programmed assembly via complementary base-pairing make these molecules useful building blocks for complex structures (Mohri, Nishikawa, Takahashi, & Takakura, 2014).

The field of DNA nanotechnology has been rapidly evolving in the last few years, non-surprisingly reaching the biomedical context, where complex functionalities and arrangements are essential. The ability to construct DNA nanostructures for biomedical applications is dependent on efficient self-assembling reactions. DNA nanotechnology has proved to be a promising strategy for the construction of reliable delivery systems and smart molecular devices **(Table 1)**.

Table 1 Examples of reported nucleic-acid based structures and their potential biological applications.

Nucleic-acid based structure	Desired function	Application	Authors
Multi-helix rectangular DNA tile	Precise spatial display of multiple-affinity α-thrombin	Multivalent interactions investigation	Rinker, Ke, Liu, Chhabra, & Yan, 2008
DNA icosahedron loaded with doxorubicin	Delivery of doxorubicin to cancer cells	Cancer therapy	Chang, Yang, & Huang, 2011
DNA icosahedron encapsulating fluorescein isothiocyanate	Report of pH variation during endosomal maturation	*In vivo* imaging	Bhatia, Surana, Chakraborty, Koushika, & Krishnan, 2011
DNA origami tube loaded with doxorubicin	Delivery of doxorubicin to cancer cells	Cancer therapy	Zhao et al., 2012
DNA origami honeycomb lattice	Pore introduction into cell membrane and molecule discrimination.	Anti-microbial agent	Langecker et al., 2012
DNA origami hexagonal barrel	Growth arrest in leukemic cells through specific antibody delivery	Cancer therapy	Douglas, Bachelet, & Church, 2012
DNA tetrahedron	Specific siRNA delivery to tumour cells	Cancer therapy	Lee et al., 2012
Polypodna	CpG DNA delivery to immune cells	Innate immunity stimulation	Mohri et al., 2012
Rectangular DNA origami sheet	Precise spatial display of reporter probe-QDs complex	Quantification of miRNA concentration	Jiehua Zhu et al., 2013
DNA origami triangles loaded with doxorubicin	Delivery of doxorubicin to cancer cells	Cancer therapy	Q. Zhang et al., 2014
TDN-based molecular beacon	Detection of tumor-related TK1	Cancer diagnostics	Xie et al., 2016

1.2.1. STRUCTURAL ASSEMBLY METHODS

Soon after the foundation of DNA nanotechnology was laid, early models of DNA self-assembly relied on the formation of a stable DNA junction motif (inspired by the Holliday junction), consisting on a flexible junction and stable double-stranded DNA arms (Seeman, 1982). The simplest designs were obtained by the repetition and ligation of these units through sticky-end connections, which could lead to the generation of 2D structures, such as square lattices **(Fig. 1a middle)** and later on 3D structures, as for example a cube **(Fig. 1a right)**.

Following this initial idea, other designs were realized through the use of the multistrand-approach, where short independent oligonucleotides successively hybridize following thermal melting and cooperativity rules. With this assembly method, structures like the tetrahedron **(Fig. 1b)** and the polypodna (polypod-like DNA) **(Fig. 1c)** were obtained (Chen & Seeman, 1991; Goodman et al., 2005; Mohri et al., 2012).

Fu and Seeman also established the design of more complex structures from the realization of Crossover motifs **(Fig. 2a)**, the initial example being the double crossover motif (DX) (Fu & Seeman, 1993). This motif consists of two double-stranded helices that interchange with one of the strands at two crossover points. Soon after, triple crossover motifs (TX) were also obtained with three double-stranded helices interchanging with one of the strands at three crossover points (LaBean et al., 2000). Another motif, the paranemic crossover (PX), was designed based on the same principle, but consisted of two parallel helices with successive crossovers (Z. Shen, Yan, Wang, & Seeman, 2004).

Mao and co-workers introduced Sequence Symmetry as a method to generate nucleic-acid based structures from a symmetric three-point star motif **(Fig. 2b)** (He et al., 2005). With simple control over flexibility and concentration of building tiles, and through adaptation of the length of the central loop, this group synthesized a tetrahedron, a dodecahedron and a buckyball from the same set of tiles (He et al., 2008). In addition, also six-point star motifs were generated and used to, via sticky end cohesion, obtain an icosahedron **(Fig. 2c)** (M. Chang et al., 2011).

DNA nanotubes have also been object of interest, with several distinct assembly strategies reported. For instance, Liu and co-workers obtained DNA nanotubes from the rolling up of 2D arrays of DNA tiles by disulfide bond formation (D. Liu, Park, Reif, & LaBean, 2004).

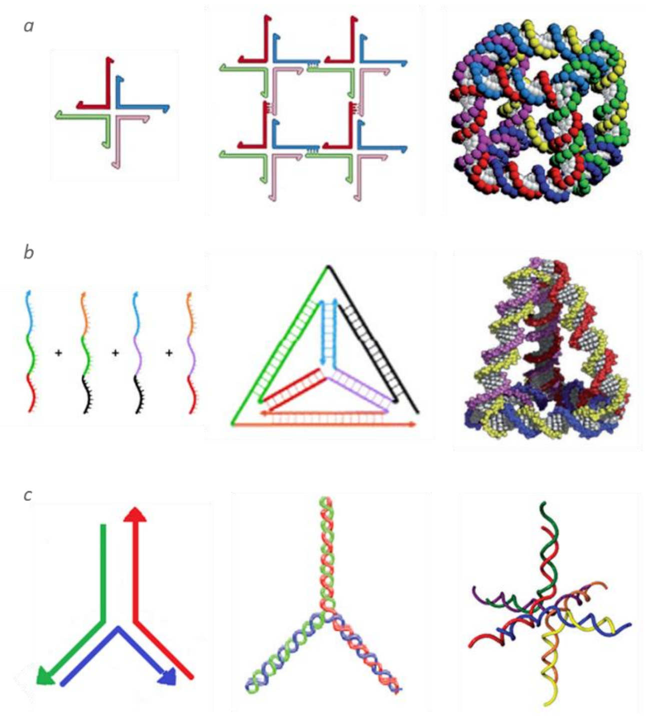

Figure 1 Synthetic (left) and design (middle) schemes of DNA constructed (a) cube, (b) tetrahedron and (c) polypodna, specifically a hexapodna (Adapted from de Vries, Zhang, & Herrmann, 2013).

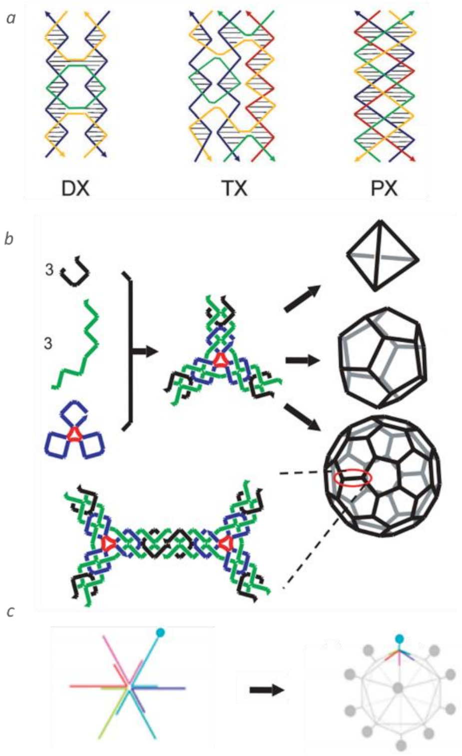

Figure 2 (a) Double (left), triple (middle) and paranemic (right) crossover motifs (Adapted from Tintoré et al., 2014). *(b) Tetrahedron, dodecahedron and buckyball assembled from three-point star building blocks (Adapted from* He et al., 2008). *(c) Icosahedron assembled from six-point star motifs, bearing an aptamer (in blue) on one of the strands (Adapted from* M. Chang et al., 2011).

In 2006, an important breakthrough in the field of DNA-nanotechnology revealed an additional method for the assembly of DNA-based structures: DNA origami (Rothemund, 2006),

In DNA origami structures, and similarly to the Japanese art of paper folding, a long, circular, single-stranded DNA molecule is used as a scaffold, which is “stapled” with the aid of shorter oligonucleotides, called staple strands, into a 2D or 3D arrangement (Rothemund, 2006) **(Fig. 3)**. In Rothemund’s publication, a single-stranded circular genomic DNA from the virus M13mp18 was folded with over 200 staple strands into an anti-parallel arrangement of helices through periodic crossovers. Self-assembling was accomplished by annealing from 95°C to 20°C in the presence of 100-fold excess of staple strands (Rothemund, 2006).

Since staple strands are complementary to different regions of the scaffold, they result in the formation of double-helical DNA domains, which connect to adjacent domains by anti-parallel crossovers (Seeman, 2010). Staples can take part of multiple crossovers, connecting multiple double-helical domains, granting these structures some density and rigidity (Lanier & Bermudez, 2015). Furthermore, each correct binding of staple strands favors the subsequent accurate binding of the next “staples” while eliminating undesired secondary structures by displacement of incorrect sequences (Saccà & Niemeyer, 2012). Such method allows to obtain well-defined nanostructures with high yield and reproducibility, leading to a reduction of the time and effort required for their production (Tintoré, Eritja, & Fábrega, 2014).

DNA origami structures with curvatures have also been described, through the addition or deletion of base pairs at specific positions, thus modulating the distance between crossovers **(Fig. 4a)** (Dietz, Douglas, & Shih, 2009). By organizing concentric DNA rings of different radii, nonlinear DNA shapes with intricate curvatures were generated **(Fig. 4b)** (Han et al., 2011).

The need for a long scaffold strand, which is usually obtained by purification of M13 bacteriophage, is a limitation of this method (Lanier & Bermudez, 2015). Different approaches to employ different scaffold sources have been reported, although the majority of these methods rely on time consuming strand separation procedures, enzymatic digestion, PCR and purification (Y. Yang, Han, Nangreave, Liu, & Yan, 2012; H. Zhang et al., 2012). A recent report by Nickels and co-researchers describes the creation of DNA structures from intact bacteriophages, without the need for thorough downstream purification procedures (Nickels et al., 2014). This method unlocks the potential for scalable DNA origami creation, which lies on self-production and purification of the scaffold material.

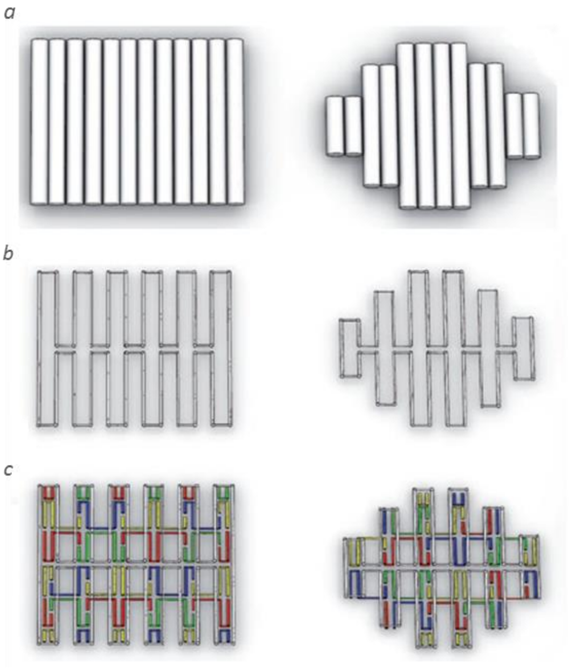

Figure 3 DNA origami design concept. (a) Cylinder representation of single-layer DNA origami objects and (b) respective single-layer scaffold. (c) Examples of respective staples layout (colored segments) for the desired folding of the scaffold (Adapted from Castro et al., 2011).

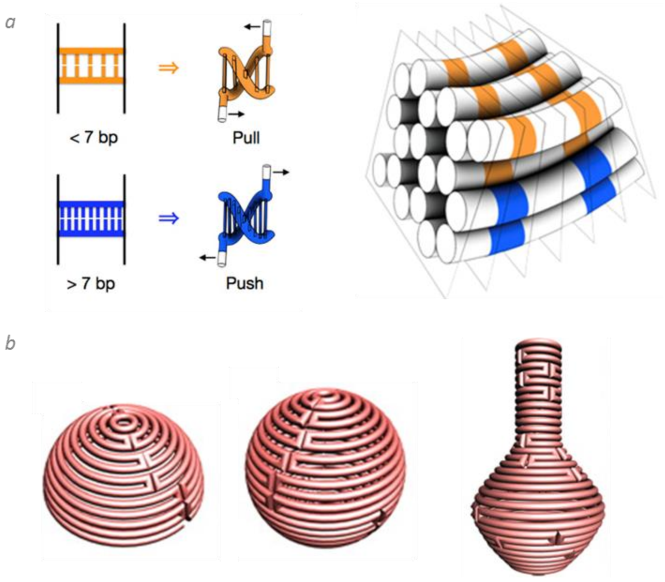

Figure 4. (a) Design principles for controlling twists and curvatures (left) and bending bundle with base-pair deletions, in orange, and insertions, in blue (right) (Adapted from Dietz, Douglas, & Shih, 2009*). (b) Schematic representation of DNA hemisphere (left), sphere (middle) and nanoflask (right) structures (Adapted from* Han et al., 2011*).*

1.2.2. In silico design of sequences

Computer-assisted programming of DNA nanostructures makes possible the engineering of molecularly defined designs, allowing the customization of surface architecture as well as, for instance, linkers arrangement (Douglas et al., 2009; Jinhao Zhu, Wei, Yuan, & Mi, 2009). The first computational tool for aiding the design of DNA structures was SEQUIN, developed by Seeman, and it was based on an algorithm for the *de novo* sequence generation. This algorithm directed sequence-symmetry minimization combined with equilibrium probability calculations, lying on sequence selection with the goal of minimizing similarities between segments, and thus decreasing the chance of undesired associations (Seeman, 1990).

Ever since, multiple tools have emerged allowing for a more facile access to DNA nanotechnology. Uniquimer (Jinhao Zhu et al., 2009), Tiamat (Williams et al., 2009), NUPACK (Zadeh et al., 2011) and CanDo (Castro et al., 2011) are a few examples of computational packages with which a researcher can rationally design a given structure: 1) construct a sketch; 2) obtain compatible sequences; 3) manipulate DNA strands through thermodynamic analysis and equilibrium properties calculation of predicted complexes; 4) optimize crossovers locations. All these steps translate in the achievement of *in silico* optimized structures that will increase the chances of successful DNA nanostructure assemblies *in vitro*.

1.2.3. The advantages of structured DNA as a nanotool

DNA nanotechnology is a highly efficient and controllable approach for creating structures of defined shape, size and characteristics. Through programmed design, these structures allow unique control over formulation and provide versatility unlike any other delivery system (Charoenphol & Bermudez, 2014). These DNA-based structures can be easily optimized for cell-specific delivery and additionally present distinct addressability, excellent water solubility, biocompatibility and biodegradability (Ming & Laing, 2015).

DNA-based structures represent a grid for the precise attachment of site-specific molecules, resultant from the heterogeneous sequence of the scaffold strand or framework oligonucleotide sequences (Smith, Schüller, Engst, Rädler, & Liedl, 2013). Nanometer-specific functionalization can be achieved at any position within the structure, which can further optimize the efficacy of the nanosystem (Mangalum, Rahman, & Norton, 2013). For instance, Lee and co-workers recently developed a DNA-based carrier system with hybridized 2'-*O*Me modified siRNA strands attached to cancer-targeting folate molecules **(Fig. 5a)**. The group demonstrated that the orientation and location of ligands dramatically affects gene silencing efficiency: for an optimal delivery of siRNAs into cells, at least three folate molecules, with an appropriate spatial orientation, per DNA nanoparticle are required. This tetrahedral system greatly enhanced the efficiency of RNAi in folate receptor-positive cells (Lee et al., 2012). The uniqueness of this type of system allowed the study of the finest spatial arrangement of targeting ligands for improved efficacy. Such detailed studies are clearly very important for the optimization of a delivery system and are very difficult, if not impossible, to address using other types of systems.

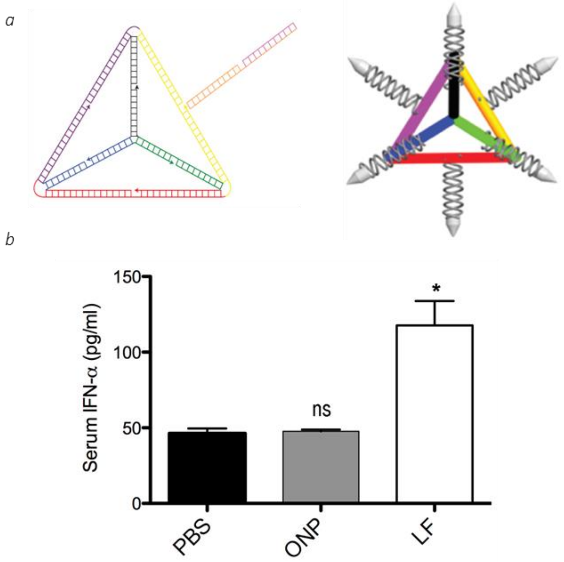

Figure 5 (a) Schematic representation of the tetrahedral oligonucleotide nanoparticle (ONP) showing site-specific hybridization of siRNA strand (left) and orientation of the ligand (in the form of bullet shapes on ends of siRNA strands - right). (b) Serum IFN-α levels 6 hours after administration of control PBS, ONP or lipofectamine (LF), showing no induced serum immune response with the ONP (Adapted from Lee et al., 2012).

Endogenous or exogenous nucleic acids are the basic units of cellular identity, thus, complex regulation, recognition and degradation mechanisms may represent a concern for the application of DNA-based delivery systems. For instance, within the bloodstream, free nucleases could potentially detect and digest foreign nucleic-acid material (Lanier & Bermudez, 2015). This issue has already been addressed by several groups with encouraging results. A study by Li and co-researchers revealed that internalized TDNs remained intact for at least 8h in cell culture, as indicated by fluorescence resonance energy (FRET) (J. Li et al., 2011). Another study demonstrated that compact DNA origami structures were stable in the presence of T7 exonuclease, E. coli exonuclease and Lambda nuclease, among others. Although susceptible to DNAse I action, full digestion by this enzyme was proved to be 10-times slower than its linear double stranded equivalent, possibly due to the shielding effect of close-packed double-helical domains in the structure. Furthermore, this group proved the maintenance of these objects in cell-culture medium, at low pH conditions and at 37°C, revealing their stability under physiological conditions (Castro et al., 2011).

Agent-free transport of DNA molecules through cellular membranes is generally unsuccessful, mostly due to the negative nature of these molecules. Remarkably, DNA nanostructures have been proved to be efficiently internalized by cells without the aid of transfection agents (Cutler et al., 2011; Hamblin, Carneiro, Fakhoury, Bujold, & Sleiman, 2012; Lee et al., 2012; Walsh, Yin, Erben, Wood, & Turberfield, 2011). A thorough study by Liang and co-workers evidenced the dynamics and mechanisms of internalization of these structures, revealing that TDNs, undergo rapid internalization - within 60 seconds - by caveolin-dependent endocytosis. The nanostructures are then orderly transported across microtubules with the aid of molecular motors. This group also verified that, upon internalization, TDNs are delivered to lysosomes, but the fate of these structures inside the cell can be altered by conjugation with organelle-specific signaling peptides, underlining the potential use of these structures as intelligent tools in biomedicine (Liang et al., 2014).

Biodegradability was, as well, already accessed, emphasizing the potential application of these systems. Shen and co-researchers reported a study on the *in vitro* distribution and stability of DNA origami tubes. This study revealed that after 12 hours of incubation, DNA structures were mostly localized in lysosomes. In addition, while proper folding was retained for about 24 hours, at 60 hours most structures were disassembled or unfolded (X. Shen et al., 2012).

Additionally, nucleotide materials, as crucial integrators of cellular environment, do not represent a potentially toxic platform. However, efforts must be made to ensure, as well, that they do not elicit an immunological response when tested in living organisms. Detection of DNA by eukaryotic cells results in the upregulation and secretion of type I Interferons (primarily numerous subtypes of IFN-α and one subtype of IFN-β). Upregulated IFNs culminate in an inflammatory signaling pathway through a set of IFN-stimulated genes with anti-viral and immunomodulatory roles (Platanias, 2005; Wu & Chen, 2014). Addressing this issue, the abovementioned first *in vivo* proof-of-principle study revealed no early immune response (no significant increase in IFN-α levels) towards the tetrahedral DNA nanostructure (TDN) system on the xenograft mouse model, even after multiple injections (Lee et al., 2012) **(Fig. 5b)**. Another report confirmed that the total amounts of white and red blood cells, hemoglobin and platelets presented normal values after systemic administration of Doxorubicin-loaded DNA triangles to xenograft mouse models. In this study, IFN-α levels were, once again, not altered in treated mice (Q. Zhang et al., 2014). These are encouraging results, however they only address a possible early immune response, accounting for the first 6h after administration. More prolonged studies would be desirable.

1.2.3.1. PNA: A PROMISING STRATEGY FOR FUNCTIONALIZATION

Peptide nucleic acids (PNA) are structural DNA analogues that contain an uncharged N-(2-aminoethyl) glycine-based backbone **(Fig. 6)**, as opposed to the negatively charged deoxyribose phosphate backbone in DNA (Egholm, Buchardt, Nielsen, & Berg, 1992; Nielsen, Egholm, Berg, & Buchardt, 1991). Since the four nucleotides and spacing between them are maintained, this molecule is capable of hybridizing via Watson-Crick base-pairing to complementary DNA sequences. These DNA-PNA hybrid duplexes are reported to present a higher thermal stability, hypersensitivity to sequence mismatches, as well as a higher resistance to enzymatic degradation (Demidov et al., 1994; Egholm et al., 1993). The high thermal melting stability of PNA-DNA duplexes is mostly attributed to the neutral charge nature of the PNA molecule, avoiding any electrostatic repulsion between the two strands as in the case of a DNA-DNA duplex (Egholm et al., 1993).

The synthesis of PNA is compatible with peptide synthesis, hence these oligomers can be readily obtained by standard peptide solid-phase synthesis protocols (Ray & Nordén, 2000).

These facts suggest a promising approach for the easy and efficient incorporation of peptides, as for instance neuronal targeting peptides, into DNA nanostructures by using a PNA linker. Flory and co-workers have described the assembly of 3D DNA-PNA-Protein complexes, through the use of PNA-protein conjugates hybridized to 3D DNA nanocages, aiming to obtain a precise 3D framework for the study of protein-protein interactions (Flory et al., 2014).

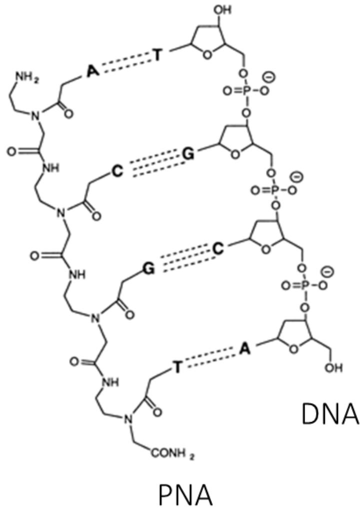

Figure 6 Chemical structure of a DNA-PNA hybrid duplex. Backbones composition is depicted for each single strand: an uncharged glycine-based backbone in PNA and a negatively charged phosphate backbone in DNA (Adapted from Peter E. Nielsen & Egholm, 1999).

1.3. AIMING AT NEUROPROTECTION AND NEUROREGENERATION

Several conditions may compromise normal neuronal function, disrupting regular dynamics of the neuronal system, either by nerve injury or neurodegeneration (Miras-Portugal et al., 2015). Trauma, ischemia and neurodegenerative diseases such as Parkinson’s disease (PD), Alzheimer’s disease (AD), Huntington’s disease (HD) and Amyotrophic Lateral Sclerosis (ALS) are the leading causes of long-term neurological disability (Ouyang, Xu, Yue, Liu, & Giffard, 2014; Saxena & Caroni, 2011), resulting in impaired motor and cognitive behavior (Schulze et al., 2011).

Up until now, there are no effective available pharmacological and surgical therapies to halt or reverse the course of neuron degeneration (Kumar & Singh, 2015; Schapira, Olanow, Greenamyre, & Bezard, 2014). The World Health Organization (WHO) predicted, in its Neurology Atlas published in 2004, that by 2040, as many developed countries' population gets older, neurodegenerative diseases will surpass cancer and become the second worldwide leading cause of death, after cardiovascular disease. Thus, it becomes crucial to study and develop novel therapeutic mechanisms, in order to successfully counteract this tendency.

To efficiently address neurodegenerative conditions, exceptional measures are required, since the central nervous system (CNS) presents numerous obstacles to an effective treatment, namely a successful and specific delivery of the therapeutic product. Some of the considered routes of administration include the intraparenchymal, intraventricular and intrathecal injection, which are potentially hazardous techniques associated with safety concerns (Haque et al., 2012), and the intranasal, intravenous and intra-arterial administration, which have less associated risks. and non-invasive techniques like intranasal administration (Balyasnikova et al., 2014). The later are obviously more desirable, as long as they assure a successful delivery to the target cells. In order to accomplish successful systemic administration (either by intravenous or intra-arterial injection), therapeutic molecules are often required to overcome the main interface between blood and brain parenchyma, the blood–brain barrier (BBB) (Pardridge, 2012). The BBB is a non-permeable specialized barrier in cerebral microvessels that consists of a thick basement membrane, endothelial cells connected by tight junctions and astrocytic endfeet. The tight junctions between endothelial cells, alongside enzymes, transporters, and efflux pumps of the multidrug resistance (MDR) pathways, control and hinder the access of molecules to the brain (Neuwelt et al., 2011). Although the BBB has a very important protective role, it results in the exclusion of 98% of small-molecule drugs and approximately 100% of large-molecule neurotherapeutics from the brain parenchyma (Pardridge, 2005). As to non-invasive intranasal administration, therapeutic products may directly reach the CNS, via the olfactory nerve or the trigeminal nerve, thus bypassing the BBB (Ruigrok & de Lange, 2015). Regardless of the need to surpass the BBB, it is also of importance the fate of the therapeutic molecule once inside the CNS. The existence of different cell types such as neurons (encompassing different neuronal sub-types), microglia, astrocytes and oligodendrocytes, with complex interconnections but specialized roles, highlights the importance and potential benefits of targeting therapeutic molecules to specific cells. In addition, in the PNS, peripheral neuropathies must also be addressed by a specifically targeted therapeutic system. Specific neuronal targeting can be integrated into the therapeutic system, such as by the use of neuro-targeting peptides and neurotoxins, in order to diminish off-target effects and assure an efficient treatment (Chu, Schellinger, Bocek, Johnson, & Pun, 2013; Oliveira, Fernandez, et al., 2010).

A number of several different strategies have been studied towards the goal of neuroprotection and neuroregeneration. Examples are drug delivery (mostly compounds involved in the modulation of apoptosis, inflammation and oxidative stress mechanisms), cell-based therapies (both somatic and stem cells have been studied), tissue engineering (the diversity of biomaterials considered can be divided into hydrogels and nanofibers), gene therapies (in which cDNA or RNAi represent pharmacological agents) and also combinatorial approaches (Kabu, Gao, Kwon, & Labhasetwar, 2015).

1.3.1. STRATEGIES FOR NEURONAL TARGETING

Specific delivery of nanotools can be accomplished by conjugation of the structure with targeting moieties that will interact with cell surface molecules. Several different strategies have been used to direct nanostructures to neuronal cells, taking advantage of all kinds of receptors present at the cell membrane.

For instance, it has been described that poly-L-lysine crosslinked with neurotensin, a 13 amino acid neuropeptide, was able to specifically transfect cells expressing the high-affinity neurotensin receptor, undergoing rapid internalization once bound to the receptor (Martinez-Fong et al., 1999). Furthermore, Hernandez-Chan and coworkers have recently demonstrated that neurotensin-polyplex-mediated BDNF transfection of dopaminergic neurons allowed for partial biochemical, structural, and behavioral recovery from early parkinsonism in rats (Hernandez-Chan et al., 2015).

Another interesting approach is the targeting of upregulated molecules in injured neuronal cells, as is the case of the p75NTR (neurotrophin receptor), which has been proved to be upregulated in peripheral nerves upon injury (Rende, Giambanco, Buratta, & Tonali, 1995) and in ALS (Seeburger, Tarras, Natter, & Springer, 1993). A DNA carrier system composed of PEG-PEI conjugated to an antibody (MLR2) to p75NTR specifically transfected mouse motor neurons *in vivo* after retrograde transport upon intraperitoneal injection (Rogers et al., 2014).

Recently, a new four amino acid peptide, CAQK, discovered by *in vivo* phage display has proved to specifically target injured mouse and human brain, through a proteoglycan complex upregulated upon injuries. Systemically administered CAQK-silicon nanoparticles carrying siRNA molecules successfully demonstrated specific gene silencing in injured brain sections (Mann et al., 2016).

Neuron-targeting has also been exploited using the Tetanus toxin (TeNT) pathway, through binding to gangliosides (GD1b and GT1b) present in the neuronal cell surface. This toxin is a bacterial protein composed of a heavy chain – TeNT Hc, a nontoxic portion responsible for neuron recognition – and a light chain – TeNT Lc, a metalloprotease that interferes with neurotransmission (Ahnert-Hilger et al., 1990; Shapiro et al., 1997). Neuron-specific delivery, as well as retrograde transport, have been accomplished by the use of the C-fragment of the TeNT Hc (Bizzini, Stoeckel, & Schwab, 1977; Coen, Osta, Maury, & Brûlet, 1997). Conjugated to PLGA-PEG nanoparticles, this fragment demonstrated the specificity to neuronal cells delivery, resulting in a six-fold increased binding of the TeNT Hc tagged nanoparticles to neuroblastoma cells when comparing with liver cells (Townsend et al., 2007). Likewise, a PEI-based vector functionalized with the Hc fragment demonstrated targeted and specific transfection of neuronal cell lines and primary dorsal root ganglion (DRG) cultures, with a significant decrease of internalization by a fibroblast cell line (NIH 3T3) (Oliveira, Pires, et al., 2010).

Phage display against GT1b has allowed the identification of a peptide with binding properties analogous to the ones of TeNT Hc fragment, with the additional feature of not presenting immunogenicity (J. K. Liu et al., 2005). This 12 amino acid peptide, referred to as Tet1 peptide (sequence HLNILSTLWKYR), has proven to be a neuron-targeting moiety, capable of retrograde transport, with high binding affinity to differentiated PC-12, DRGs and primary motor neurons (Federici, Liu, Teng, Yang, & Boulis, 2007; J. K. Liu et al., 2005). In a later work, Tet1-PEG-PEI conjugates were found to exclusively transfect neural progenitor cells from a heterogeneous population composed of neural progenitor cells, microglia, glial progenitors and astrocytes (Kwon et al., 2010).

1.3.2. POTENTIAL OF DNA-BASED DELIVERY VECTORS FOR NEUROTHERAPEUTIC AGENTS

Featuring controllable size and architecture, atomic-scale addressability and biocompatibility, DNA nanostructures represent powerful and promising tools as “smart” delivery vehicles. A diversity of different biologically active compounds or agents can be chemically or physically loaded with ease into DNA nanostructures, which can further improve the physicochemical and pharmacological properties of the cargo and selectively deliver the bioactive payload to the target. These delivery vehicles present a high capacity of cargo loading, capable of covalent functionalization, simple hybridization with other nucleic acids and encapsulation of different kinds of payloads (Lee et al., 2012; Mohri et al., 2012; Q. Zhang et al., 2014).

For instance, RNAi, which is becoming an increasingly popular therapeutic strategy for a range of acquired and inherited diseases, would benefit from a delivery system with such characteristics. siRNA can be used as a therapy in neurological disorders for which repression of key genes may provide clinical benefit, as for instance BACE1, predicted to promote amyloidogenic peptide formation in AD (Singer et al., 2005), mutated SOD1 (CuZn-superoxide dismutase) in ALS (Ralph et al., 2005), EGFR (epidermal growth factor receptor) and β-catenin in glioma (Kui Wang, Park, & Zhang, 2013) and PTEN upon neuronal injury (N. Chang, El-Hayek, Gomez, & Wan, 2007). Its wide potential has promised to revolutionize the neurotherapeutics field (Davidson & Paulson, 2016), however, efficient delivery of therapeutic nucleic acids continues to be a challenge mostly due to the lack of an effective delivery system.

Due to their inherent hydrophilicity and net negative charge, siRNA molecules are excluded from entering through cellular membranes. In addition, their relatively small sizes lead to rapid clearance from circulation. As such, the successful application of siRNAs as therapeutic agents requires the combination of chemically and structurally optimized siRNA with a delivery system that would improve its physicochemical and pharmacological properties (Dominska & Dykxhoorn, 2010). In order to administer siRNA systemically, and allow it to cross the physiological barriers for reaching its site of action without adverse effects, delivery systems should, ideally, present the following characteristics: low toxicity profile; serum stability; ability to evade the immune system; ability to resist renal clearance; avoid interactions with non-target cells; permit target cell entry and endosome escape; efficient cytoplasmic unpacking, allowing siRNA uptake into RISC (Whitehead, Langer, & Anderson, 2009).

DNA nanostructures, combining a plethora of distinctive characteristics, can represent such a promising solution: a delivery vehicle that can easily incorporate therapeutic siRNAs by straightforward annealing, with enhanced serum stability, minimal cytotoxicity and immunogenicity and rapid cell internalization for an improved silencing effect (Charoenphol & Bermudez, 2014; Lee et al., 2012).

It is worth mentioning that in the case of delivery of functional nucleic acids such as antisense oligonucleotides, siRNA and aptamers, the delivery system and the cargo are essentially the same type of molecule. As such, it is critical to take into account architectural disposition, to avoid undesired interactions between them (Tintoré et al., 2014). This can be achieved by *in silico* design studies using some of the previously mentioned computational tools.

Targeted drug delivery will, as well, benefit from such a predictable and controllable nanoconstruct, that can be designed to fit current needs in the field. In neurotherapeutics, several compounds have been proved to have clinical relevance, among these, anticancer drugs like carmustine (BCNU) (Westphal et al., 2003), methotrexate (Morris & Abrey, 2009) and doxorubicin (Dox), as well as therapeutic molecules targeting neurodegeneration like rivastigmine in AD (Z.-Z. Yang et al., 2013). Nerve growth factors-based therapies have also been suggested as promising approaches in regenerative medicine applications. For instance, the delivery of VEGF (vascular endothelial growth factor) has been reported to promote the maintenance and regrowth of injured ischemic axons (Shvartsman et al., 2014), while GDNF (glial cell line-derived neurotrophic factor), was reported to increase the number of motor neurons regenerating their axons after chronic axotomy (Boyd & Gordon, 2003).

Chang and co-workers reported a DNA icosahedron assembled from aptamer-conjugated six-point-star motifs in which Dox was intercalated. The Mucin-1 aptamer on this polyhedron allowed the targeting of epithelial cancer cells with specific improved cytotoxicity (M. Chang et al., 2011). A different concept, defined as DNA nanotrain was also reported, in which two complementary DNA strands alternatively bind to each other upon initiation from a DNA aptamer and form a long linear assembly, schematically resembling long train tracks **(Fig. 7a)**. Dox was then intercalated into the formed DNA double helix. The Dox-“DNA nanotrain” complex, by specifically targeting cancer cells, revealed stronger *in vivo* anti-tumor efficacy and reduced side effects in a mouse xenograft tumor model in comparison to free Dox (G. Zhu et al., 2013).

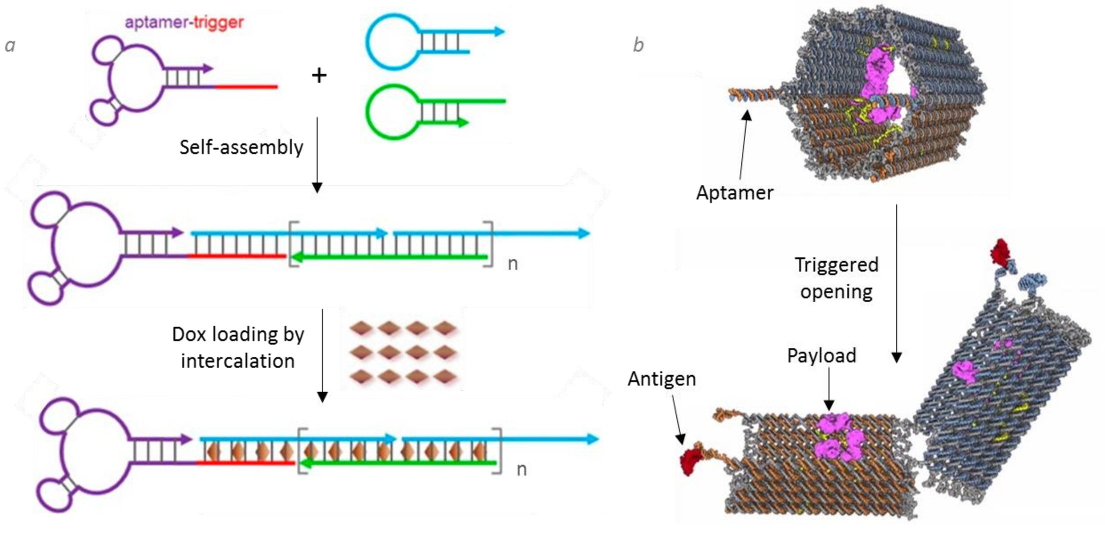

Figure 7 (a) Schematic representation of the self-assembly of DNA nanotrains from two short DNA strands upon initiation from a targeting aptamer. Resultant nanotrains were loaded with Dox by intercalation (Adapted from G. Zhu et al., 2013). *(b) DNA nanorobot schematic representation in a closed (top) and open (bottom) conformation. In the presence of the target antigen, the aptamer will bind it, displacing the complementary strand and opening the structure for payload exposure (Adapted from* Douglas et al., 2012).

A key feature of DNA-based nanostructures is the possibility to address selected positions within the 2D or 3D nanostructures with atomic-scale accuracy, and precisely incorporate fluorophores, chemical reactive groups, proteins, etc. Erben and co-researchers have reported the successful encapsulation of a single molecule of cytochrome c within a TDN, by precisely controlling the attachment site, and thus modulating the position of the protein relative to the tetrahedron (Erben, Goodman, & Turberfield, 2006). In another report, cytochrome c and azurin have been described to assemble into separate TDNs, through the formation of DNA-PNA-protein complexes, while maintaining the protein's secondary structure and catalytic activity (Flory et al., 2014).

Controlled release is a major aim of smart drug delivery systems and also a mean to improve the performance of therapeutic cargoes. The superior control over DNA-based structures and integration of DNA-based molecular mechanisms potentiates intelligent trigger-controlled release of bioactive molecules (Krishnan & Simmel, 2011). Control mechanisms can be introduced by the use of aptamers, as these molecules 1) bind in a highly specific manner to a given antigen, and can be specifically tuned for certain diseases, 2) can switch conformation upon binding/unbinding of ligand and 3) are easily incorporated into a DNA structure. For instance, a smart logic-gated DNA origami nanorobot with two aptamers specific to two receptors localized on the cell membrane, was able to open and release the payload once both targets were detected, emulating an "AND" logic gate (Douglas et al., 2012) **(Fig. 7b)**. Another possible control mechanism makes use of the i-motif DNA structure, a quadruplex structure that forms due to base pairing between protonated and unprotonated cytosines sequences at low pH and disassembles at neutral or basic pH (Benabou, Avino, Eritja, Gonzalez, & Gargallo, 2014). For example, i-motif sequences have been introduced into a TDN structure allowing structure disassembly at low pH ("open" state) and release of a model protein cargo (GFP) (Keum & Bermudez, 2012). Also dynamic mechanisms can be introduced by use of DNA strand-displacement technology, a process through which two strands with partial or full complementarity hybridize to each other, displacing one or more pre-hybridized strands in the process (D. Y. Zhang & Seelig, 2011). For instance, by incorporating overhang sequences in its design, a DNA nanocube has been reported to be able to unfold/disassemble in presence of a specific prostate cancer mRNA trigger sequence (complementary to the overhangs) (Bujold et al., 2014).

1.3.3. POTENTIAL OF DNA-BASED SMART SENSING DEVICES IN NEUROTHERAPEUTICS

DNA nanotechnology represents a full-of-potential approach for the construction and application into intelligent sensing devices. Owing to the inherent characteristics of DNA-based structures, their use as imaging diagnostic probes allows for an enhanced control over spatial distribution of detector molecules, rendering a quantitative and ultrasensitive target detection mechanism (Wen et al., 2012).

Molecular beacon-based imaging, for instance, has been recently suggested as a promising diagnostics strategy in neurotherapeutics (Østergaard et al., 2015), and can be easily incorporated into DNA-based nanostructures. Molecular beacons are single-stranded nucleic acid hairpin probes with a stem structure that incorporates a fluorophore and a quencher, in the 5' and 3' end, respectively (Tyagi & Kramer, 1996). These probes allow for specific nucleic acids sequence detection through sequence matching between the target and the single-stranded loop domain. In the absence of the target, FRET occurs between the fluorophore and the quenching molecule. Upon hybridization to the target, the stem portion dissociates and the resulting increased distance between fluorophore and quenching molecule results in a detectable fluorescence signal (Tyagi & Kramer, 1996; Kemin Wang et al., 2009). However, the success of molecular beacons has been hindered by their inability to cross cell membranes without transfection reagents and by the nonspecific degradation by intracellular enzymes (Y. Kim, Sohn, & Tan, 2008; Kemin Wang et al., 2009).

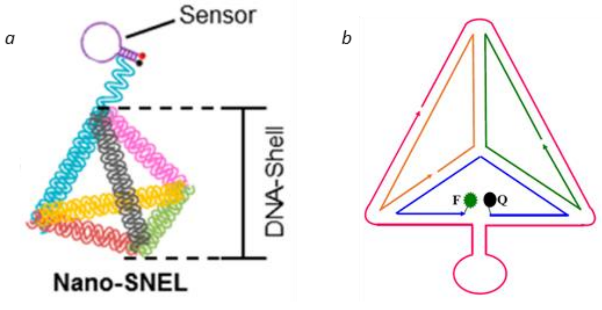

Figure 8 (a) Schematic representation of nano-SNEL, with the molecular beacon sensor indicated and its fluorophore and quencher molecules in red and black, respectively (Adapted from Tay et al., 2015). *(b) Schematic representation of the DTMB (DNA tetrahedron-based molecular beacon with the loop and stem portions incorporated in one of the sequences, and the fluorophore (F) and quencher (Q) incorporated in another sequence* (Adapted from Xie et al., 2016).

A system that conjugates the unsurpassed characteristics of DNA-nanotechnology and the ability of molecular beacons may counteract these limitations, providing a straight-forward reliable and specific detection platform. The incorporation of a molecular beacon into a DNA-nanostructure would result in a system with facilitated cell entry, enabling the access to target molecules, and with enhanced resistance to degradation, which leads to fewer false positive results.

Specifically, the use of molecular beacons targeting microRNAs (miRNA) enables the monitoring of gene expression and miRNA expression patterns in living cells through a non-invasive manner, representing an efficient and reliable tool as biomarkers for diagnostic purposes. Several human diseases have been proved to present an aberrant expression of miRNAs and a distinctive expression profile through temporal progression, among them, some nervous system associated disorders (B. Zhang & Farwell, 2008). Through the use of molecular beacons, the assessment of distinctive miRNA expression patterns would allow a more precise detection and monitoring of such diseases.

For instance, in AD, miR-9 and miR-128 have a significant higher expression when comparing with healthy adults (Lukiw, 2007), while miR-153, that targets the amyloid-β (Aβ) precursor protein 3'-UTR, is decreased (Long, Ray, & Lahiri, 2012). PD patients have a deficiency in miR-133, known to regulate the maturation and function of midbrain dopaminergic neurons (J. Kim et al., 2007), and in miR-34b/c at early stages of the disease, thought to trigger mitochondrial dysfunction and oxidative stress in dopaminergic neurons (Miñones-Moyano et al., 2011). Patients with ALS, a disease that specifically affects upper and lower motor neurons, present a down-regulation of miR-9, a miRNA which was proved to target the heavy neurofilament subunit of motor neurons (Haramati et al., 2010). Additionally, in cerebral ischemia, several miRNAs were identified to be significantly altered when comparing with healthy subjects, and more specifically miR-125b-2, miR-27a, miR-422a, miR-488 and miR-627 are indicated to be upregulated in acute ischemia, and thus can be used for diagnosis (Sepramaniam et al., 2014).

This strategy has been recently adopted outside the neurotherapeutics field by Tay and co-researchers, for the construction of a nano-SNEL ("nano-snail-inspired nucleic acid locator") whereby a GAPDH-specific molecular beacon is conjugated to one vertex of a TDN serving as a "nanoshell" **(Fig. 8a)**. This group proved that the nano-SNEL presents a substantial improvement in resistance to enzyme degradation and enhanced cellular internalization, with resulting increased efficacy (Tay, Yuan, & Leong, 2015). Soon after, another research group has also studied the use of a TDN-based molecular beacon, this time adopting a different structural strategy by incorporating the molecular beacon in the tetrahedron structure for tumor-related TK1 detection **(Fig. 8b)**. This system confirmed the enhanced stability against enzymes as well as intracellular delivery, when compared with the nude molecular beacon (Xie et al., 2016).

1.3.4. DNA-BASED THERANOSTICS PLATFORM

A theranostic system integrating targeting ligands, imaging features and bioactive compounds could realize combinatorial diagnosis and therapy for more appropriate and efficient clinical applications. DNA-based nanostructures hold great promises towards that end, taking advantage from their inherent and remarkable characteristics: ease of multi-functionalization, capacity to load a wide variety of therapeutic molecules, atomic-scale precision. Some of the aforementioned DNA nanodevices represent an important step towards the development of a theranostic platform, including sensing interfaces that can trigger the release of a therapeutic moiety.

Setyawati and co-researchers already developed a DNA-based theranostic platform through the use of a TDN with incorporated glutathione-protected gold nanoclusters allowing bacterial detection, and intercalated actinomycin D for antibacterial activity. This system represents a basic yet effective theranostic platform for bacterial infections, given the successful results in detecting and killing model bacteria *Escherichia coli* and *Staphylococcus aureus* (Setyawati et al., 2014).

Bachelet and co-workers went further ahead, taking advantage of the previously introduced logic-gated structures (AND, OR and XOR) **(Fig. 9)**. The team developed a series of different DNA origami robots capable of dynamic interactions with each other, generating logical outputs, which are translated into the release or not of molecular payloads. These DNA robots were tested both *in vitro* and in living *Blaberus discoidalis,* revealing encouraging results for a possible application in which a tailored therapeutic response is needed according to the diagnosis, as for instance the release of different drugs according to a specific disease state (Amir et al., 2014).

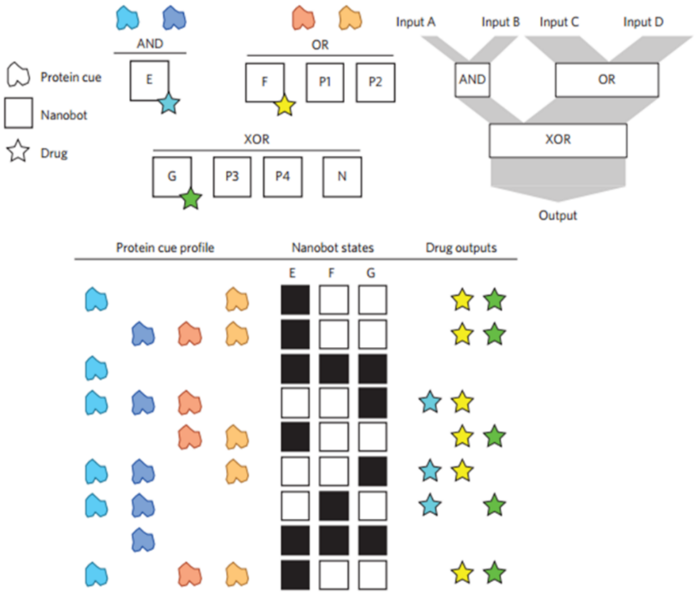

Figure 9 Scheme of the eight different robot types, each presenting its own task: three effector robots E, F and G, carrying a different drug; four positive regulators, P1 and P2 as opening keys to F, P3 and P4 as opening keys to G; and a negative regulator N that inactivates G opening. Two first-layer gates, AND and OR, control their own drug release and the release of a third drug on a second-layer gate, XOR (top). Examples of distinct drug combinations according to different protein cues present are represented (bottom) (Amir et al., 2014).

AIM OF THE THESIS

DNA nanotechnology has been regarded by the scientific community as a full-of-potential approach for meeting most current requirements in biomedicine. The predictability associated with Watson&Crick base-pairing rules, versatility of assembly, modularity and specific functionalization, adding on to the biodegradability and biocompatibility of these structures are features allowing the development of efficient and smart drug delivery vehicles as well as novel sensitive biosensors.

The answer to current challenges in the delivery of therapeutic molecules or biosensensing devices might be enclosed in DNA nanotechnology. Together with the unique ability of straight-forward atomic-scale precision, this type of nanoconstructs are soluble, biodegradable, biocompatible, presenting enhanced resistance to degradation and cell internalization. Along these lines, DNA-based nanostructures hold great promise for nanomedicine applications.

The aim of this thesis was to design and develop of a novel neuronal targeting DNA-based nanostructure to be applied either in neurotherapeutics delivery, molecular biosensing or in a theranostic platform.

In order to accomplish this, novel DNA sequences were firstly designed in order to efficiently assemble into a tetrahedral structure and further functionalized with a neuronal-targeting peptide. The functionalization strategy was based on the use of PNA-conjugated targeting peptides to achieve a simple and stable hybridization with single-stranded DNA “anchors” present in the assembled tetrahedral structure.

Specific tasks of this thesis were outlined as follows:

1. Optimization of assembly and purification protocols using a previously reported tetrahedral DNA nanostructure (TDN);
2. Design of novel efficient TDN sequences, using available computer-assisted design;
3. Assembly, purification and characterization of the newly designed TDN;
4. Functionalization of TDN with the neuronal targeting ligand – Tet1 peptide;
5. Assessment of *in vitro* specific uptake by neuronal cells.

CHAPTER 2

MATERIALS AND METHODS

2.1. MATERIALS
2.2. IN SILICO DESIGN OF NOVEL TDN2 SEQUENCES
2.3. ASSEMBLY AND PURIFICATION OF TDNS
2.4. CHARACTERIZATION OF TDNS
    2.4.1. PAGE ANALYSIS
    2.4.2. DYNAMIC LIGHT SCATTERING
    2.4.3. ATOMIC FORCE MICROSCOPY
2.5. ASSEMBLY AND CHARACTERIZATION OF TDN-TET1 SYSTEM
2.6. CELL CULTURE
    2.6.1. ND7/23 DIFFERENTIATION
    2.6.2. IMMUNOCYTOCHEMISTRY
2.7. CELLULAR ASSOCIATION AND UPTAKE STUDIES
    2.7.1. CONFOCAL MICROSCOPY ANALYSIS
    2.7.2. FLOW CYTOMETRY ANALYSIS
    2.7.3. IMAGE STREAM ANALYSIS
2.8. STATISTICAL ANALYSIS

2.1. MATERIALS

All oligonucleotide sequences (PAGE or HPLC purified) were purchased from Integrated DNA Technologies. PNA-Tet1 peptide conjugate was purchased from Panagene, dissolved in 10% DMSO, and also used with no further purification.

Tetrahedron 1 (TDN1) sequences:

s1a: 5'- /5Cy3/AGG CAG TTG AGA CGA ACA TTC CTA AGT CTG AAA TTT ATC ACC CGC CAT AGT AGA CGT ATC ACC
s2a: 5'- / CTT GCT ACA CGA TTC AGA CTT AGG AAT GTT CGA CAT GCG AGG GTC CAA TAC CGA CGA TTA CAG
s3a: 5'- /GGT GAT AAA ACG TGT AGC AAG CTG TAA TCG ACG GGA AGA GCA TGC CCA TCC ACT ACT ATG GCG
s4a: 5'- /5Cy5/CCT CGC ATG ACT CAA CTG CCT GGT GAT ACG AGG ATG GGC ATG CTC TTC CCG ACG GTA TTG GAC

Tetrahedron 2 (TDN2) sequences:

FAM-s1b: 5'- /56-FAM[1]//iSpC3[2]/GCA CTT ACG GAG GGA TGA GGA GCG TCC GAC GGC CGG TCA CCA ACC CTT AAC GAA ATT TGT GCC AAT AAT GAC TAA*[3] A* A -3'
FAM-s2b: 5'- /56-FAM/CCT CAT CCC TCC GTA AGT GCA CTG ACT AGG CGA GTC GTC ACA CCT ACC AGG GAG CGC GGC CGC AAT AAT GAC TAA* A* A -3'
FAM-s3b: 5'- /56-FAM//iSpC3/GTG ACG ACT CGC CTA GTC AGA GCA CAA ATT TCG TTA AGG GTA CGG TTA CGA CCT CCT ACC TGC AAT AAT GAC TA* A* A -3'
FAM-s4b: 5'- /56-FAM//iSpC3/GGT GAC CGG CCG TCG GAC GCA CGG CCG CGC TCC CTG GTA GGA CAG GTC GGA GGT CGT AAC CG -3'

Biotin-Linker (Biot-ON):5'- 5Biosg[4]/TTT TCA ATA ATG ACT AAA A -3'

Reverse complementary DNA linker for StvBiot studies (rcON): 5'- TTT TAG TCA TTA TTG AAA A -3'

Reverse complementary DNA linker for TDN2 anchors studies (rc18): 5'- CGC TTT TAG TCA TTA TTG -3'

PNA-Tet1 conjugate: N-term /HLNILSTLWKYR-OOO[5]-TTT TAG TCA TTA TTG/ C-term

2.2. IN SILICO DESIGN OF NOVEL TDN2 SEQUENCES

The NUPACK web application software (Zadeh et al., 2011) was used for the analysis and design of the DNA sequences forming the TDN2. The input design code and representation of predicted sub-structures are shown in the supplementary information.

---

[1] 5' 6-FAM (carboxyfluorescein), a commonly used fluorescent dye for labeling oligonucleotides.

[2] Internal C3 Spacer phosphoramidite, a three carbon spacer arm introduced in the sequences bearing a FAM molecule and starting with a guanine base, due to reported fluorescence quenching by adjacent guanosine nucleotides.

[3] A* indicates a phosphorothioate bond, which is a substitution of a sulfur atom for a non-bridging oxygen in the phosphate backbone. This modification renders the internucleotide linkage resistant to nuclease degradation.

[4] 5' Biotin, a tag added to the 5' of the DNA molecule.

[5] O-linker is a glycol linker of nine atoms used to distance the hybridization portion of the molecule from the peptide. 3 O-linkers were introduced, as recommended, since the conjugation was done at the N-terminus of the PNA molecule.

2.3. ASSEMBLY AND PURIFICATION OF TDNS

DNA sequences were previously studied and designed to optimally assemble into tetrahedrons by annealing. In order to obtain such structures, stoichiometric quantities of the component DNA strands were mixed in filtered 1x TM buffer (Tris 10 mM $MgCl_2$ 5 mM in milli-Q water, pH 7,5) at a final concentration of 1 µM. Assembly was done in a Biometra® TPersonal Thermocycler with the following program: equimolar mixed DNA strands were heated at 95˚C for 3 min and cooled down to 4˚C at a rate of 3˚C/s (optimized conditions).

For purification, assembled DNA structures were run at 4˚C in 6% poly-acrylamide gels at 50V for 150 min, in TBE 1x + 12,5 mM $MgAc_2$. The TDN band on the gel was detected by the UV shadowing technique, which allows the visualization of unlabeled, dye-free DNA molecules **(Fig. 10)**. The TDN band on the gel was then excised for purification.

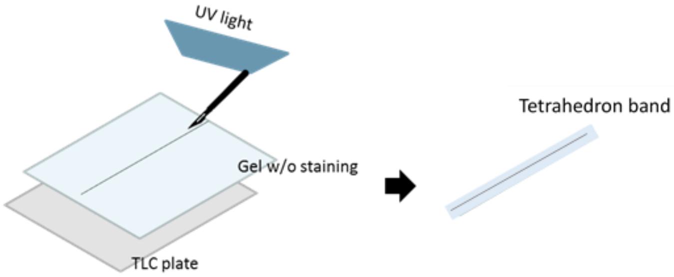

Figure 10 UV shadowing technique. In this technique, the gel is placed on plastic wrap over a silica-coated TLC plate on which UV light is shone upon. The dye in the UV-fluorescent plate is excited, while nucleic acids absorb the light, casting a shadow against the fluorescent background.

Two different purification protocols were followed: i) Spin-X method: gel pieces were placed into a Spin-X centrifugal tube filter (Corning® Life Sciences) and frozen at -80˚C for 15 min. Then, TM buffer was added immediately before centrifugation for 20 min at 13’000 xg. Flow-through was removed and another centrifugation was carried out for an additional 10 min; ii) Crush&Soak method (testing for different gel processing and soaking conditions, as follows): gel pieces were either cut manually with a scalpel into smaller pieces or centrifuged (13’000 xg for 1 min; RT) through a 0,6 mL eppendorf tube previously punctured with a needle to create a hole in the bottom. TM buffer was then added in a volume equal to 3 times the one occupied by the gel pieces and left soaking for 24 h or 48 h at 4˚C in a tube rotator. The gel slurry was centrifuged again at 13’000 xg for 3 min for collection of the DNA containing supernatant solution. Finally, both the supernatant (to remove small polyacrylamide fragments still present in solution) and gel slurry (to maximize liquid extraction from the gel slurry and increase DNA recovery) were run through a Spin-X filter. Both flow-throughs were combined at the end of the Spin-X centrifugation steps.

After analyzing the efficiency of each method, the choice of protocol for purification lied on the Crush&Soak method with manual cutting of the gel pieces and 48 h of incubation in soaking buffer **(Fig. 11)**.

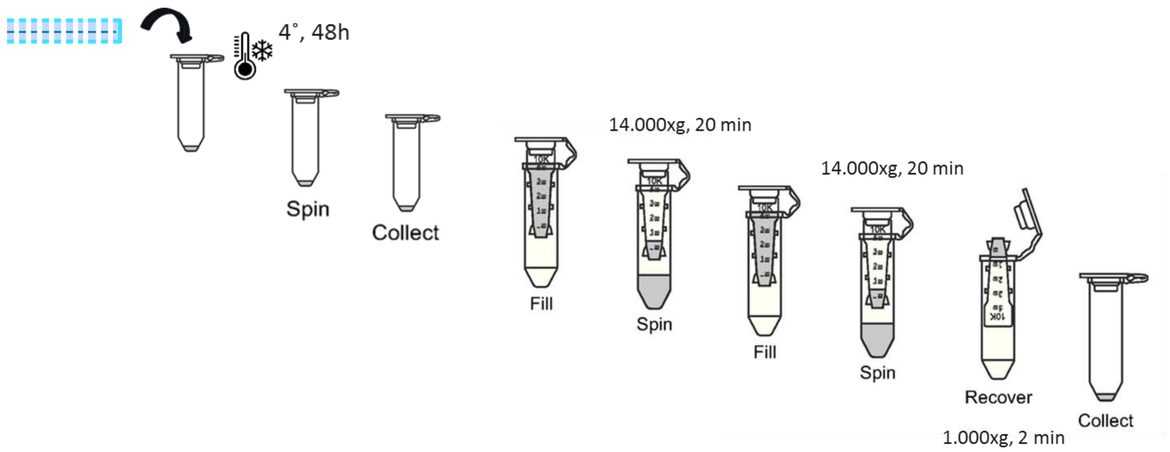

Figure 11 Summary of the optimized TDN purification protocol. The first four steps consist of the optimized Crush&Soak protocol, with a manual cutting of the pieces and an incubation time of 48 h at 4˚C. The following steps correspond to the buffer exchange protocol, using Amicon centrifugal filter devices.

For buffer exchange and concentration, Amicon® centrifugal filter devices were used **(Fig. 11)**. These were previously rinsed with TM buffer 1x, according to manufacturer's instructions, and then TDN purified solution was added to the column and centrifuged for 20 min at 14'000 xg. The sample was washed with TM buffer 1x and centrifuged for an additional 20 min at 14'000 xg. The concentrated sample was then collected by inverting the upper part of the column and centrifuging for 2 min at 1'000xg.

2.4. CHARACTERIZATION OF TDNS

2.4.1. GEL ELECTROPHORESIS ANALYSIS

Hybridization between strands was observed by gel electrophoresis, running individual and hybridized strands in 6% acrylamide gels in 1x TBE with 12,5 mM $MgAc_2$ at 4˚C, for 90 min at 70V (BIO-RAD system). Band detection and visualization was done by staining with SYBR® Gold (Thermo Fisher Scientific), using GeneRuler™ Low Range DNA Ladder (Thermo Fisher Scientific) or GeneRuler 100bp Plus DNA Ladder (Thermo Fisher Scientific) for size comparison. Gels were imaged in a GEL-Doc XR+ system (BioRad).

Image analysis was performed in Fiji (SciJava). Assembly yields of TDNs were calculated by quantifying relative band intensities in the gel with ImageJ, normalizing with respect to the appropriate size of the structure, according to previously published literature (Greene, Keum, & Bermudez, 2012). This should be done due to the fact that the gel staining signal is proportional to the mass of dsDNA, thus the expected ratio of the TDN (4 strands) to a 2-strand structure is 4:2, while for higher mass structures (about which there is no knowledge on the number of strands) a relative mass ratio is obtained according to the size given by the DNA ladder.

2.4.2. DYNAMIC LIGHT SCATTERING

Size analysis was performed in a Zetasizer Nano ZS (Malvern), using a High concentration quartz zeta cell ZEN1010 (Malvern). Samples were filtered using a Spin-X tube before analyzing. Measured sample concentration was around 2 µM. All measurements were carried out in triplicate at 25˚C.

2.4.3. ATOMIC FORCE MICROSCOPY

AFM experiments were carried out using a FastScan Bio AFM system (Bruker). For analysis of TDNs by AFM, 100 µl of $NiCl_2$ 20 mM were added to a freshly cleaved mica allowing the Ni^{2+} ions to bind the mica surface for about 2 min. The DNA sample was then added to the $NiCl_2$ drop on the mica, at a final concentration of 10 nM, mixing both solutions. After 20 min, the sample was immediately analyzed in liquid with a FastScan-B probe (Bruker).

2.5. ASSEMBLY AND CHARACTERIZATION OF TDN-TETT1 SYSTEM

Purified TDNs were mixed in an optimized ratio of 1:5 with PNA-Tet1 conjugates in the presence of TM buffer 1x, with additional 1% DMSO for an increased solubility of the PNA-Tet1 conjugate in the solution. Hybridization proceeded for 1h at RT.

In order to characterize the system, hybridized TDNs with the PNA-Tet1 conjugates were run in 6% acrylamide gels in TBE 1x at 4˚C, for 90 min at 70V.

2.6. CELL CULTURE

ND7/23 cells were grown in Dulbecco's Modified Eagle Medium (DMEM) with GlutaMax (Gibco), supplemented with 10% FBS and 1% P/S. Cells were passaged every 3-4 days at a ratio of 1:15. NIH 3T3 cells were grown in the same medium conditions, and passaged every 3 days at a ratio of 1:20.

2.6.1. ND7/23 DIFFERENTIATION

ND7/23 cells differentiation was accomplished by culturing the cells in a pre-treated surface, coated with laminin-111 at 20 µg/ml for 3 h at 37 ˚C. Cells were cultured for 7 days in DMEM F12 supplemented with 2% b27 (Invitrogen), 1% P/S (Gibco), 2 µg/ml NGF (Merck Millipore) and 1 mM of dbcAMP (Sigma-Aldrich). Medium was changed every 3 days. For microscopy visualization, 2500 cells/well were seeded in µ-Slide 8 Well, ibiTreat (Ibidi®), while for Flow Cytometry analysis, 15000 cells/well were seeded in a 20-well plate.

2.6.2. IMMUNOCYTOCHEMISTRY

For microscopy analysis, medium was removed from cells, these were washed 3 times with PBS and fixed with either paraformaldehyde (PFA) or formaldehyde (FA) 3.7% for 15 min. Permeabilization was done using PBS with Triton 0.2% for 10 min, followed by blocking with PBS BSA 1% (w/v) for 30 min. Primary antibodies were added, and cells were incubated overnight at 4˚C. Cells were then washed 3 times with PBS, secondary antibodies were added and incubated for 1 hour at RT, followed by Hoechst for 10 min, after which 3 additional washes were done. Samples were then analyzed by inverted fluorescence microscopy (Zeiss Axiovert 200 MAT) or confocal microscopy.

For flow cytometry analysis, cells were trypsinized and cell number was adjusted to 1-5x10^6 cells/ml after which blocking solution (ice cold PBS BSA 1% (w/v)) was added with incubation proceeding for 30 min on ice. Cells were collected by centrifuging at 1500 rpm for 5 min at 4˚C, after which primary antibodies were added for 40 min at 4˚C. Cells were washed 3 times with PSB and incubated with secondary antibodies for an additional 40 min, after which they were washed again and re-suspended in PBS for further analysis.

Mouse anti-Neurofilament-Heavy (Santa Cruz) was used in a ratio of 1:100, mouse anti-Gt1b (Merck Millipore) was used in a ratio of 1:100 for both microscopy and flow cytometry, secondary anti-mouse 488 was used in a ratio of 1:1000 for microscopy and 1:4000 for flow cytometry analysis, while secondary anti-mouse 594 was used in a ratio of 1:1000 in PBS BSA 1% (w/v). Hoescht was used in a 1:20000 ratio from a 10mg/ml aliquot in PBS.

2.7. CELLULAR ASSOCIATION AND UPTAKE STUDIES

2.7.1. CONFOCAL MICROSCOPY ANALYSIS

Analysis was performed in a Leica TCS SP5 (Leica Microsystems). To assess the targeting efficiency of the PNA-Tet1 conjugate, 16 µg of Streptavidin-Alexa488 (Invitrogen) was mixed in a ratio of 1:1 with a Biotin-oligonucleotide (Biot-ON) conjugate bearing a complementary sequence to the PNA-Tet1. After 30 min of incubation at RT, PNA-Tet1 conjugates were added to the mixture in a 1:5 ratio, incubating for an additional 30 min at RT, in 1x TM buffer with 1% DMSO. Systems were incubated with cells in DMEM for 4 hours, after which cells were washed with PBS, fixed and treated for further analysis.

Fluorescently labeled TDNs, bearing one FAM molecule per DNA strand, were mixed in a 1:5 ratio with PNA-Tet1 conjugates (in TM buffer 1x, 1% DMSO). Samples were then added to differentiated ND7/23 cells at a final concentration of 0.025 µM or 0.05 µM in Hank's Balanced Salt Solution (HBSS, Gibco). One, two or three hours later (according to specified), cells were washed with PBS, fixed and treated for further analysis.

2.7.2. FLOW CYTOMETRY ANALYSIS

Flow cytometry data was collected in a BD FACSCalibur™ (BD Biosciences) and data analysis was done using FlowJo v10.1 software. Cells were incubated with Stv-BiotON-PNATet1 (1:1:5) at 0.025 µM for 1 hour at 37˚C. Cells were then trypsinized, washed once with PBS, re-suspended in cold PBS and filtered for analysis.

2.7.3. IMAGE STREAM ANALYSIS

Image stream data was collected using an Amnis ImageStream® (Merck Millipore). Cells were incubated with fluorescently labeled TDN-PNATet1 (1:5) 0.025 uM for 1 hour at 37˚C. After that, cells were trypsinized, washed once with PBS, re-suspended in cold PBS and filtered for analysis. Image acquisition was done twice for each sample, in order to acquire images in the open mode (for internalization analysis) and in the EDF (extended depth field) mode (for spot count analysis).

Data analysis was performed using the IDEAS® v6.2 software (Merck Millipore), making use of masks in order to discriminate between cell membrane and cytoplasm for the internalization analysis, as well as the spot mask for the spot counting analysis.

2.8. STATISTICAL ANALYSIS

Data is graphically presented in the form of mean ± standard deviation (SD), from results obtained from three independent experiments, unless otherwise stated. Significance was assessed by repeated measures matched one-way ANOVA, in GraphPad Prism7. No significance was assumed for $p > 0.05$, and significance was assumed for: * $p < 0.05$; ** $p < 0.01$; *** $p < 0.001$; **** $p < 0.0001$.

Chapter 3

Results and Discussion

- 3.1. Protocol optimization using previously studied TDN sequences
  - 3.1.1. TDN1 assembly by the Multistrand approach: annealing of four DNA strands pre-designed to hybridize into a tetrahedron
  - 3.1.2. TDN1 extraction and purification from polyacrylamide gels
- 3.2. Assembly and characterization of newly designed TDN2 sequences
  - 3.2.1. Design of a novel DNA tetrahedron
  - 3.2.2. PAGE analysis of TDN2
  - 3.2.3. DLS analysis of TDN2
  - 3.2.4. AFM analysis of TDN2
  - 3.2.5. Initial assessment of the novel TDN2 cellular uptake
- 3.3. Development and characterization of the cellular model for uptake studies
- 3.4. assessment of the PNA-Tet1 efficiency by conjugation with Streptavidin-Biotin system
- 3.5. TDN neuronal targeting by Tet1 peptide
  - 3.5.1. PAGE characterization of the TDN-Tet1 system
  - 3.5.2. *In vitro* uptake studies of TDN-Tet1

3.1. PROTOCOL OPTIMIZATION USING PREVIOUSLY STUDIED TDN SEQUENCES

Initially, annealing and purification protocols were tested and optimized using previously described and studied TDN sequences (Greene et al., 2012).

3.1.1. TDN1 ASSEMBLY BY THE MULTISTRAND APPROACH: ANNEALING OF FOUR DNA STRANDS PRE-DESIGNED TO HYBRIDIZE INTO A TETRAHEDRON

At first, the stepwise assembly of the DNA-tetrahedron (TDN1), by annealing equimolar quantities of different combinations of TDN1 sequences, was analyzed by PAGE **(Fig. 12)**. This enabled the correct identification of the TDN1 band at around 250 bp in the last lane, when comparing with the DNA ruler.

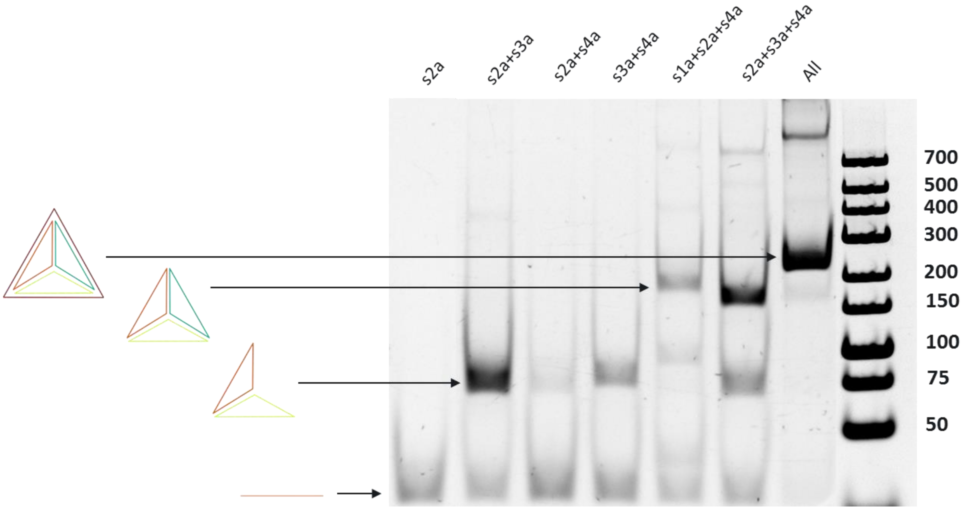

Figure 12 PAGE analysis of the step-by-step assembly of the TDN with the representation of one, two, three or all four sequences in the gel. On the left of the gel, schematic representations of presumed formed structures are presented. The right most lane shows the GeneRuler DNA ladder and corresponding base pair (bp) numbers.

In order to optimize and achieve the highest yields of correctly assembled structure (minimizing improperly folded structures of high molecular weight, or incomplete assemblies of lower molecular weight), different annealing conditions were tested. Two annealing protocols that differ in the duration of the annealing (FAST – 30 s and SLOW – 2 hours 30 min) and three different annealing buffers (TM 5 mM Mg^{2+}, TM 12.5 mM Mg^{2+} and PBS 2x) in a range of final strands concentrations (0.05 – 3 µM) were compared **(Fig. 13** and **14)**. Image analysis using Fiji allowed for the calculation of the percentage of the TDN1 band in the whole lane (taking into account other bands present and the correction according to the size of the structures formed).

The FAST annealing protocol revealed to be the one yielding a higher amount of the desired structures at highest concentrations tested, thus being chosen for further assemblies. As to the annealing buffers, both Tris-Magnesium buffers allowed for high percentages of the TDN1 to be formed at 1 µM, of around 70% of the sample being the preferred structure. Since there was no apparent difference, the buffer considered for following assemblies was the one presenting the lower concentration of Mg^{2+}, not to interfere with cell homeostasis in later studies. Electrophoresis analysis exhibited one prominent band for each combination of strands, as predicted, and in accordance to published results (Greene et al., 2012; Xia et al., 2016), suggesting that desired nanostructures had successfully assembled **(Fig. 14)**.

By testing different strand concentrations we wanted to analyze the contribution of the inter- and intramolecular interactions for the tetrahedron assembly, in different buffer and annealing temperature conditions. At low strand concentrations higher intramolecular interactions are to be expected, on the contrary at high strand concentration a competition between intra and intermolecular interactions starts to occur. A high number of intermolecular interactions will thus result in the appearance of improperly assembled high molecular weight structures, as can be seen by the appearance of bands with > 700 bp mass in **Fig. 14**.

Aiming at obtaining greater quantities of the desired structure per assembly, the highest concentration that does not compromise the structure yield is the ideal one. From the obtained results, one can assume that the FAST protocol benefits intramolecular interactions better than the SLOW protocol, and structures assembled by the FAST protocol in a final concentration of 1 µM allow for a relatively high quantity of the structure to be obtained with a positive commitment regarding intermolecular interactions.

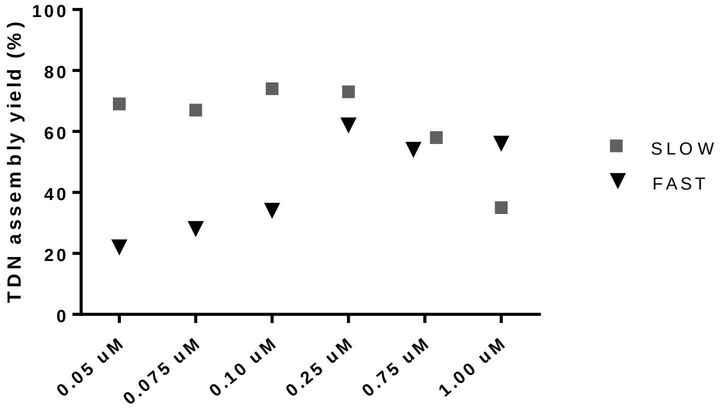

Figure 13 Percentage of TDN in each sample according to the annealing protocol: 2 h 30 min (SLOW) or 30 s (FAST), comparing a range of different final strands concentrations in TM buffer (5mM Mg^{2+}). Data results from one experiment.

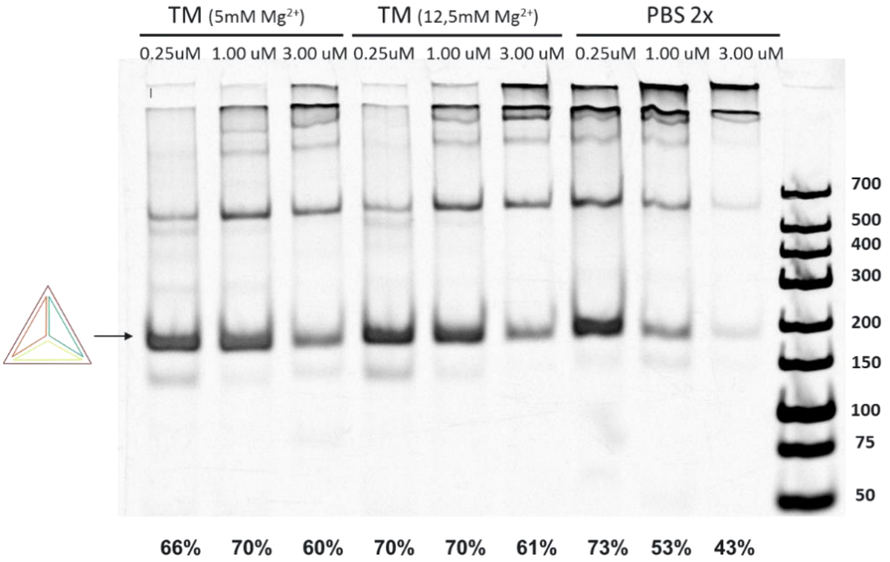

Figure 14 PAGE analysis of annealed strands comparing three different buffers and three different final strands concentrations. Displayed percentages on the bottom indicate the percentage of TDN in each lane. Note: this gel was run in TBE 1x, and not in TBE 1x 12.5 mM $MgAc_2$, which explains the different migration of the bands and the localization of the TDN1 band at around 200 bp instead of 250 bp as previously indicated. The tetrahedron band is schematically indicated to the left of the gel.

3.1.2. TDN1 EXTRACTION AND PURIFICATION FROM POLYACRYLAMIDE GELS

Although, after optimization of conditions, a high percentage of correctly assembled tetrahedron was achieved (70 %) purification of this structure is preferable, in order to proceed with additional characterizations and experiments using only the pure TDN. For this, assembled structures were run in a polyacrylamide gel and detected by the dye-free UV shadowing technique, in order not to contaminate the sample with DNA intercalating dyes. Subsequently, the corresponding band was excised and further purified, using two different methods: the Spin-X and the Crush&Soak. Briefly, these two methods mainly differ on the time of sample processing and the sample incubation with a soaking solution: the Spin-X protocol consists of cutting the gel band into pieces, freezing it, adding TM buffer and collecting by centrifugation through a tube filter; the Crush&Soak protocol consists of shredding the gel band into pieces, incubating it in soaking solution (3 times the volume of the gel) at 4˚C for 24 h, and then centrifuging it for collection.

Analysis by PAGE of the TDN recovery with both methods **(Fig. 15)** revealed the Crush&Soak method as the one allowing the highest recovery of the DNA structure, possibly due to enabling a more efficient diffusion of the structure from the gel pieces into the soaking solution for 24 h. Although it was expected that the incubation with the soaking solution in the Crush&Soak protocol would increase the recovery rates of the structure, the Spin-X method was tested since it would benefit from shorter processing times and lower sample dilutions.

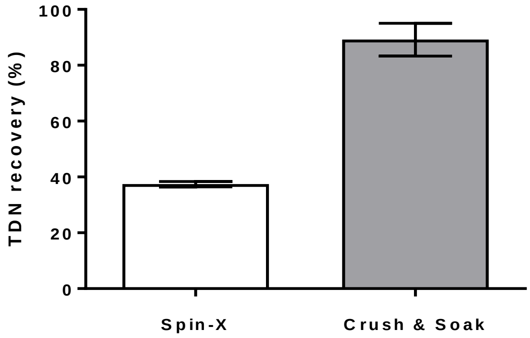

Figure 15 Tetrahedron recovery after purification by the Spin-X and the Crush&Soak methods.

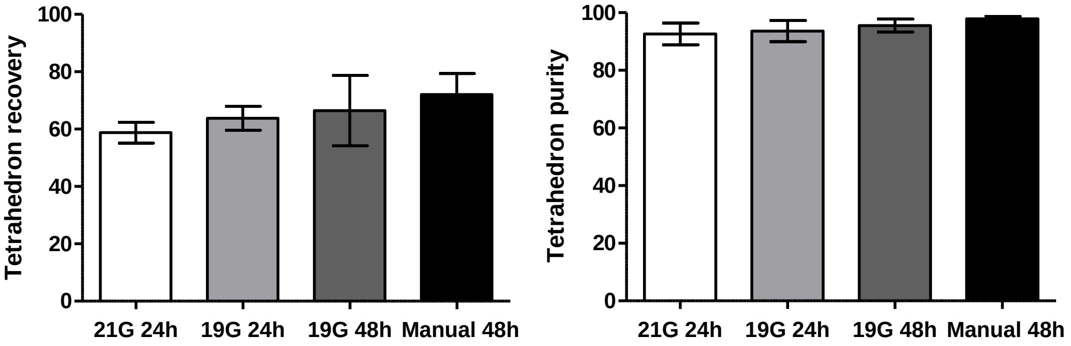

Figure 16 TDN recovery (left) and purity (right) after purification following altered Crush&Soak protocols as analyzed by PAGE.

Further alterations to the protocol were done in order to maximize recovery and maintenance of the structure integrity. Four protocols were tested: shredding the gel through a 21 G or 19 G needle hole with 24 hours of soaking at 4˚C (21 G 24 h and 19 G 24 h, respectively) and shredding the gel through a 19 G needle hole or through manual cutting with 48 hours of soaking (19 G 48 h and Manual 48 h, respectively). PAGE analysis and comparison of the calculated percentages of recovery and purity (relative quantity of tetrahedron structure in the solution, taking into account other non-desired structures that might have formed during the purification process) **(Fig. 16)**, indicated the Manual crush with 48 h of soaking as the protocol with a small tendency for the highest recovery rate and purity of processed samples, being this the protocol followed in further purifications.

After analyzing the obtained samples by UV spectrophotometry, a peak at around 230 nm indicated the presence of contaminants after the purification protocol, which were attributed to EDTA and Mg^{2+} ions (Appendix A). A desalting step was, thus, added to the purification protocol, by using Amicon centrifugal devices according to manufacturer's instructions. Comparing the UV spectra of a purified TDN1 sample before and after the desalting step, it is possible to observe the decrease of the ratio of contaminant (<240 nm):DNA (260 nm), as desired.

Triplicate samples obtained by aforementioned purification protocols were analyzed regarding the stability of the TDN1 at 4˚C for 4 weeks **(Table 2)**.

Table 2 Stability of the purified TDN1 for 4 weeks at 4˚C, as indicated by the purity of the samples run in polyacrylamide gels (hyphens mark samples which were not analyzed on the indicated time-point due to sample loss; t=0 samples were analyzed immediately after purification).

	21G 24 h	19G 24 h	19G 48 h	Manual 48 h
t= 0	92,6%	95,2%	95,9%	96,4%
t= 1 week	97,4%	98,3%	99,2%	99,5%
t= 2 weeks	96,6%	98,2%	99,0%	98,9%
t= 3 weeks	96,6%	98,5%	99,4%	99,3%
t= 4 weeks	95,7%	98,0%	99,1%	98,9%
t= 0	86,2%	86,6%	91,5%	98,3%
t= 1 week	86,6%	86,9%	92,1%	98,2%
t= 2 weeks	90,1%	90,0%	93,6%	98,7%
t= 3 weeks	90,0%	89,9%	93,5%	98,6%
t= 4 weeks	90,4%	90,2%	93,7%	98,5%
t= 0	99,1%	99,1%	99,3%	99,0%
t= 1 week	99,7%	99,7%	99,7%	99,6%
t= 2 weeks	99,2%	99,0%	99,1%	99,0%
t= 3 weeks	98,7%	98,5%	98,6%	98,5%
t= 4 weeks	99,1%	-	99,0%	-

Results revealed that purified TDN1 maintained its structure, with virtually no degradation or structure rearrangement, since the percentage of the TDN in the sample did not show appreciable variations with time (as analyzed by PAGE).

3.2. ASSEMBLY AND CHARACTERIZATION OF NEWLY DESIGNED TDN2 SEQUENCES

3.2.1. DESIGN OF A NOVEL DNA TETRAHEDRON

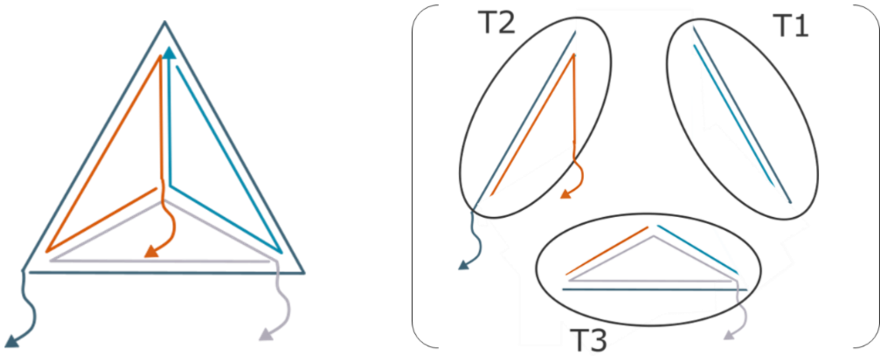

Figure 17 Representation of the novel TDN design, wavy lines representing the unhybridized anchor sequences, which have the same pre-defined sequence (as determined for high affinity binding to a 15-mer PNA sequence) and arrows representing the 3' ends of the sequences (left). Segmentation of the tetrahedron design into 3 regions (T1, T2 and T3) without pseudoknots for NUPACK analysis and sequence design (right).

a

Normalized ensemble defect: 3.1 %

S4_3: ACAGGTCGGAGGTCGTAACCG
S4_2: ACGGCCGCGCTCCCTGGTAGG
S4_1: GGTGACCGGCCGTCGGACGC
S3_2: AGCACAAATTTCGTTAAGGGTACGGTTACGACCTCCGACCTGCAATAATGACTAAAAGCG
S3_1: GTGACGACTCGCCTAGTCAG
S2: CCTCATCCCTCCGTAAGTGCACTGACTAGGCGAGTCGTCACACCTACCAGGGAGCGCGGCCGCAATAATGACTAAAAGCG
S1_3: AACCCTTAACGAAATTTGTGCCAATAATGACTAAAAGCG
S1_2: AGCGTCCGACGGCCGGTCACC
S1_1: GCACTTACGGAGGGATGAGG

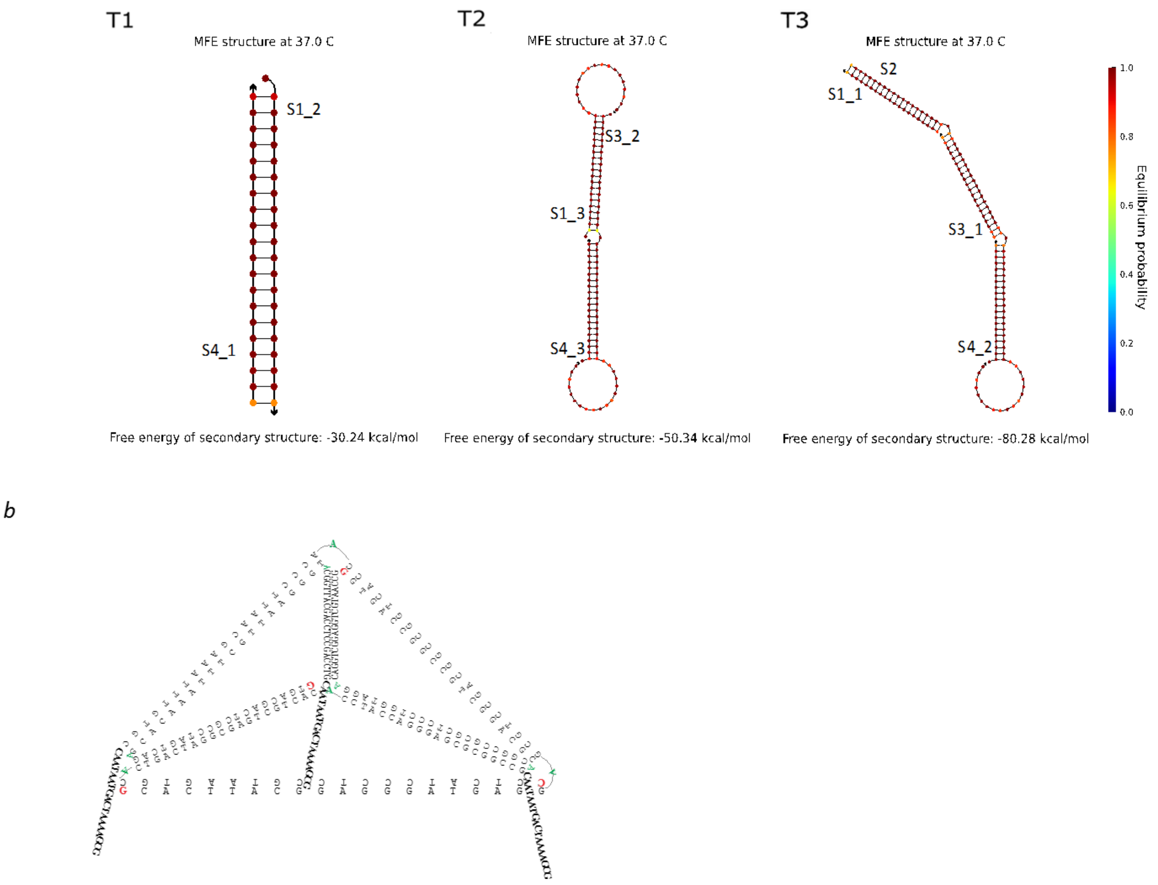

Figure 18 (a) NUPACK generated sequences from a maximum probability of defects of 3.1 % (top). Minimum free-energy structures of the resultant sequences for the 3 segmented regions of the TDN. (b) Output sequences representation in a tetrahedral structure. Green bases are unpaired, red bases represent the 5' ends of sequences.

Novel TDN sequences were designed and studied for the assembly of a new tetrahedral structure bearing three “anchors” for annealing with a neuron-targeting peptide-nucleic acid conjugate. Sequences were designed using the NUPACK web server (Zadeh et al., 2011), and further *in silico* analyzed in order to minimize secondary structures and unwanted interactions, as well as optimize stability. As the NUPACK algorithms do not allow the prediction of sequences based on pseudoknots (DNA/RNA structures minimally composed of two helical segments connected by single-stranded regions or loops) the TDN design was segmented into 3 regions **(Fig. 17)**. The 3 regions and resultant structures were then defined in “DU+” or “dot-parens-plus” notation according to NUPACK coding language (Appendix B). Specific sequences (CCCC, GGGG, CCCCC, GGGGG) were excluded from the possible design since these are known to produce undesired secondary structures. A set of sequences was then obtained theoretically, producing the target structures in equilibrium with a 3.1 % probability of defects at 37˚C and for a concentration of 1 µM of strands **(Fig. 18)**. The loop resembling portions in the generated sequences representation **(Fig. 18a)** correspond to the anchor sequences that are confirmed to be successfully unhybridized in the output designs (for display purposes, NUPACK assigns a loop representation to unpaired bases) and thus available for further conjugations. The final complete sequence of each of the 4 strands composing the TDN was then put together by simply following the correct 5’ to 3’ directions **(Fig. 18b)**.

3.2.2. PAGE ANALYSIS OF TDN2

First, a step-by-step assembly of TDN2 was analyzed by PAGE, by combining different strands in a final concentration of 0.1 µM **(Fig. 19)**. An expected ladder-type migration pattern, as well as one clearly prominent band for each combination of strands was obtained. As can be noted, s4b strand is slightly lighter and migrated farther, which is due to the lack of the extra 18-nucleotide “anchor” present in the other three strands (s1b, s2b and s3b). The TDN2 band is identified at around 350 bp, when comparing with the DNA ruler.

In order to confirm that the optimal annealing conditions obtained with TDN1 are, as well, the optimal conditions for the assembly of TDN2, different final concentrations and annealing buffers were tested with the FAST annealing protocol **(Fig. 20)**. Optimal assembly conditions of TDN2 coincide with the ones obtained for TDN1, achieving a TDN2 yield of 76 %

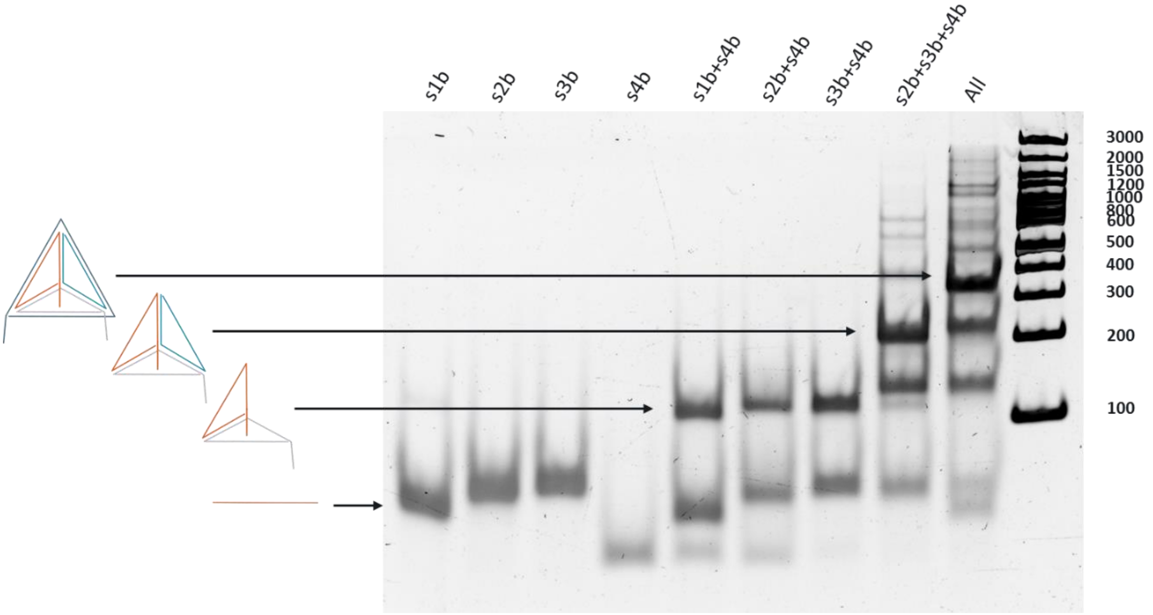

Figure 19 Stepwise assembly of novel TDN2 sequences by combining equimolar quantities of combinations of strands. On the left of the gel, schematic representations of the presumed structures are presented.

when following the fast annealing protocol with TM buffer at a final strand concentration of 1 µM.

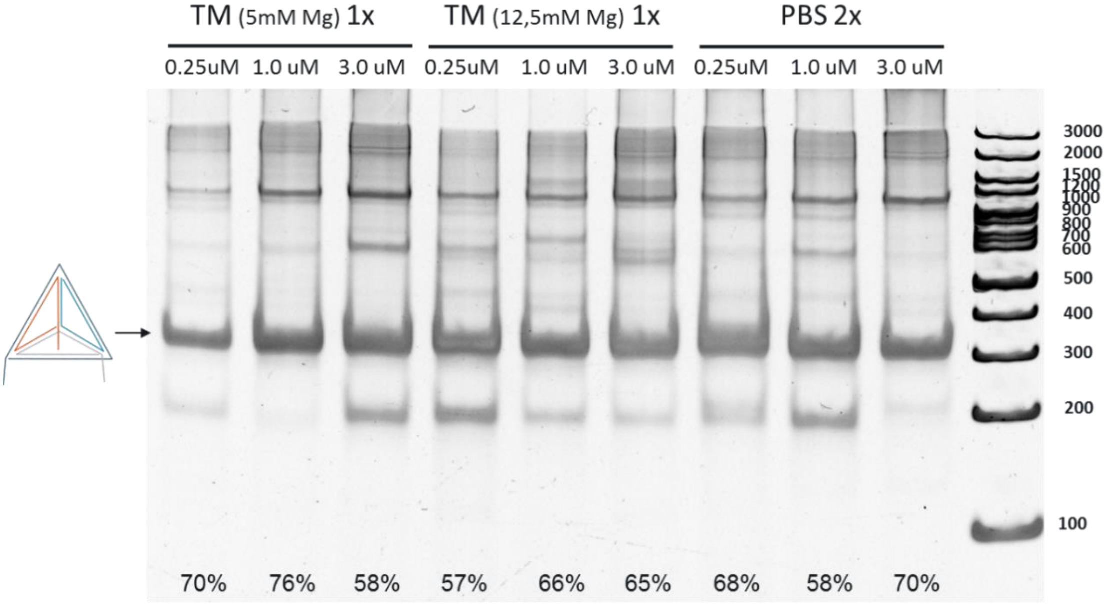

Figure 20 PAGE analysis of annealed strands comparing three different buffers and final strands concentrations. Indicated percentages specify the percentage of TDN2 in each lane. The tetrahedron band is schematically indicated to the left of the gel.

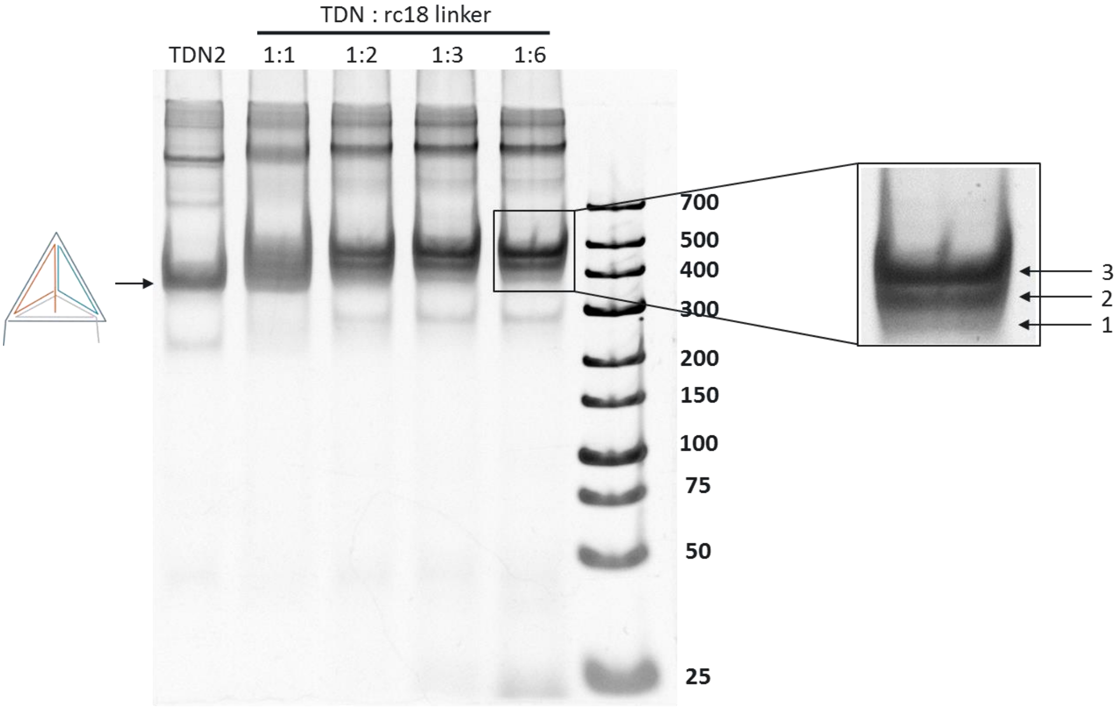

Figure 21 PAGE analysis of the hybridization of the TDN2 anchors with a complementary DNA strand (rc18) at different ratios. The tetrahedron band is schematically indicated to the left of the gel. Inset: bands corresponding to 1, 2 and 3 hybridized linker DNAs - bottom to top, respectively - are highlighted.

For the purpose of confirming that the three ssDNA “anchors” are correctly exposed, varying ratios of a complementary DNA linker strand (rc18) were added to the assembled unpurified TDN2. Analysis by PAGE **(Fig. 21)** revealed a shift of the TDN2 band with increasing ratios of the DNA linker strand. Specifically, three bands of very close mass are observed resulting from the annealing of one, two or all three anchors of the TDN2 to the DNA linker. The 1:3 ratio should allow the annealing of all three TDN anchors with the DNA linker, however the detection of these mentioned three structures does not suggest that. The same occurs in the 1:6 ratio, presenting an excess of the complementary DNA strand. This could be a result from unpredicted steric constraints as the anchor sequences are immediately flanking a highly structured region (the vertices of the tetrahedron). In such a case this could suggest that spacing the anchors with, for example, a single unpaired nucleotide (e.g. one T) could provide sufficient flexibility avoiding the steric constraints. Alternatively, as the samples analyzed were not purified, the existence of unassembled or irregular structures could expose regions with partial complementarity to the linker DNA competing for the correct hybridization with the anchor sequences. Nevertheless, the most prominent band in the lane of both samples is the third higher mass structure **(Fig. 21** inset**)**, showing a high level of complete assembly of the TDN anchors with the complementary DNA linker strands.

3.2.3. DLS ANALYSIS OF TDN2

Dynamic light scattering size analysis of this structure revealed a range of apparent hydrodynamic diameters between 13,25 nm and 14,67 nm. A representative graphic of the TDN2 size distribution, according to the intensity of scattered light, is depicted in **Fig. 22**.

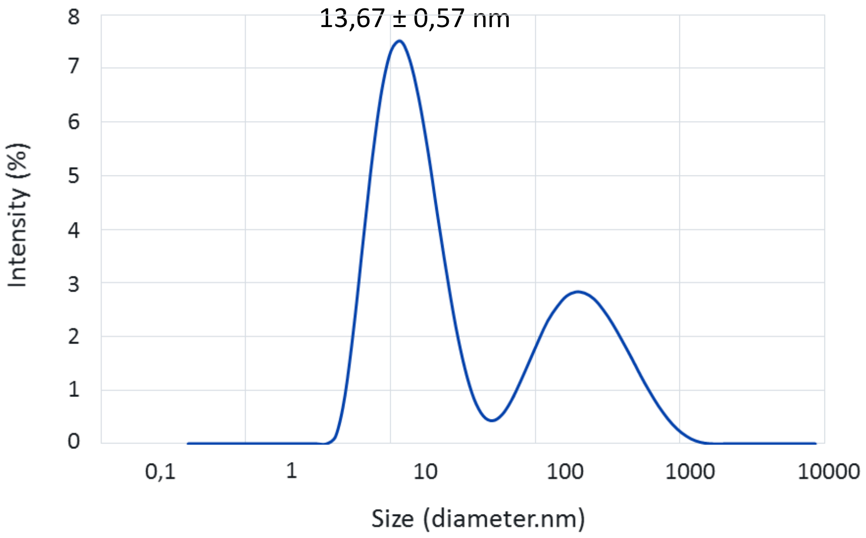

Figure 22 TDN2 size distribution by intensity of scattered light. Mean hydrodynamic diameter as wells as the standard deviation are indicated above the graph.

Table 3 Percentages of number and volume occupied by the 1^{st} peak, and PDI values obtained for each measurement.

	Size by Number	Size by Volume	PDI
Sample 1	100%	99,9%	0,61
Sample 2	100%	100%	0,33
Sample 3	100%	100%	0,60

DLS analysis of the TDN2 allowed the measurement of the apparent hydrodynamic diameter, with good quality cumulant/correlogram fit (good quality measurements) only at high sample concentrations (around 2 µM). The first and highest indicated peak shows a mean hydrodynamic diameter of 13,67 ± 0,57 nm, resultant from 3 independent measurements at similar concentration values. These values are consistent with the expected hydrodynamic diameter of the TDN, falling in the range of observed diameter values for different described TDNs (Keum, Ahn, & Bermudez, 2011; K.-R. Kim et al., 2013; Lee et al., 2012; X. Li et al., 2012). For instance, recently, Jiang and co-workers revealed an hydrodynamic diameter of about 13 nm for a TDN of 20bp of side length (Jiang et al., 2016), a value very close to the one here obtained and discussed.

The second peak, at around 265 nm, can be explained by the Rayleighs approximation, which states that the intensity of scattered light is proportional to the diameter of the particles to the 6th power. Translating this theory, a 100 nm particle will scatter 10^6 as much light as a 10 nm particle. Since after purification a very small percentage of higher order structures are still present in the sample (identified by PAGE analysis, results not shown), these can be influencing the DLS analysis. In such case, when a second peak appears, one should take into account the information given in the size distributions by volume and by number **(Table 3)**. In fact, in all measurements, the percentage of number and volume of the sample occupied by the 1st indicated peak is very close or equal to 100%. Polydispersity index values (PDI) showed a relatively high number (>0,3), however as PDI calculations only take into account the intensity values, the detection of structures with higher hydrodynamic diameters impedes the calculation of a true PDI value for the correct TDN.

3.2.4. AFM ANALYSIS OF TDN2

More direct evidence for the self-assembly into a tetrahedron was provided by AFM imaging in liquid. Performing the analysis in a liquid environment allowed the maintenance of the structural features of the TDN2, and in fact an approximately pyramidal structure was observed, with three resolved edges and a triangular-shaped base **(Fig. 23)**. Imaged structures presented height dimensions between 4,5 and 5 nm, which are very close to expected theoretical values of around 5 nm. These were calculated using the formula below, taking into account the side length, given by the known length of a base pair – 0,332 nm – and the number of base pairs present at each side of the TDN – 20bp. Additionally, the measurements are consistent with published values for a TDN of similar dimensions (Leitner et al., 2011). Regarding the edge width, the obtained value was around 13 nm, contrasting with the theoretically estimated 7 nm length. This can be explained by the fact that the AFM tip used, with a 20 nm diameter, did not present enough lateral resolution for an accurate measurement. In addition, the theoretical length calculations (based on perfect geometrical figures) do not take into account contributions from the width of a dsDNA helix - 2 nm.

$$h = \sqrt{\frac{2}{3}} \times a \text{ , } a \text{ being the side lenght}$$

$$h = \sqrt{\frac{2}{3}} \times 0{,}332 \, nm \times 20 \, bp \; = 5{,}4 \, nm$$

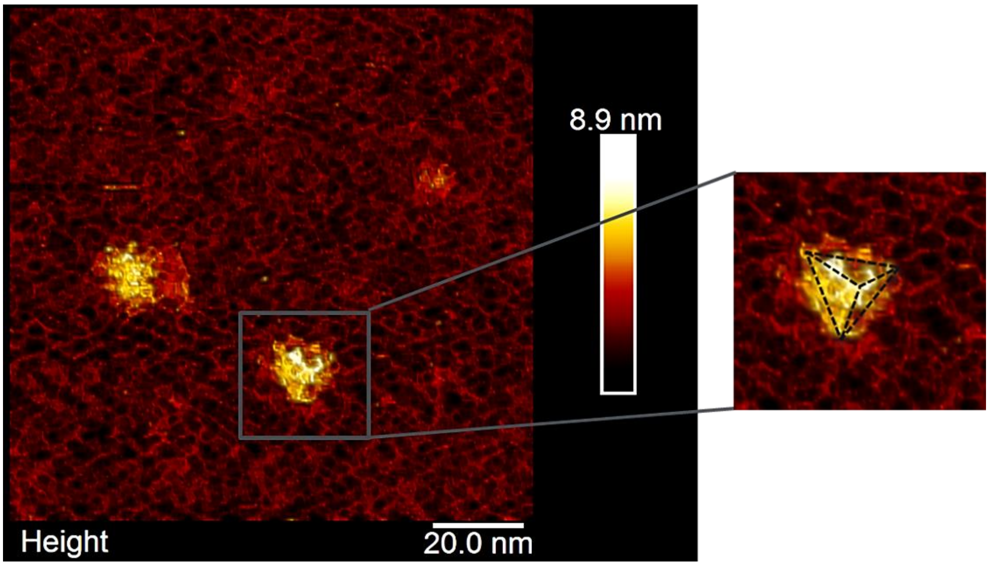

Figure 23 AFM liquid analysis of TDN2. Inset: proposed scheme of the resolved structure, highlighting what resembles three upper edges and the triangular base of the tetrahedron.

3.2.5. INITIAL ASSESSMENT OF THE NOVEL TDN2 CELLULAR UPTAKE

A preliminary analysis of the cellular internalization of TDN2 was done by assessing the uptake of these FAM-labeled nanostructures by Image Stream Cytometry. ND7/23 cells were incubated with labeled TDN2 for 1 hour at 37˚C, after which the cells were analyzed **(Fig. 24)**.

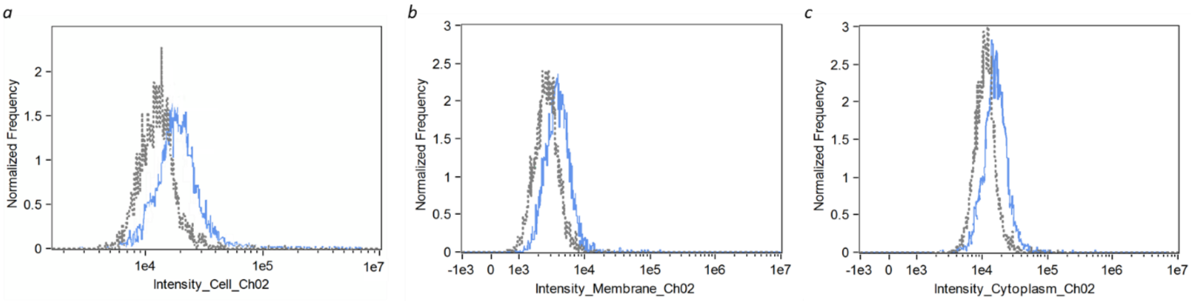

Sample	Median Intensity
CTR	12573,63
TDN2	18190,72

Sample	Median Intensity
CTR	2591,31
TDN2	3806,44

Sample	Median Intensity
CTR	11109,00
TDN2	16141,51

Figure 24 Image Stream Cytometry analysis of the cellular uptake of untreated ND7/23 cells (CTR – pointed grey graph) and cells incubated with FAM-labeled TDN2 (TDN2 – blue graph). Cellular uptake was assessed according to the fluorescence intensity in (a) the whole cell, (b) cellular membrane and (c) cytoplasm. Median intensity values of each analyzed sample are indicated in the table below each graphic. Data from (b) and (c) were obtained through the use of membrane and cytoplasm masks for the analysis of the fluorescence intensity.

A small shift to higher fluorescence intensities after TDN2 incubation was observed, suggesting an association of the TDN2 with cells. Roughly the same shift was seen when analyzing for only membrane- or cytoplasm-associated fluorescence, possibly indicating that in these conditions TDN structures are both interacting with the membrane and some already internalized. These results are in line with previous reports, showing cell uptake of DNA nanostructures (Hamblin et al., 2012; Walsh et al., 2011), although with this particular neuroblastoma cell line TDN2 (from this point on, TDN2 will be simply referred to as TDN) uptake seems relatively modest.

3.3. DEVELOPMENT AND CHARACTERIZATION OF THE CELLULAR MODEL FOR UPTAKE STUDIES

With the aim of studying specific cellular uptake by neurons, a cellular model was developed by differentiating ND7/23 cells. The ND7/23 cell line, derived from the fusion of neonatal rat sensory neurons with mouse neuroblastoma, displays sensory neurons features, and the differentiation of these cells induces the development of neurite-like projections as well as a more approximate behavior to that of *in situ* neurons (Suburo et al., 1992; Wood et al., 1990). In order to accomplish this, cells were differentiated for 6/7 days in laminin-coated surfaces, using two different differentiation media: one containing low FBS (0.5%) and another serum-free containing b27 supplement (2%), both in DMEM F12 supplemented with NGF, dbcAMP and antibiotics, according to published literature (Wood et al., 1990). Laminin was used for cell adhesion purposes and neurite-like outgrowth during the course of differentiation (Powell et al., 2000). Poly-D-lysine is also a standard substrate used to culture neuronal cells, however it was not a suitable coating for the experiments here conducted. Due to its positive net charge, the polymer would electrostatically interact with DNA nanostructures during uptake studies (Kam, Shain, Turner, & Bizios, 2001).

Undifferentiated and differentiated ND7/23 cells were stained for the heavy subunit of neurofilament (NF-H) **(Fig. 25)**, a major component of neuronal cytoskeleton particularly abundant in axons and dendrites (Yuan, Rao, Veeranna, & Nixon, 2012), in order to confirm the formation of neurite-like projections. Both media induced an apparent increase in the expression of the NF-H protein, when comparing with cells cultured with regular growth medium (DMEM + 10% FBS), as assessed by immunohistochemistry. The expression of this cytoskeleton protein, highly abundant in axons and dendrites, revealed the formation of neurite-like extensions in treated cells, as expected, indicative of the differentiation of ND7/23 cells.

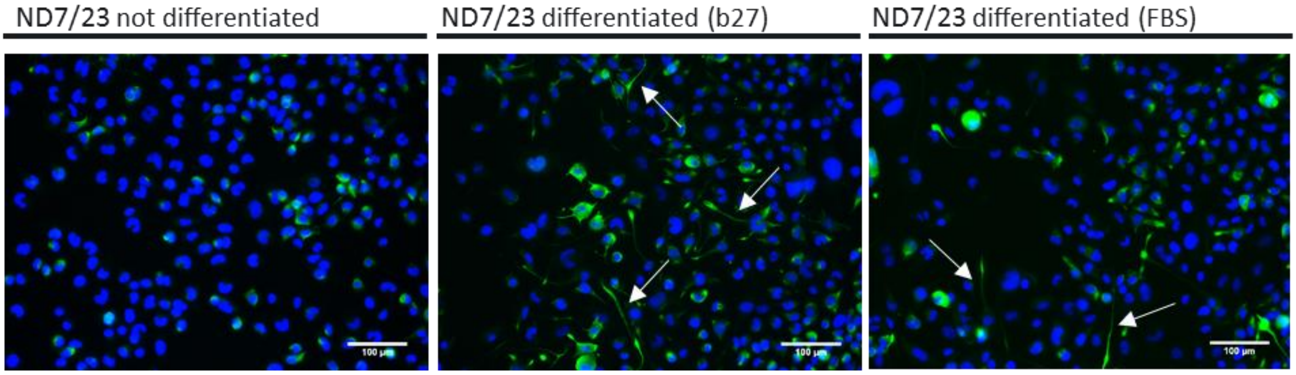

Figure 25 Representative images of NF-H (green) expression in differentiated and not differentiated ND7/23 cells. Nuclei are stained with Hoechst 33342 (blue). White arrows indicate neurite-like extensions formed by differentiated cells. Scale bars: 100µm.

Next, we wanted to evaluate the cell surface expression of the ganglioside receptor Gt1b in undifferentiated and differentiated cells. The expression of this receptor is of particular relevance as it is the receptor interacting with the neuron-targeting peptide Tet1, which could then enable neuron targeted TDN delivery.

Analysis by FACS revealed that differentiated ND7/23 cells present an increased expression level of the ganglioside GT1b **(Fig. 26)**, which had not previously been described in the literature. This result suggests that differentiated ND7/23 cells are more closely resembling sensory neurons potentially avoiding the increased unspecific uptake characteristic of fast-growing tumor cell lines. Hence, differentiated ND7/23 appeared to be a suitable cellular model for uptake studies. Furthermore, as higher levels of the receptor are expressed at the surface this could have a positive influence on specific uptake activity.

A tendency for a higher relative level of expression of the ganglioside is observed in cells differentiated with the serum-free b27 supplemented medium, in comparison to cells differentiated with the low FBS containing medium. Of notice is also the fact that, after differentiation, the cell population expressing the Gt1b is much more homogeneous than undifferentiated cells, which present a relatively high number of cells with very low or absent Gt1b expression (comparing to the unstained sample). Hence, this cell model (differentiated ND7/23) was advantageous for proceeding with initial uptake studies, as it could recapitulate, to some extent, the features of primary neuronal cells. It is important to highlight that differentiated cells are normally non-dividing cells which, contrary to fast growing tumor cell lines, present lower levels of unspecific endocytic activity (Levine, Hoang, & Raines, 2013; Ortega et al., 2015). This is a relevant feature to take into account when studying uptake by neuronal cells.

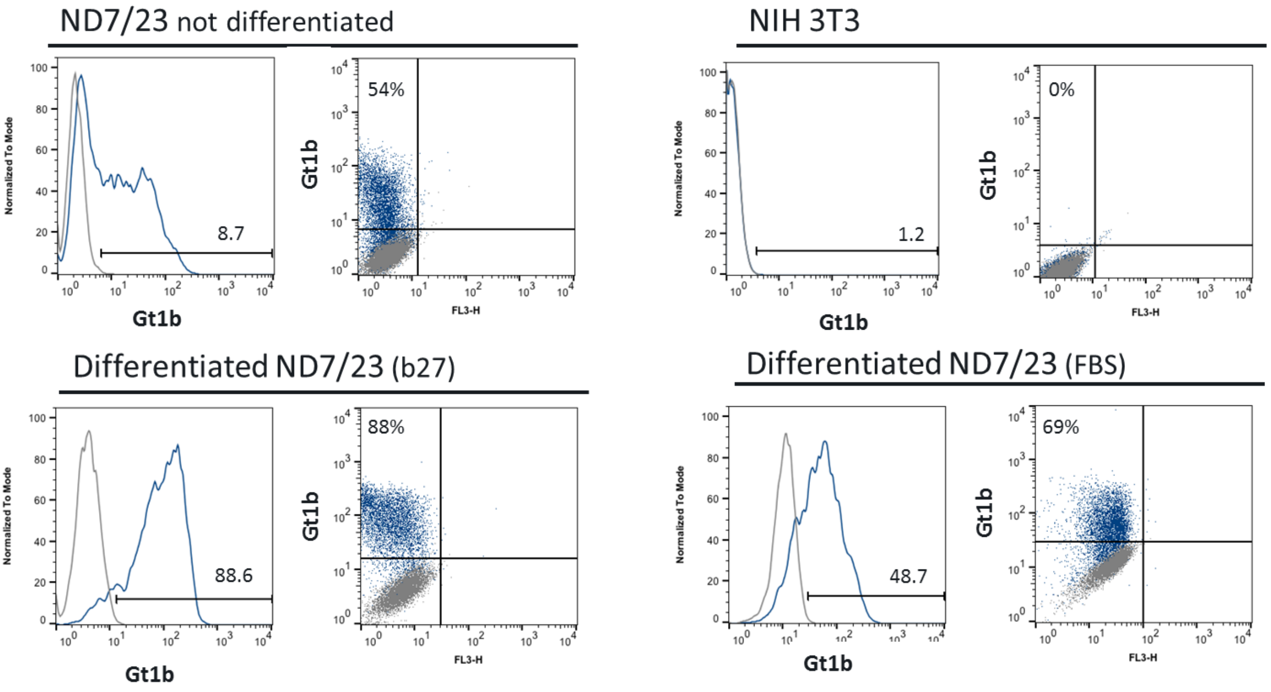

Figure 26 FACS analysis of Gt1b expression in differentiated and not differentiated ND7/23 cells and in NIH 3T3 cells, as a negative control. Represented in grey is the unstained sample. The blue colored data corresponds to the anti-Gt1b stained sample. Median Gt1b intensity values of stained samples are indicated on histograms. Displayed percentages on dot plots indicate the frequency of the Gt1b positive cells in the population.

3.4. ASSESSMENT OF THE PNA-TET1 EFFICIENCY BY CONJUGATION WITH STREPTAVIDIN-BIOTIN SYSTEM

Tet1 (of sequence HLNILSTLWKYR), a synthetic peptide with binding affinity and retrograde transport analogous to that of the well-established neuron-targeting TeNT Hc fragment, was chosen as a targeting moiety, given the already specified characteristics and the additional advantage of not presenting associated immunogenicity (J. K. Liu et al., 2005). The adopted strategy to conjugate the Tet1 peptide to the DNA-based structure lied on the use of PNA as a "bridging molecule" between the targeting peptide and the TDN single stranded anchors. PNA, a synthetic nucleic-acid oligomer, presents high binding affinity to DNA molecules due to its uncharged nature. This allows a strong interaction even in short PNA-DNA duplexes, given the inexistent electrostatic repulsion that occurs in DNA-DNA duplexes.

Additionally, PNA and peptides have compatible synthesis methods, and thereof conjugates can be easily obtained by a single continuous automated peptide synthesis protocol. The PNA-Tet1 conjugate is easily integrated into the novel TDN by annealing between the ssPNA and the ssDNA anchors present in the structure.

With the purpose of firstly evaluating the performance of the PNA-Tet1 conjugate, a simple system associating the conjugate with Biotin and Streptavidin was designed: PNA-Tet1 was hybridized to a Biotin-conjugated oligonucleotide sequence complementary to the PNA sequence, which was then conjugated to fluorescently labeled Alexa488-Streptavidin. A control system with a complementary ssDNA linker hybridezed to the Biot-ON instead of the PNA-Tet1 conjugate (referred to as StvBiot-rcON) was also constructed **(Fig. 27).**

Figure 27 Schematic representation of the StvBiot-Tet1 (left) system and corresponding control StvBiot-rcON (right).

PAGE analysis of different molecular ratios between each moiety allowed optimization of the complete assembly.

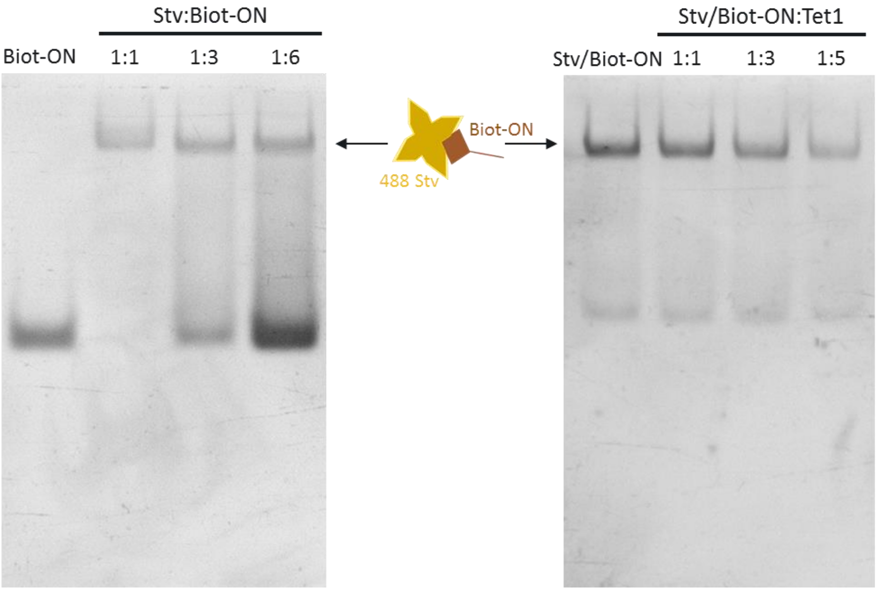

Figure 28 PAGE analysis of the optimal ratio for the conjugation of (left) Streptavidin/Biotin-ON and (right) Streptavidin/Biotin-ON-Tet1. The Stv/Biot-ON band is indicated.

On **Fig. 28** left, 1:1 of Streptavidin:Biotin-ON (Stv:Biot-ON) seems to be the best ratio, consuming all the Biot-ON and yielding the Stv/Biot-ON system, while higher ratios indicated an excess of Biot-ON noticeable from the increase of this band.

On the right panel of **Fig. 28**, although no higher mass complex can be detected in the gel, the increasing depletion of the Stv/Biot-ON band as the molecular proportion of ligand increases, suggests that the complex is being formed to some extent. The expected proportion of Tet1 relative to Biot-ON would be 1:1, however PAGE analysis did not reveal that. We believe this can possibly be a result from the low hydrophilicity of the PNA-Tet1 conjugate, which could tend to aggregate in solution and become unavailable for hybridization. In fact, spectrophotometric readings of the PNA-Tet1 conjugate concentration in solution (OD readings at 260 nm) revealed consistently lower values than expected ones (results not shown), indicating the possibility of the conjugates not to be completely solubilized. This can be a result from the uncharged nature of the PNA molecule and the aminoacid composition of the Tet1 peptide, presenting only 3 positive aminoacids (polar), opposite to 3 uncharged and 6 hydrophobic aminoacids.

In line with the aforementioned, only at higher PNA-Tet1 ratios did the Stv/Biot-ON band start to disappear in the lane, suggesting a need for an excess of the PNA-Tet1 conjugate in order to obtain the desired structure.

It should be mentioned that a 5 fold excess of PNA-Tet1 conjugate is not optimal, since free (or aggregates of) PNA-Tet1 molecules could be present during *in vitro* cell uptake studies, interfering to some extent with the studies. Thus, a future redesign of the PNA-Tet1 conjugate sequence would be advantageous (e.g. including solubility enhancer linkers between the PNA and peptide moieties or reducing the purine content of the PNA sequence).

The Stv/Biot-ON-PNA-Tet1 (from here on referred to as StvBiot-Tet1) system, allowed us to have an initial simpler construct to test the Tet1 targeting ability when linked through a PNA-DNA hybrid.

For assessing cell binding/uptake, both Stv systems (with PNA-Tet1 or control) were incubated with undifferentiated ND7/23 cells for 4 hours at 37˚C, after which cells were fixed and stained with an anti-Gt1b antibody, and analyzed by confocal microscopy **(Fig. 29)**.

Images revealed that cells associated to a lesser extent with the control system, not bearing the targeting peptide **(Fig. 29a)**, when comparing with cells treated with the StvBiot-Tet1 system **(Fig. 29b)**, which presented a higher intensity as well as frequency of fluorescence signals. Image analysis confirmed the presence of the StvBiot-Tet1 system inside cells and in very close proximity to Gt1b receptors **(Fig. 29c)**, indicating that the system was efficiently taken up by cells and suggesting internalization by the Gt1b receptor.

Cells were also analyzed by flow cytometry after incubation periods of 1 hour at 37˚C with the same systems **(Fig. 30)**. Results showed an increase in cell fluorescence when the targeting peptide was present in the system, as compared with both untreated cells and cells incubated with the StvBiot-rcON system. These results are consistent with the confocal microscopy analysis, confirming the targeting properties of the DNA hybridized PNA-Tet1 conjugate, and the ability to be specifically internalized by Gt1b receptors.

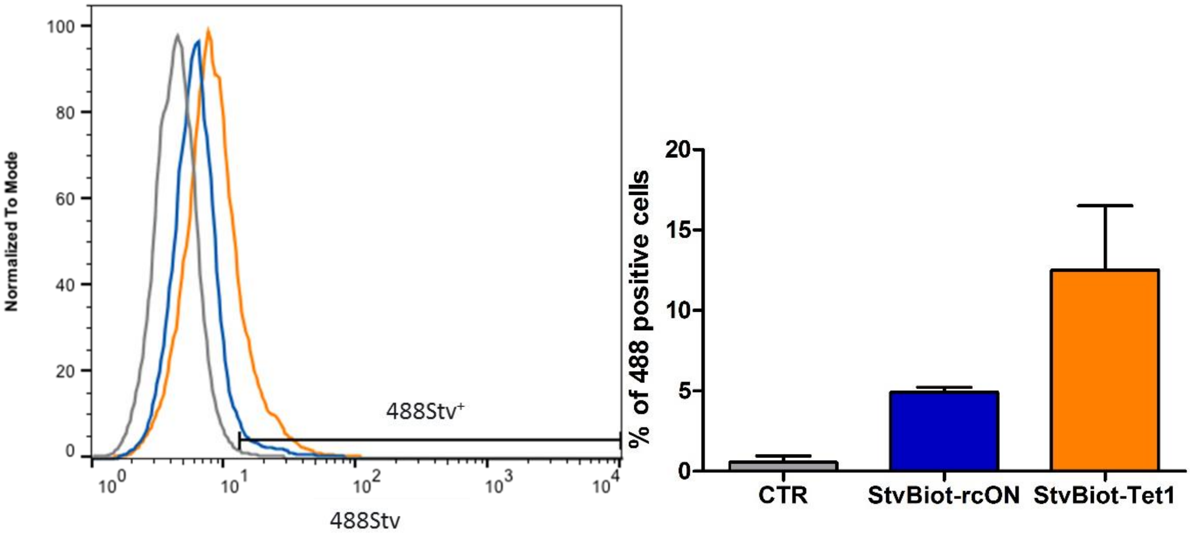

Figure 30 Cell association of StvBiot-rcON (blue) or StvBiot-Tet1 (orange) assessed by flow cytometry. A histogram of the cell signal intensity at 488nm is represented on the left with untreated cells in grey and cells incubated with either StvBiot-rcON in blue or StvBiot-Tet1 in orange. On the right the percentage of 488 positive cells is depicted graphically, considered taking into account the autofluorescence signal of untreated cells (CTR). Results obtained from two independent experiments.

The results from the incubation of the StvBio-Tet1 system with cells showed an enhanced cell internalization when the Tet1 targeting peptide was conjugated to a PNA hybridized to a simple DNA-Streptavidin system. This suggests that ligand receptor interactions are maintained even in presence of a possible excess of PNA-Tet1 conjugate in the samples, as mentioned before. Nevertheless, some level of undesired blocking of Gt1b receptors could still occur by the excess PNA-Tet1, meaning that the results obtained should still be regarded as underestimations of the full potential of the system.

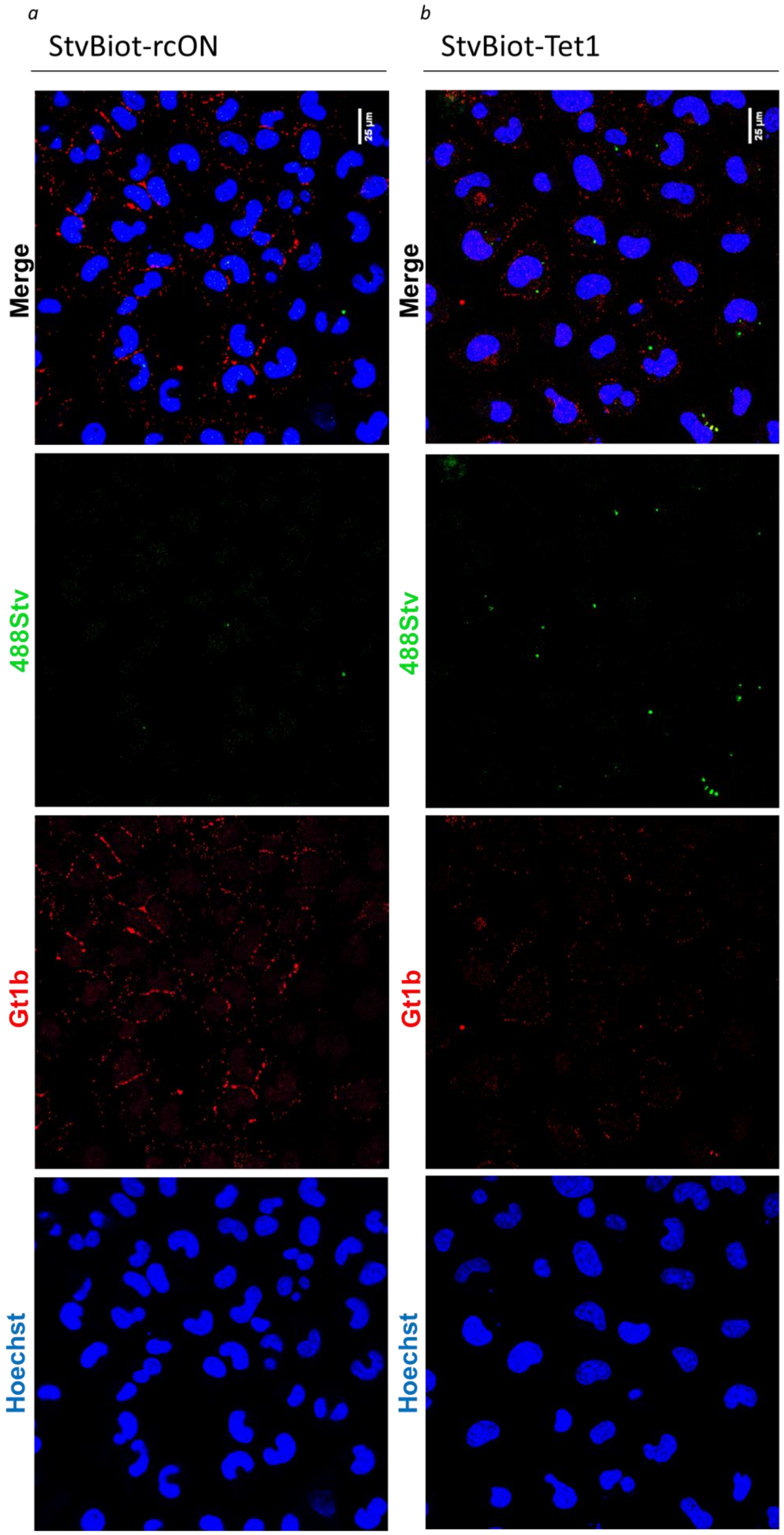
a
StvBiot-rcON
b
StvBiot-Tet1
25 µm
25 µm
Merge
Merge
488Stv
488Stv
Gt1b
Gt1b
Hoechst
Hoechst

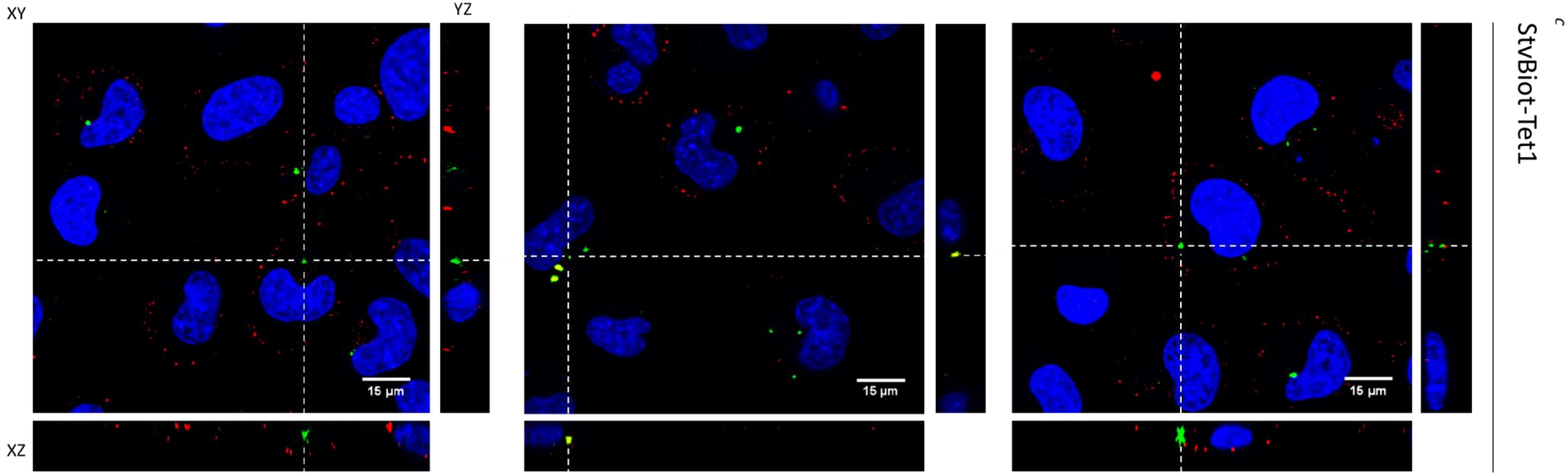

Figure 29 ND7/23 cell association of StvBiot conjugated to either a (a) control reverse complementary ssDNA or (b) the targeting peptide Tet1. Scale bars: 25 µm. (c) Orthogonal views from different planes (x/y, x/z or y/z) of StvBiot-Tet1 treated cells confirm that the 488 labeled system localizes inside the cell (left) and co-localizes or is in close proximity with Gt1b receptor (middle and right). Scale bars: 15 µm.

3.5. TDN NEURONAL TARGETING BY TET1 PEPTIDE

3.5.1. PAGE CHARACTERIZATION OF THE TDN-TET1 SYSTEM

After confirming functionality of the PNA-Tet1 peptide conjugate in a simpler arrangement, TDN-Tet1 system studies followed.

First, a PAGE analysis of the system was done **(Fig. 31)**. Several ratios were tested, in order to optimize the annealing of all three ssDNA anchors with the PNA-Tet1 conjugate. For the same reasons abovementioned, we were not able to consistently observe a predominant band in the gel resultant from a shift of the TDN once hybridized to the PNA-Tet1 conjugate. Nevertheless, at the higher ratios tested, the TDN band starts do disappear, suggesting some level of interaction is occurring with the PNA-Tet1 conjugate. Still, at the 1:5 ratio we could observe three faint bands that suggest a shift of the TDN when hybridized to 1, 2 or 3 PNA conjugates **(Fig. 31** inset**)**, although with low efficiency, as expected.

As previously mentioned, the low hydrophilicity of the PNA conjugate (despite dissolving in 10% DMSO) results in a low amount of solubilized conjugate that is able to successfully hybridize with the complementary TDN anchor sequences. This translates into the necessity to add higher amounts of the PNA conjugate to the TDN to compensate for this effect.

Additionally, as referred in **Fig. 21**, some steric hindrance might be lowering the efficiency of hybridization between the PNA conjugate and the TDN anchors.

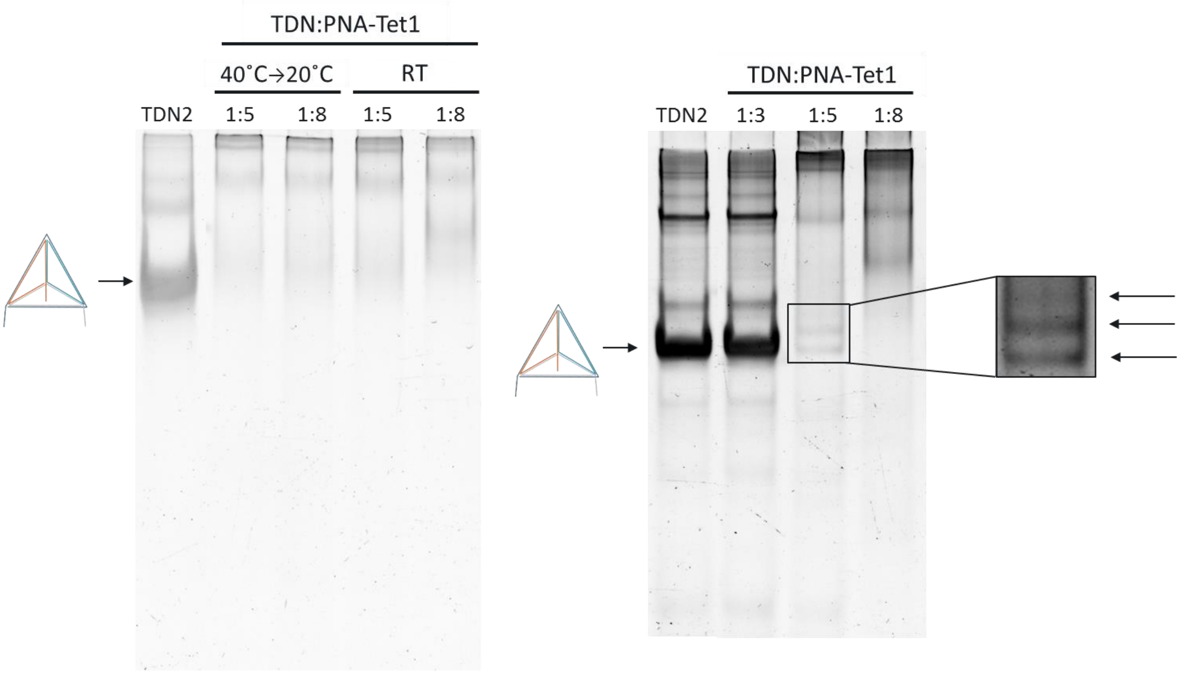

Figure 31 PAGE analysis of the system TDN-Tet1. Two different ratios were tested as well as different temperatures for the annealing between the ssDNA anchors of TDN and the complementary ssPNA of the PNA-Tet1 conjugate: an incubation of 3 min at 40˚C and cooling down to 20˚C in 1 hour or an incubation of 1 hour at room temperature (left). In a different experiment three ratios were tested, with an incubation of 1 hour at room temperature. The tetrahedron band is schematically indicated to the left of the gel. Inset: for clarity purposes, a high contrast image indicates the presence of higher mass structures immediately above the tetrahedron band.

3.5.2. IN VITRO UPTAKE STUDIES OF TDN-TET1

Next, uptake studies of the neuronal-targeting TDN-Tet1 system here developed were done. Confocal microscopy analysis of differentiated ND7/23 cells incubated with both "naked" FAM-labelled TDN (without any PNA-Tet1) and targeting FAM-labelled TDN-Tet1 structures (with PNA-Tet1) was performed **(Fig. 32)**. Relative short time points (1-3 hours) were used, in order to limit unspecific uptake.

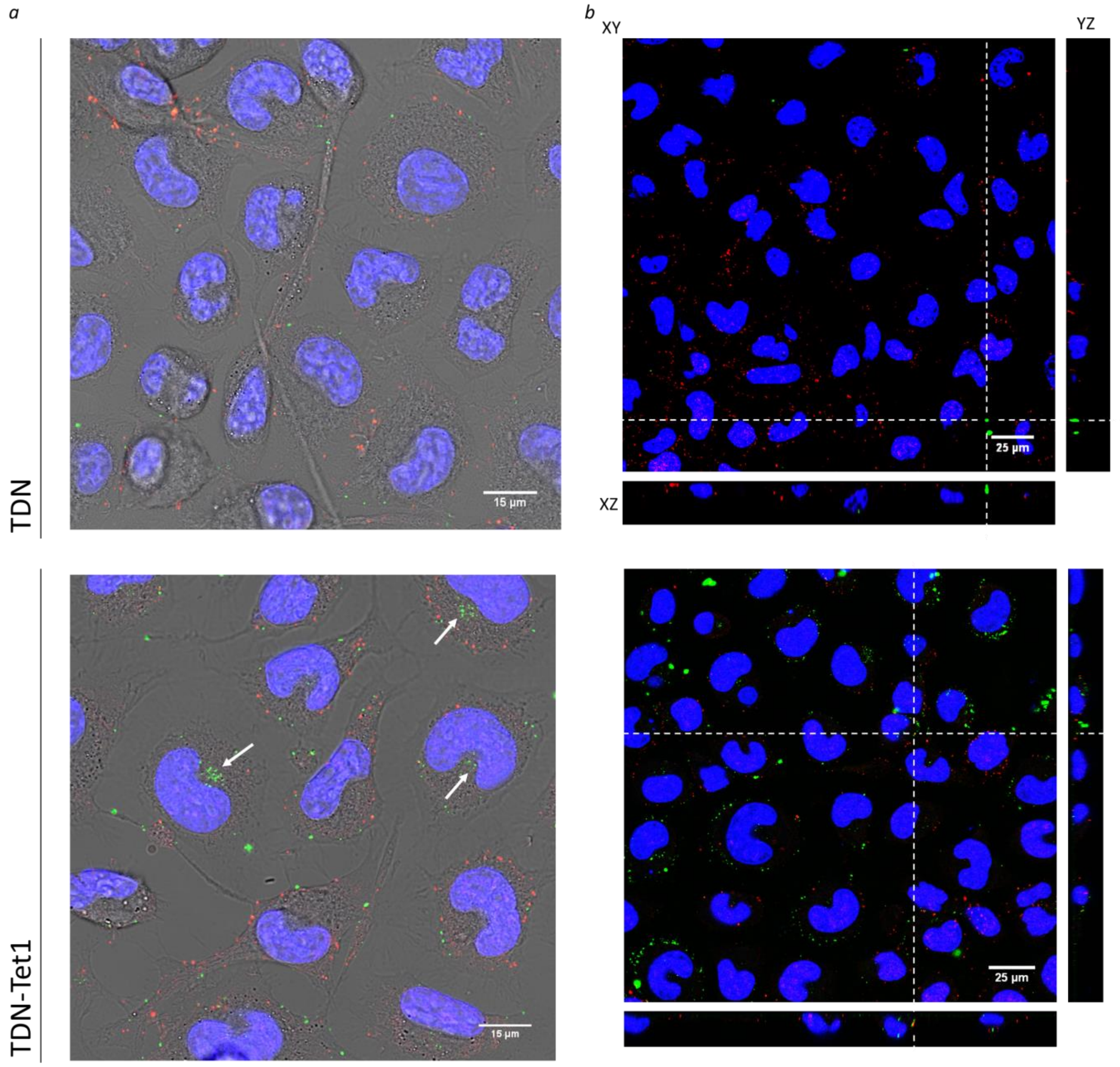

Figure 32 Representative images of the confocal analysis of differentiated ND7/23 cells incubated with naked TDN and TDN-Tet1 systems for 1 hour at 37˚C. (a) Incubations done at a final concentration of 0.05 µM of each system. Arrows point to TDN-Tet1 structures in close proximity to the nuclei. Scale bars: 15 µm. (b) Orthogonal views (x/y, x/z or y/z) of cells incubated at a concentration of 0.025 µM with each system indicate the co-localization of the FAM-labelled TDN-Tet1 and the Gt1b signals (bottom), while no apparent co-localization exists in the signals from the naked TDN and the Gt1b receptor (top). Nuclei are stained with Hoechst 33342 (blue), FAM-labelled TDNs are represented in green and Gt1b receptor in red. Scale bars: 25 µm.

Images revealed a higher number of cells with fluorescent TDN signals when using the targeted TDN-Tet1 system, comparing with cells incubated with the naked TDN **(Fig.32)**, which indicates that there is a higher cell association with TDN-Tet1. The few signals coming from cells incubated with the naked TDN were mostly localized to the cell periphery. In contrast, within 1 hour of incubation, the presence of TDN-Tet1 systems was observed not only in the periphery but also in close proximity to the nucleus (as indicated by arrows **Fig. 32a**), suggesting quick internalization and trafficking in the cells. This observation suggests the occurrence of vesicular transport of these systems after internalization, and is in accordance with previous studies using Tet1-PEI nanoparticles (Park, Lasiene, Chou, Horner, & Pun, 2007). Furthermore, 3D reconstruction of images through orthogonal views **(Fig. 32b)** enabled the identification of co-localizing signals of TDN-Tet1 systems (green) and Gt1b receptor (red), suggesting specific receptor-mediated uptake. Expectedly, the same was not observed in cells treated with naked TDN. These results confirm the neuronal-targeting properties of the PNA-Tet1 conjugate incorporated into the DNA nanostructure.

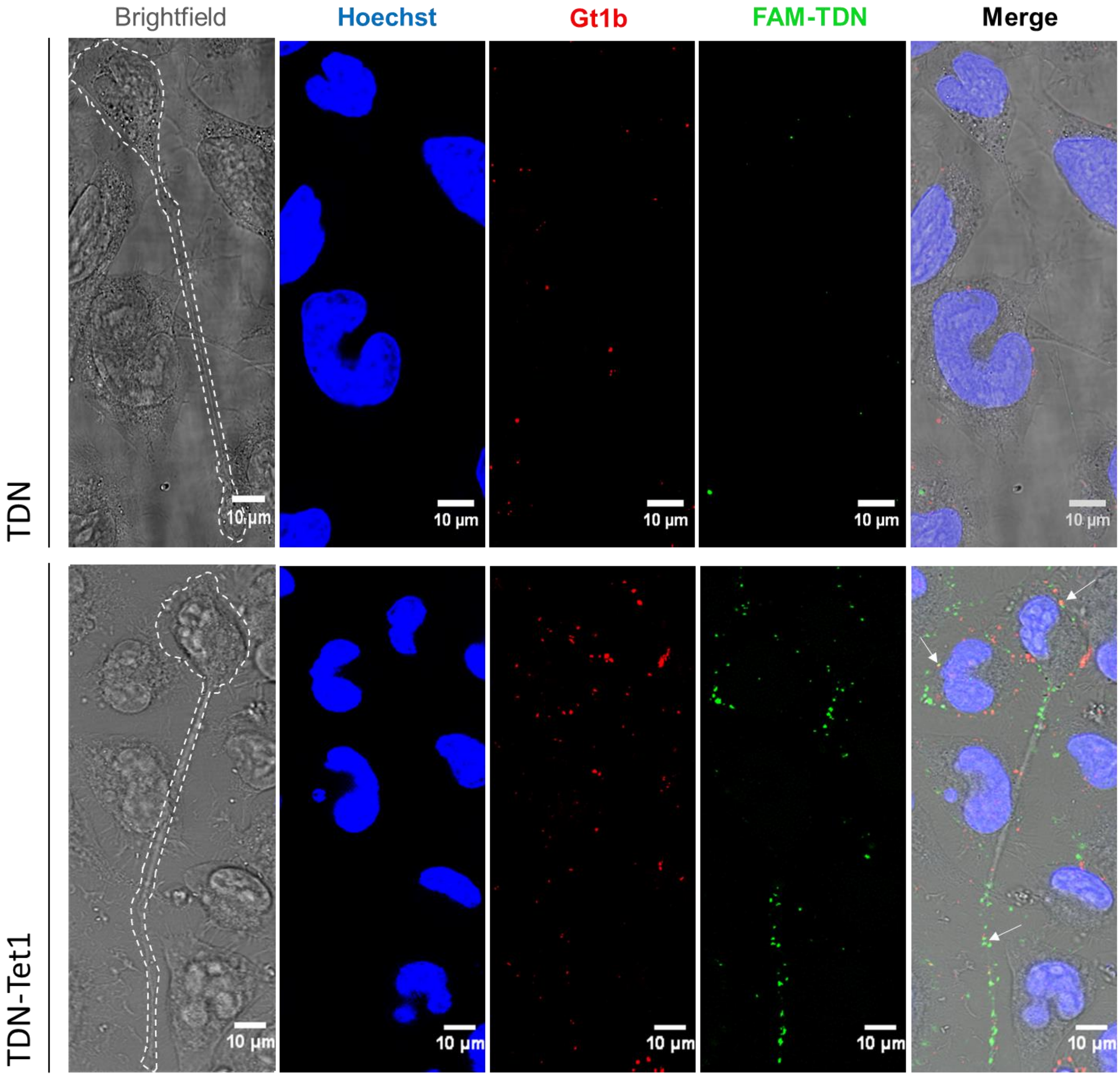

Figure 33 Representative confocal images focusing on differentiated ND7/23 cells showing neurite-like extensions (highlighted by a white dotted line in the brightfield images) after incubation for 3 hours with either the naked TDN (top) or the TDN-Tet1 (bottom) system at a concentration of 0.025 µM. White arrows indicate sites of co-localization of the TDN-Tet1 signal (green) and the Gt1b receptor signal (red). Scale bars: 10 µm.

In a different set of experiments, (with differentiated ND7/23 cells incubated with both systems for 3 hours, at 37˚C) **(Fig.33)**, image analysis revealed the localization of several TDN-Tet1 systems along neurite extensions. This observation evidences the possibility of the TDN-Tet1 structures to be taken up not only by cell bodies, a place where endocytosis is more prone to occur, but also either along the neuronal extensions or by the extensions termini with subsequent intracellular transport along the neurite up to the cell body. This could be of relevance for neurotherapeutics, where for instance a TDN structure could be taken up by a neuronal cell through its neuro-muscular junction and retrogradely travel along the axon finally accessing the central nervous system (CNS) while bypassing the blood-brain-barrier (McCall et al., 2014; Townsend et al., 2007).

Uptake studies were then conducted in energy-depleted conditions, by incubating cells with naked TDN and TDN-Tet1 systems at 4˚C. Confocal microscopy analysis revealed a dramatic reduction in the signal of both systems **(Fig. 34)**, when comparing with incubations performed at 37˚C. Under these conditions, cells incubated with naked TDN presented minimal fluorescence signals, indicating low levels of cellular association or internalization. On the contrary, cells treated with TDN-Tet1 systems still presented significant levels of fluorescence mostly limited to the cellular periphery. Moreover, in cells incubated with the neuronal-targeting TDN-Tet1 system, the fluorescence signal distribution was very different from the obtained when incubated at 37˚C **(Fig. 32)**. The observation of no fluorescence signal in the interior of cells, more specifically proximal to the nucleus, and a clear localization of the structures at the cell periphery, confirms the blocking of GT1b-mediated internalization processes. Thus, the presence of clearly visible fluorescence signals at the cell periphery, in contrast to the naked TDN, reflects the ability of the Tet1 peptide to still bind to the Gt1b at low temperature although the internalization processes are blocked.

These results demonstrate that both the unspecific uptake of naked TDN and the specific uptake of TDN-Tet1 systems are energy-dependent, since at 4˚C all active energy-dependent processes are suspended. This is in accordance to the described caveolin-dependent endocytosis of naked tetrahedral DNA nanostructure, while residual fluorescent signal may occur by TDN adsorption to the cell membrane (Liang et al., 2014).

In order to accomplish a semi-quantitative study of cell uptake we next performed Image Stream analysis of differentiated ND7/23 cells incubated with targeting TDN-Tet1 system, naked TDN, as well as a single strand DNA (s4b) as an extra control **(Fig. 35)**.

As expected, cells incubated with the ssDNA molecule did not reveal a significant difference in the cell intensity, as compared with untreated cells, indicating minimal uptake (membrane- and cytoplasm-associated intensity analysis in **Fig. S4**). Cells incubated with unmodified TDN revealed a significant increase in the uptake of the nanostructure, as evidenced by higher cell fluorescence intensity values, comparing with both untreated cells and cells treated with the ssDNA molecule, confirming the increased cell permeability to structured DNA. It must be noted that s4b presented one FAM molecule per strand, as opposed to the four FAM molecules in the TDN. Although it is not possible to directly compare fluorescence intensities between TDN structures and the single stranded s4b, we performed an analysis by spot counting which is made independent of the intensity (representative images for spot counting analysis in **Fig. S4c**). Spot count can correlate with the appearance of intracellular vesicle-like structures or aggregates indicating cytoplasmic localization after uptake. Spot count analysis revealed a lower number of intracellular structures by the incubation with s4b in comparison with the TDN **(Fig. 33b)**. Cells incubated with the targeting TDN-Tet1 system revealed the highest fluorescence levels, indicative of increased uptake. Higher frequencies of cells with greater numbers of fluorescent spots, were as well observed, confirming the influence of the targeting moiety in mediating increased uptake of the TDN nanostructure and our previous microscopy results.

In order to verify the cell specificity of the designed TDN-Tet1 system, the same analysis was performed in NIH 3T3, a fibroblast cell line **(Fig. 36)**, confirmed to have no expression of Gt1b at the cell surface. Cells incubated with s4b did not reveal a significant difference in the cell fluorescence intensity, by comparison with untreated cells, indicating no significant uptake of this molecule, as predicted. When cells were incubated with naked TDN, a significant increase in the fluorescence signal (relative to untreated cells and cells treated with both the ssDNA molecule and the TDN-Tet1 system) was observed. This was accompanied by higher numbers of fluorescence spots, indicating increased cell internalization of the TDN nanostructure (**Fig. S5c**). Interestingly, the fluorescence increase was substantially higher than the one obtained with differentiated ND7/23 cells. On the contrary, cells incubated with the neuronal-targeting TDN-Tet1 system did not present a significant increase in cell intensity, as compared to the control conditions. There was a clear decrease on the uptake of TDN-Tet1 structures in relation to unmodified TDN, revealing no significant cellular uptake by this non-neuronal cell line. Such a considerable difference in the uptake of these structures was not predicted.

Further analysis must be done in order to completely understand the observed events, but several conditions might be leading to this result. First, this fibroblastic cell line, as a fast tumor-growing cell line, presents increased unspecific endocytosis in relation to differentiated ND7/23 cells, which might explain the augmented unspecific internalization of the TDN in NIH 3T3 cells. One possible reason for the TDN-Tet1 to have lower uptake than the naked TDN could derive from an unknown shielding effect by the presence of the PNA-Tet1 conjugates. The peptides possess positive as well as hydrophobic aminoacids, localized mainly in one modified TDN face (see **Fig. 17**), which can eventually make a first contact with the cell surface rather than the faces with more highly negative net charge. Such non-optimal binding events could lead to a partial shielding, lowering the uptake mediated by the recognition of a dense negative charge in structured DNA as is the case of the naked TDN. Another possibility could result from a certain tendency of the PNA-Tet1 conjugates to aggregate which could lead to the presence of more than expected peptides bound to the TDN. These events could also lead to a shielding effect lowering uptake in relation to naked TDN.

The observed difference in the uptake of TDN-Tet1 system in the fibroblast cell line when compared to the neuronal-type cells, demonstrate the specificity of the targeting achieved by the TDN nanostructures modified with the PNA-Tet1 conjugates, and the involvement of Gt1b receptor-ligand interactions.

Our results are in accordance to previous studies using polymer-based DNA nanocomplexes modified with Tet1 peptides showing specific uptake by neuron-like cells (Park et al., 2007). However, it is important to note that while in the polymer-based system it is not known the exact number of Tet1 molecules per nanocomplex mediating cell uptake, with the DNA nanostructure system that number is possible to know and ranges from 1-3 Tet1 peptides per structure, in an optimized system. Another fundamental difference relates to the charge of the polymer-based nanocomplex, which is cationic in nature, while the DNA nanostructure here described is highly negative. A cationic charge can normally have a beneficial effect in cell internalization by aiding through electrostatic interactions with cell membranes. In the DNA nanostructure system, we have observed that the Tet1 peptide was still able to mediate specific uptake while in presence of a highly negatively charged environment.

As mentioned above, these results might be further improved by the redesign of the PNA-Tet1 conjugate, in order to obtain an optimized annealing with the TDN anchors, thus avoiding the need for excess conjugate. Present PNA-Tet1 conjugate not annealed with the TDN might be blocking Gt1b receptors, altering the results.

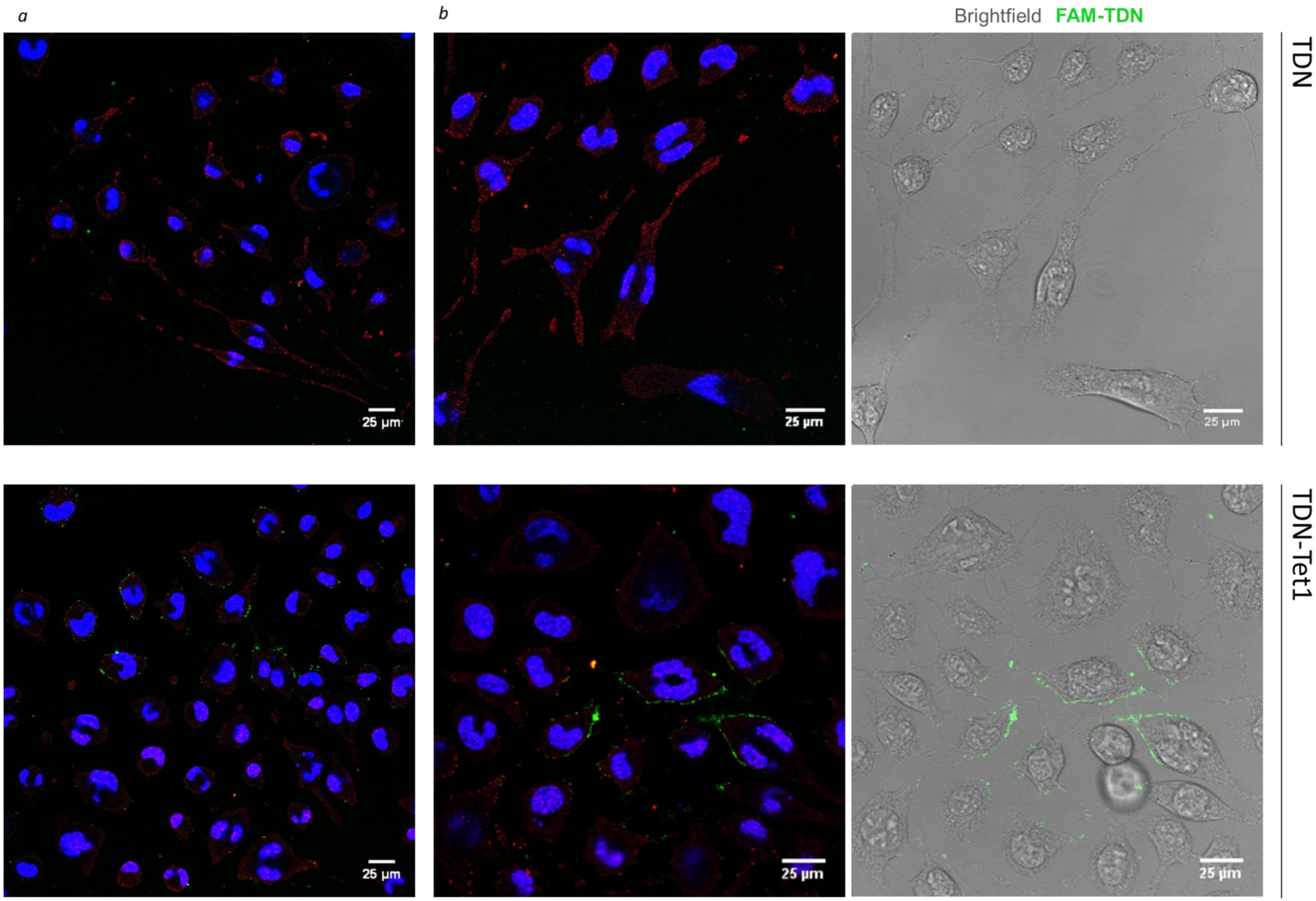

Figure 34 (a and b) Confocal microscopy representative images of differentiated ND7/23 cells incubated with naked TDN and neuronal targeting TDN-Tet1 systems for 2 hours at 4˚C (0.025 µM). (b) Duplicate images for clarity purposes, brightfield and FAM-TDN merged images elucidate the localization of the structures within the cell. Scale bars: 25µm. Nuclei are stained with Hoechst 33342 (blue), FAM-labelled TDNs are represented in green and Gt1b receptor is stained in red.

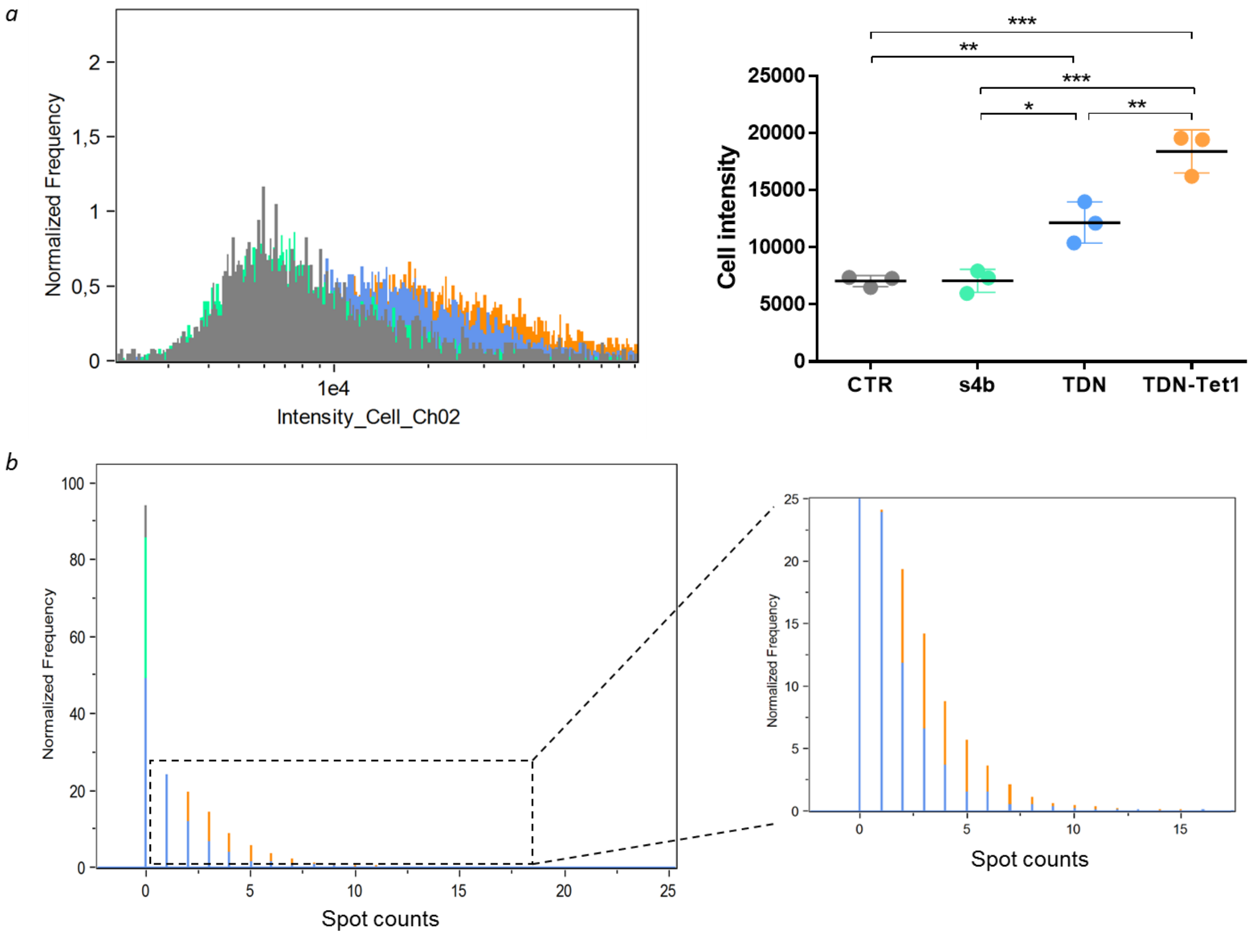

*Figure 35 Image Stream analysis of untreated differentiated ND7/23 (CTR - grey) and differentiated ND7/23 incubated with FAM-s4b (green), FAM-TDN (blue) and FAM-TDN-Tet1 (orange). (a) Cellular uptake was assessed according to the fluorescence intensity in the cell, as depicted in the representative histogram (left). Cellular intensity is translated into median values graphically represented (right). Results obtained from three independent experiments. (b) Fluorescence spots in the cells were measured, making use of spot masks and spot-counting features. A representative histogram of spot-count normalized frequencies is on the left, zoomed in on the right. * denotes statistical significance between samples, using repeated measures one-way ANOVA statistical analysis. * p < 0,05; ** p < 0,01; *** p < 0,001;*

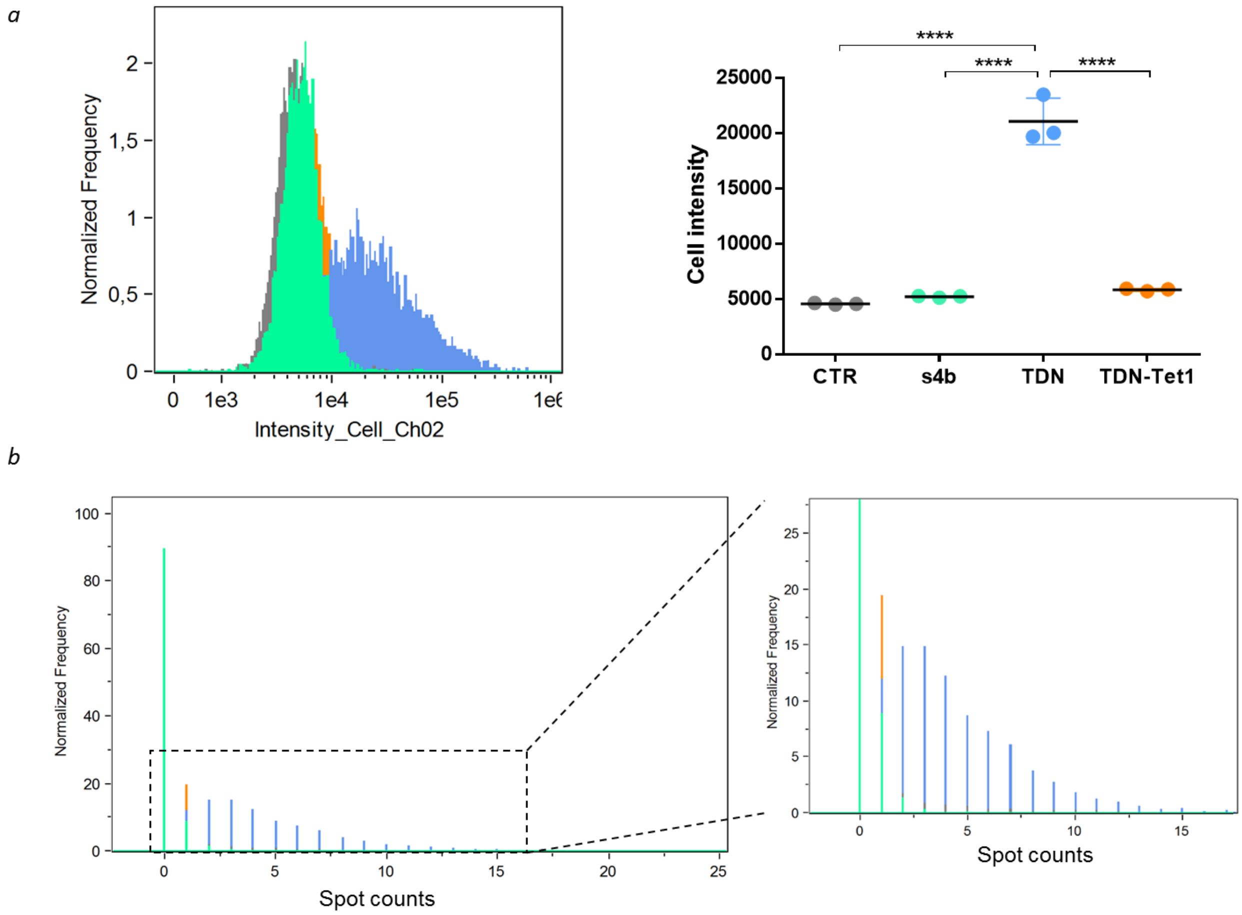

*Figure 36 Image Stream analysis of untreated (CTR - grey) cells and NIH 3T3 cells incubated with FAM-s4b (green), FAM-TDN (blue) and FAM-TDN-Tet1 (orange). (a) Cellular uptake was assessed according to the fluorescence intensity in the cell, illustrated in the representative histogram (left), and translated into graphically represented median values (right). Results obtained from three independent experiments. (b) Fluorescence spots in the cells were measured, making use of spot masks and spot-counting features. A representative histogram of spot-count normalized frequencies is on the left, zoomed in on the right. * denotes statistical significance between samples, using repeated measures one-way ANOVA statistical analysis. **** p < 0,0001.*

CHAPTER 4

CONCLUSION AND FUTURE PERSPECTIVES

CONCLUSION

From all the biomedical fields, neurotherapeutics appears to be one of the domains with the highest unmet clinical successes rate. Adding to the list of limitations most therapeutics face – such as presenting stability in physiological conditions, resisting renal clearance, evading the immune system, reaching its site of actions without adverse effects -, the special complexity and sensitivity of the neural network require exceptional measures to address neurological issues.

DNA nanotechnology has proved to be one of the most promising approaches, currently being studied, towards filling existing gaps in the field of biotechnology. All types of structures with the most various applications have been successfully reported: from simple arrangements designed to display reporter probes to complex smart drug delivery platforms. DNA-based nanostructures have the potential to satisfy all the requirements for a safe and effective nanotool, with unique features that allow the production of a molecularly identical population of structures with well-defined, controllable properties and molecular addressability.

Here we report a novel tailor-made DNA-based nanostructure, with the ability of specifically targeting neuronal cells, as a potential new tool in neurotherapeutics.

Making use of DNA nanotechnology principles, and combining innovative synthetic nucleic-acid tools and DNA self-assembly features, a strictly defined neuronal-targeting TDN was designed.

The adopted strategy was the multistrand approach for the construction of a DNA-based tetrahedron from four ssDNA sequences. The novelty of the assembled TDN is related with the structure bearing three ssDNA anchors through which the neuronal targeting Tet1 peptide can be incorporated, by simple annealing between the TDN DNA anchors and a PNA-Tet1 conjugate.

In the present thesis, the assembly, characterization, and evaluation of the TDN-Tet1 system were accomplished. Cellular uptake studies revealed an enhanced and specific internalization of the TDN-Tet1 system by neuronal-like differentiated ND7/23 cells, due to specific recognition of the target ganglioside receptor. Inversely, no internalization was observed with control NIH 3T3 fibroblast cells, demonstrating the specificity of the DNA nanostructure system. Obtained results suggest that the TDN-Tet1 system here designed and studied could represent a potential nanotool for neuronal applications.

The application of DNA nanotechnology for the tailored treatment of neuropathies seems to be a promising new avenue one should definitely address. The system here reported, as a newcomer in this study area, provides the opportunity and the potential to be successfully developed into a smart drug delivery system or a sensitive biosensing device for neurotherapeutic applications.

FUTURE PERSPECTIVES

The work here presented corresponds to the first part of a project that aims at the development of a neurotherapeutic nanotool. After succeeding with the design and basic functionalities of the tetrahedral DNA structure, evidencing accomplished specific neuronal targeting by the incorporation of Tet1 peptide, several points deserve further attention.

First off, other possible purification protocols should be tested, since the one here described is very time-consuming and demands several steps to be taken in order to obtain optimal recovery in a final high sample concentration. Size exclusion chromatography - high-performance liquid chromatography (SEC-HPLC) has been recently introduced as a possible high-yielding purification method. Apart from being a simpler and large-scale adapted method, aggregation, degradation and/or re-assembly events that occur during processing of gel-containing DNA structures are minimized.

The performance of the PNA-Tet1 conjugate greatly affects the functionality of the TDN-Tet1 system. As already discussed, the level of hydrophobicity of the conjugate must be addressed, either through the incorporation of solubility enhancers or by decreasing the percentage of purine bases of the PNA (which present a tendency to aggregate in aqueous solutions). An additional approach is the redesign of the anchors, as well, given the possible steric constraints due to the close proximity of the annealing site and the rigid assembled tetrahedron.

For the construction of a structure with improved functionality, the number of targeting peptides per structure and their relative orientation should also be studied, since the nature of the system in study allows for this type of analysis.

The novel structure here designed, presents single-stranded DNA anchors at three vertices of the tetrahedron, which can anneal with respectively three ssPNA-peptide conjugates. Although previous studies addressing the stability and degradation resistance of TDNs have been made, it would be desirable to understand if the modified TDN maintains the reported stabilities. For that, temperature-dependent disassembly and enzymatic degradation must be firstly addressed, and further accompanied by, for instance, FRET analysis to assess structural integrity within cells at several time points.

Uptake tests in isolated rat primary neurons, as well as co-cultures with non-neuronal cells, need to be performed to further confirm TDN-Tet1 functionality and specificity. Finally, assessment of the TDN structure biodistribution and internalization *in vivo* upon, for instance, intracerebroventricular injections should be conducted to access its potential in the CNS.

As a promising therapeutic candidate, the structure here described can be precisely modified to incorporate different moieties, for example a molecular beacon that integrates into a sensitive neurological biosensor or siRNA molecules for smart neurotherapeutics delivery.

Major work and improvements are still to be done, nevertheless results herein discussed confirm the fact that DNA nanotechnology is a promising approach for achieving selective and controlled therapeutic applications.

SUPPLEMENTARY INFORMATION

APPENDIX A

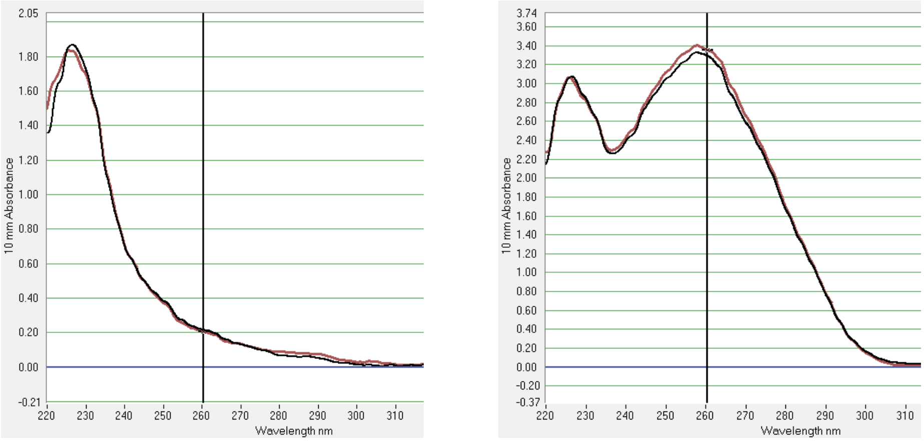

Figure S1 UV spectra of a purified TDN1 sample pre- (left) and post-desalting (right).

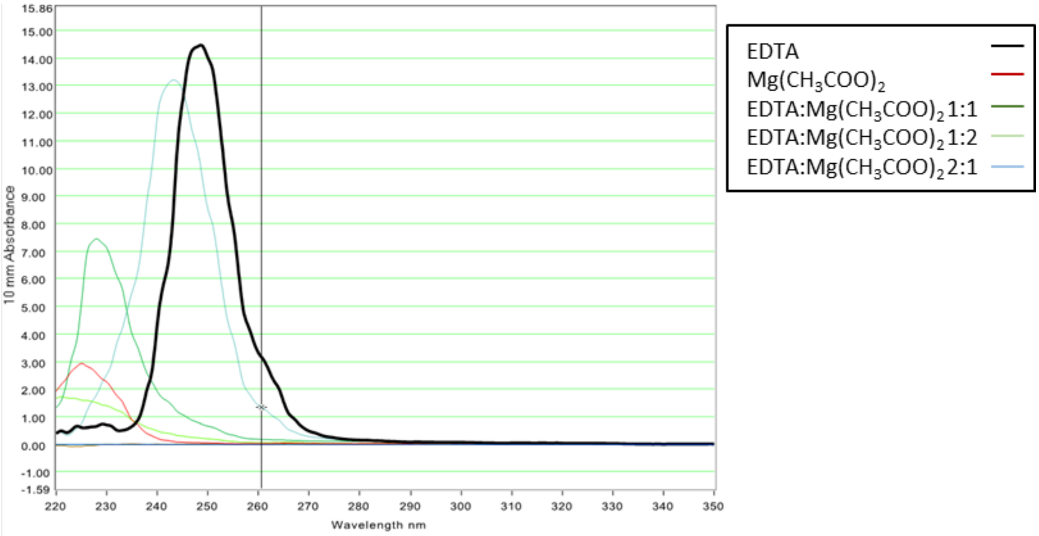

Figure S2 UV spectra of a range of possible contaminants in the purified sample prior to the desalting step.

APPENDIX B

The input code for the generation of novel TDN sequences in NUPACK follows:

```
# example physical properties
temperature = 37
material = dna
trials = 3
sodium = 0.15

# domains for the T1 of the tetrahedron
domain h = A
domain i = N20

# domains for T2 of the tetrahedron
domain j = A
domain k = N20
domain l = A
domain m = N20
domain p = CAATAATGACTAAAAGCG
domain o = CAATAATGACTAAAAGCG
domain n = A
domain r = A

# domains for T3 of the tetrahedron
domain a = N20
domain b = A
domain c = A
domain d = N20
domain e = A
domain f = N20
domain g = A
domain q = CAATAATGACTAAAAGCG


# strands for T1 of the tetrahedron
strand S1_2 = h i
strand S4_1 = i*
# strands for T2 of the tetrahedron
strand S3_2 = j k r m p
strand S4_3 = n m*
strand S1_3 = l k* o
# strands for T3 of the tetrahedron
strand S1_1 = a
strand S2 = a* b d e f q
strand S3_1 = d*
strand S4_2 = g f*#


# DU+ and bracket notation for the three complexes
structure T1 = U1 D20 +
structure T2 = .((((((((((((((((((((.((((((((((((((((((((..................+.))))))))))))))))))))+.))))))))))))))))))))..................
structure T3 = ((((((((((((((((((((.((((((((((((((((((((.((((((((((((((((((((..................+.))))))))))))))))))))+))))))))))))))))))))+))))))))))))))))))))
# associated strand sequences and structures
T1.seq = S1_2 S4_1
T2.seq = S3_2 S4_3 S1_3
T3.seq = S2 S4_2 S3_1 S1_1
# add all structures as on-targets for to a single tube and set optimization parameters
tube tetrahedron = T1 T2 T3
tetrahedron.maxsize = 3
tetrahedron.stop[%] = 5.0
prevent = CCCC, GGGG, CCCCC, GGGGG
```

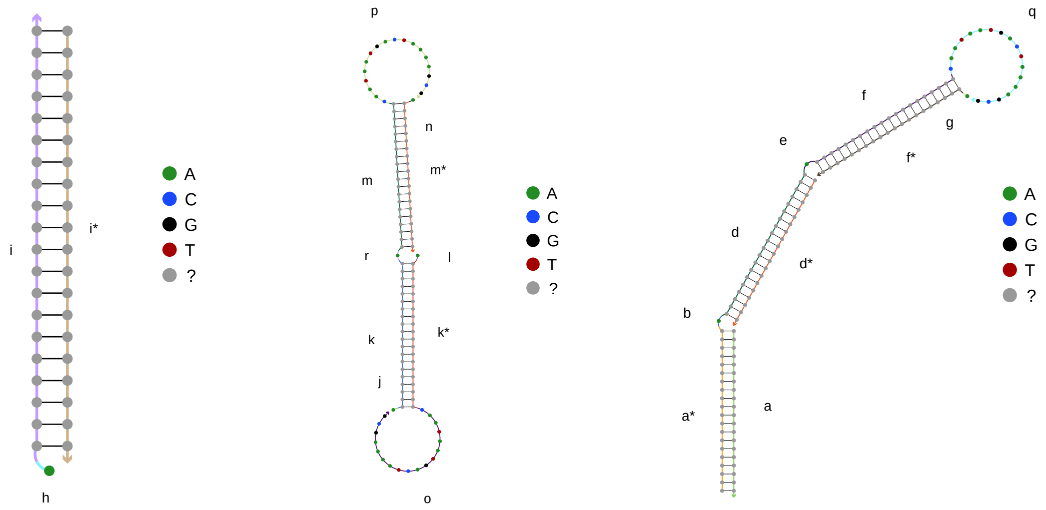

Figure S3 Representation of predicted substructures as a result of the input code, and prior to nucleotide bases attribution.

APPENDIX C

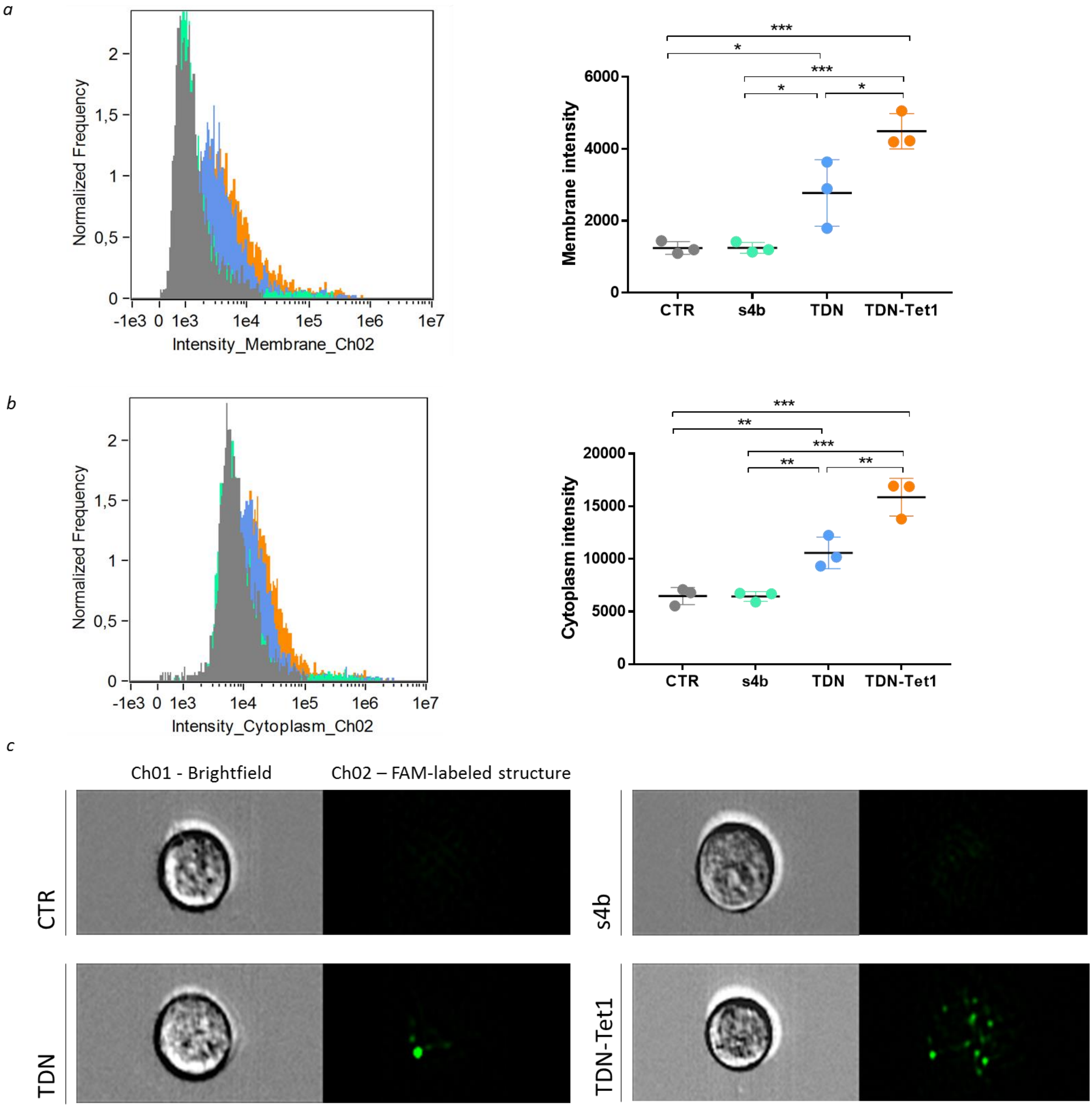

Figure S4 Image stream analysis of (a) membrane and (b) cytoplasm intensity of differentiated ND7/23 cells incubated with FAM-s4b (green), FAM-TDN (blue) and FAM-TDN-Tet1 (orange). (c) Representative brightfield and fluorescence images acquired for each condition. Spot-counting was done using images collected in Channel 02, through the use of masks that discriminate bright fluorescence spots.

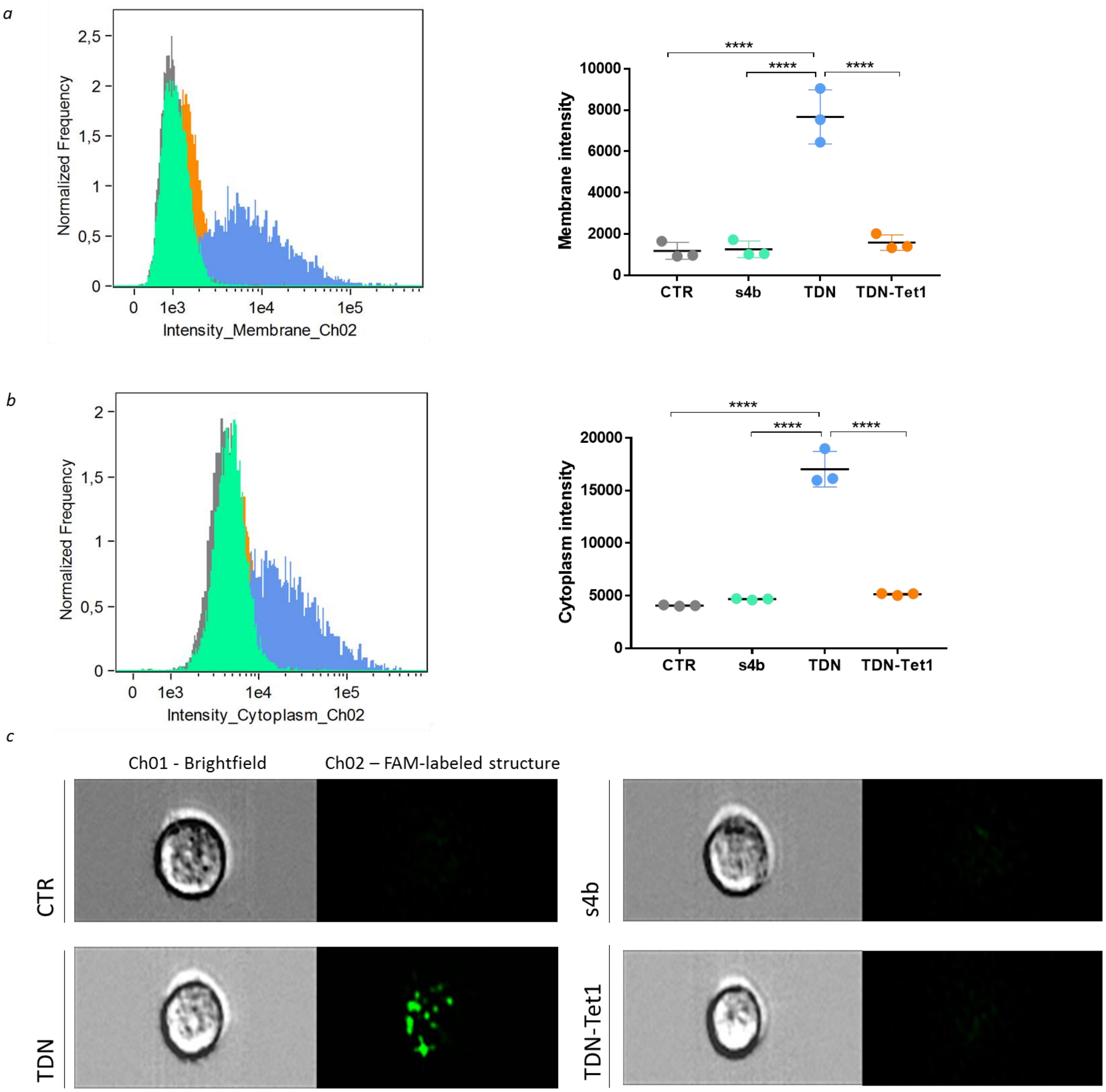

Figure S5 Image stream analysis of (a) membrane and (b) cytoplasm intensity of NIH 3T3 cells incubated with FAM-s4b (green), FAM-TDN (blue) and FAM-TDN-Tet1 (orange). (c) Representative brightfield and fluorescence images acquired for each condition. Spot-counting was done using images collected in Channel 02, through the use of masks that discriminate bright fluorescence spots.

REFERENCES

Ahnert-Hilger, G., Dauzenroth, M. E., Habermann, E., Henschen, A., Krieglstein, K., Mauler, F., & Weller, U. (1990). Chains and fragments of tetanus toxin, and their contribution to toxicity. *Journal de Physiologie*, *84*(3), 229–36. Retrieved from http://www.ncbi.nlm.nih.gov/pubmed/2074546

Amir, Y., Ben-Ishay, E., Levner, D., Ittah, S., Abu-Horowitz, A., & Bachelet, I. (2014). Universal computing by DNA origami robots in a living animal. *Nat Nano*, *9*(5), 353–357. Retrieved from http://dx.doi.org/10.1038/nnano.2014.58

Balyasnikova, I. V, Prasol, M. S., Ferguson, S. D., Han, Y., Ahmed, A. U., Gutova, M., … Lesniak, M. S. (2014). Intranasal delivery of mesenchymal stem cells significantly extends survival of irradiated mice with experimental brain tumors. *Molecular Therapy : The Journal of the American Society of Gene Therapy*, *22*(1), 140–8. Retrieved from http://dx.doi.org/10.1038/mt.2013.199

Benabou, S., Avino, A., Eritja, R., Gonzalez, C., & Gargallo, R. (2014). Fundamental aspects of the nucleic acid i-motif structures. *RSC Advances*, *4*(51), 26956–26980. http://doi.org/10.1039/C4RA02129K

Bhatia, D., Surana, S., Chakraborty, S., Koushika, S. P., & Krishnan, Y. (2011). A synthetic icosahedral DNA-based host–cargo complex for functional in vivo imaging. *Nat Commun*, *2*, 339. Retrieved from http://dx.doi.org/10.1038/ncomms1337

Bizzini, B., Stoeckel, K., & Schwab, M. (1977). AN ANTIGENIC POLYPEPTIDE FRAGMENT ISOLATED FROM TETANUS TOXIN: CHEMICAL CHARACTERIZATION, BINDING TO GANGLIOSIDES AND RETROGRADE AXONAL TRANSPORT IN VARIOUS NEURON SYSTEMS. *Journal of Neurochemistry*, *28*(3), 529–542. Retrieved from http://doi.wiley.com/10.1111/j.1471-4159.1977.tb10423.x

Boyd, J. G., & Gordon, T. (2003). Glial cell line-derived neurotrophic factor and brain-derived neurotrophic factor sustain the axonal regeneration of chronically axotomized motoneurons in vivo. *Experimental Neurology*, *183*(2), 610–619. http://doi.org/http://dx.doi.org/10.1016/S0014-4886(03)00183-3

Bujold, K. E., Fakhoury, J., Edwardson, T. G. W., Carneiro, K. M. M., Briard, J. N., Godin, A. G., … Sleiman, H. F. (2014). Sequence-responsive unzipping DNA cubes with tunable cellular uptake profiles. *Chemical Science*, *5*(6), 2449–2455. http://doi.org/10.1039/C4SC00646A

Castro, C. E., Kilchherr, F., Kim, D.-N., Shiao, E. L., Wauer, T., Wortmann, P., … Dietz, H. (2011). A primer to scaffolded DNA origami. *Nat Meth*, *8*(3), 221–229. Retrieved from http://dx.doi.org/10.1038/nmeth.1570

Chang, M., Yang, C.-S., & Huang, D.-M. (2011). Aptamer-Conjugated DNA Icosahedral Nanoparticles As a Carrier of Doxorubicin for Cancer Therapy. *ACS Nano*, *5*(8), 6156–6163. http://doi.org/10.1021/nn200693a

Chang, N., El-Hayek, Y. H., Gomez, E., & Wan, Q. (2007). Phosphatase PTEN in neuronal injury and brain disorders. *Trends in Neurosciences*, *30*(11), 581–586. http://doi.org/10.1016/j.tins.2007.08.006

Charoenphol, P., & Bermudez, H. (2014). Design and application of multifunctional DNA nanocarriers for therapeutic delivery. *Acta Biomaterialia*, *10*(4), 1683–1691. http://doi.org/http://dx.doi.org/10.1016/j.actbio.2013.07.021

Chen, J., & Seeman, N. C. (1991). Synthesis from DNA of a molecule with the connectivity of a cube. *Nature*, *350*(6319), 631–633. Retrieved from http://dx.doi.org/10.1038/350631a0

Chu, D. S. H., Schellinger, J. G., Bocek, M. J., Johnson, R. N., & Pun, S. H. (2013). Optimization of Tet1 ligand density in HPMA-co-oligolysine copolymers for targeted neuronal gene delivery. *Biomaterials*, *34*(37), 9632–9637. http://doi.org/http://dx.doi.org/10.1016/j.biomaterials.2013.08.045

Coen, L., Osta, R., Maury, M., & Brûlet, P. (1997). Construction of hybrid proteins that migrate retrogradely and transynaptically into the central nervous system. *Proceedings of the National Academy of Sciences of the United States of America*, *94*(17), 9400–5. Retrieved from http://www.pubmedcentral.nih.gov/articlerender.fcgi?artid=23202&tool=pmcentrez&rendertype=abstract

Cutler, J. I., Zhang, K., Zheng, D., Auyeung, E., Prigodich, A. E., & Mirkin, C. A. (2011). Polyvalent Nucleic Acid Nanostructures. *Journal of the American Chemical Society*, *133*(24), 9254–9257. http://doi.org/10.1021/ja203375n

Davidson, B. L., & Paulson, H. L. (2016). Molecular medicine for the brain: silencing of disease genes with RNA interference. *The Lancet Neurology*, *3*(3), 145–149. http://doi.org/10.1016/S1474-4422(04)00678-7

de Vries, J. W., Zhang, F., & Herrmann, A. (2013). Drug delivery systems based on nucleic acid nanostructures. *Journal of Controlled Release*, *172*(2), 467–483. http://doi.org/http://dx.doi.org/10.1016/j.jconrel.2013.05.022

Demidov, V. V, Potaman, V. N., Frank-Kamenetskil, M. D., Egholm, M., Buchard, O., Sönnichsen, S. H., & Nlelsen, P. E. (1994). Stability of peptide nucleic acids in human serum and cellular extracts. *Biochemical Pharmacology*, *48*(6), 1310–1313. http://doi.org/http://dx.doi.org/10.1016/0006-2952(94)90171-6

Dietz, H., Douglas, S. M., & Shih, W. M. (2009). Folding DNA into Twisted and Curved Nanoscale Shapes. *Science (New York, N.Y.)*, *325*(5941), 725–730. http://doi.org/10.1126/science.1174251

Dominska, M., & Dykxhoorn, D. M. (2010). Breaking down the barriers: siRNA delivery and endosome escape. *Journal of Cell Science*, *123*(Pt 8), 1183–9. Retrieved from http://www.ncbi.nlm.nih.gov/pubmed/20356929

Douglas, S. M., Bachelet, I., & Church, G. M. (2012). A Logic-Gated Nanorobot for Targeted Transport of Molecular Payloads. *Science* , *335* (6070), 831–834. http://doi.org/10.1126/science.1214081

Douglas, S. M., Marblestone, A. H., Teerapittayanon, S., Vazquez, A., Church, G. M., & Shih, W. M. (2009). Rapid prototyping of 3D DNA-origami shapes with caDNAno. *Nucleic Acids Research*, *37*(15), 5001–5006. http://doi.org/10.1093/nar/gkp436

Egholm, M., Buchardt, O., Christensen, L., Behrens, C., Freier, S. M., Driver, D. A., … Nielsen, P. E. (1993). PNA hybridizes to complementary oligonucleotides obeying the Watson–Crick hydrogen-bonding rules. *Nature*, *365*(6446), 566–568. Retrieved from http://dx.doi.org/10.1038/365566a0

Egholm, M., Buchardt, O., Nielsen, P. E., & Berg, R. H. (1992). Peptide nucleic acids (PNA). Oligonucleotide analogs with an achiral peptide backbone. *Journal of the American Chemical Society*, *114*(5), 1895–1897. http://doi.org/10.1021/ja00031a062

Erben, C. M., Goodman, R. P., & Turberfield, A. J. (2006). Single-Molecule Protein Encapsulation in a Rigid DNA Cage. *Angewandte Chemie International Edition*, *45*(44), 7414–7417. http://doi.org/10.1002/anie.200603392

Federici, T., Liu, J. K., Teng, Q., Yang, J., & Boulis, N. M. (2007). A means for targeting therapeutics to peripheral nervous system neurons with axonal damage. *Neurosurgery*, *60*(5), 911–8; discussion 911–8. Retrieved from http://www.ncbi.nlm.nih.gov/pubmed/17460527

Flory, J. D., Simmons, C. R., Lin, S., Johnson, T., Andreoni, A., Zook, J., … Fromme, P. (2014). Low Temperature Assembly of Functional 3D DNA-PNA-Protein Complexes. *Journal of the American Chemical Society*, *136*(23), 8283–8295. http://doi.org/10.1021/ja501228c

Fu, T. J., & Seeman, N. C. (1993). DNA double-crossover molecules. *Biochemistry*, *32*(13), 3211–3220. http://doi.org/10.1021/bi00064a003

Goodman, R. P., Schaap, I. A. T., Tardin, C. F., Erben, C. M., Berry, R. M., Schmidt, C. F., & Turberfield, A. J. (2005). Rapid Chiral Assembly of Rigid DNA Building Blocks for Molecular Nanofabrication. *Science*, *310*(5754), 1661–1665. http://doi.org/10.1126/science.1120367

Greene, D. G., Keum, J.-W., & Bermudez, H. (2012). The Role of Defects on the Assembly and Stability of DNA Nanostructures. *Small*, *8*(9), 1320–1325. http://doi.org/10.1002/smll.201102221

Hamblin, G. D., Carneiro, K. M. M., Fakhoury, J. F., Bujold, K. E., & Sleiman, H. F. (2012). Rolling Circle Amplification-Templated DNA Nanotubes Show Increased Stability and Cell Penetration Ability. *Journal of the American Chemical Society*, *134*(6), 2888–2891. http://doi.org/10.1021/ja2107492

Han, D., Pal, S., Nangreave, J., Deng, Z., Liu, Y., & Yan, H. (2011). DNA Origami with Complex Curvatures in Three-Dimensional Space. *Science*, *332*(6027), 342 LP – 346. Retrieved from http://science.sciencemag.org/content/332/6027/342.abstract

Haque, S., Md, S., Alam, M. I., Sahni, J. K., Ali, J., & Baboota, S. (2012). Nanostructure-based drug delivery systems for brain targeting. *Drug Development and Industrial Pharmacy*, *38*(4), 387–411. Retrieved from http://www.ncbi.nlm.nih.gov/pubmed/21954902

Haramati, S., Chapnik, E., Sztainberg, Y., Eilam, R., Zwang, R., Gershoni, N., … Hornstein, E. (2010). miRNA malfunction causes spinal motor neuron disease. *Proceedings of the National Academy of Sciences of the United States of America*, *107*(29), 13111–13116. http://doi.org/10.1073/pnas.1006151107

He, Y., Tian, Y., Chen, Y., Deng, Z., Ribbe, A. E., & Mao, C. (2005). Sequence Symmetry as a Tool for Designing DNA Nanostructures. *Angewandte Chemie*, *117*(41), 6852–6854. Retrieved from http://doi.wiley.com/10.1002/ange.200502193

He, Y., Ye, T., Su, M., Zhang, C., Ribbe, A. E., Jiang, W., & Mao, C. (2008). Hierarchical self-assembly of DNA into symmetric supramolecular polyhedra. *Nature*, *452*(7184), 198–201. Retrieved from http://dx.doi.org/10.1038/nature06597

Hernandez-Chan, N. G., Bannon, M. J., Orozco-Barrios, C. E., Escobedo, L., Zamudio, S., De la Cruz, F., … Martinez-Fong, D. (2015). Neurotensin-polyplex-mediated brain-derived neurotrophic factor gene delivery into nigral dopamine neurons prevents nigrostriatal degeneration in a rat model of early Parkinson's disease. *Journal of Biomedical Science*, *22*(1), 59. http://doi.org/10.1186/s12929-015-0166-7

Jiang, D., Sun, Y., Li, J., Li, Q., Lv, M., Zhu, B., … Fan, C. (2016). Multiple-Armed Tetrahedral DNA Nanostructures for Tumor-Targeting, Dual-Modality in Vivo Imaging. *ACS Applied Materials & Interfaces*, *8*(7), 4378–4384. http://doi.org/10.1021/acsami.5b10792

Kabu, S., Gao, Y., Kwon, B. K., & Labhasetwar, V. (2015). Drug delivery, cell-based therapies, and tissue engineering approaches for spinal cord injury. *Journal of Controlled Release*, *219*, 141–154. http://doi.org/http://dx.doi.org/10.1016/j.jconrel.2015.08.060

Kam, L., Shain, W., Turner, J. N., & Bizios, R. (2001). Axonal outgrowth of hippocampal neurons on micro-scale networks of polylysine-conjugated laminin. *Biomaterials*, *22*(10), 1049–1054. http://doi.org/http://dx.doi.org/10.1016/S0142-9612(00)00352-5

Keum, J.-W., Ahn, J.-H., & Bermudez, H. (2011). Design, Assembly, and Activity of Antisense DNA Nanostructures. *Small*, *7*(24), 3529–3535. http://doi.org/10.1002/smll.201101804

Keum, J.-W., & Bermudez, H. (2012). DNA-based delivery vehicles: pH-controlled disassembly and cargo release. *Chemical Communications (Cambridge, England)*, *48*(99), 12118–12120. http://doi.org/10.1039/c2cc37471d

Kim, J., Inoue, K., Ishii, J., Vanti, W. B., Voronov, S. V, Murchison, E., … Abeliovich, A. (2007). A microRNA feedback circuit in midbrain dopamine neurons. *Science (New York, N.Y.)*, *317*(5842), 1220–1224. http://doi.org/10.1126/science.1140481

Kim, K.-R., Kim, D.-R., Lee, T., Yhee, J. Y., Kim, B.-S., Kwon, I. C., & Ahn, D.-R. (2013). Drug delivery by a self-assembled DNA tetrahedron for overcoming drug resistance in breast cancer cells. *Chemical Communications*, *49*(20), 2010–2012. http://doi.org/10.1039/C3CC38693G

Kim, Y., Sohn, D., & Tan, W. (2008). Molecular Beacons in Biomedical Detection and Clinical Diagnosis. *International Journal of Clinical and Experimental Pathology*, *1*(2), 105–116. Retrieved from http://www.ncbi.nlm.nih.gov/pmc/articles/PMC2480550/

Krishnan, Y., & Simmel, F. C. (2011). Nucleic Acid Based Molecular Devices. *Angewandte Chemie International Edition*, *50*(14), 3124–3156. http://doi.org/10.1002/anie.200907223

Kumar, A., & Singh, A. (2015). A review on Alzheimer's disease pathophysiology and its management: an update. *Pharmacological Reports*, *67*(2), 195–203. Retrieved from http://www.sciencedirect.com/science/article/pii/S1734114014002886

Kwon, E. J., Lasiene, J., Jacobson, B., Park, I.-K., Horner, P. J., & Pun, S. H. (2010). Targeted nonviral delivery vehicles to neural progenitor cells in the mouse subventricular zone. *Biomaterials*, *31*(8), 2417. http://doi.org/10.1016/j.biomaterials.2009.11.086

LaBean, T. H., Yan, H., Kopatsch, J., Liu, F., Winfree, E., Reif, J. H., & Seeman, N. C. (2000). Construction, Analysis, Ligation, and Self-Assembly of DNA Triple Crossover Complexes. *Journal of the American Chemical Society*, *122*(9), 1848–1860. http://doi.org/10.1021/ja993393e

Langecker, M., Arnaut, V., Martin, T. G., List, J., Renner, S., Mayer, M., … Simmel, F. C. (2012). Synthetic Lipid Membrane Channels Formed by Designed DNA Nanostructures. *Science* , *338* (6109), 932–936. http://doi.org/10.1126/science.1225624

Lanier, L. A., & Bermudez, H. (2015). DNA nanostructures: a shift from assembly to applications. *Current Opinion in Chemical Engineering*, *7*, 93–100. Retrieved from http://www.sciencedirect.com/science/article/pii/S2211339815000027

Lee, H., Lytton-Jean, A. K. R., Chen, Y., Love, K. T., Park, A. I., Karagiannis, E. D., … Anderson, D. G. (2012). Molecularly self-assembled nucleic acid nanoparticles for targeted in vivo siRNA delivery. *Nat Nano*, *7*(6), 389–393. Retrieved from http://dx.doi.org/10.1038/nnano.2012.73

Leitner, M., Mitchell, N., Kastner, M., Schlapak, R., Gruber, H. J., Hinterdorfer, P., … Ebner, A. (2011). Single-Molecule AFM Characterization of Individual Chemically Tagged DNA Tetrahedra. *ACS Nano*, *5*(9), 7048–7054. http://doi.org/10.1021/nn201705p

Levine, M. N., Hoang, T. T., & Raines, R. T. (2013). Fluorogenic Probe for Constitutive Cellular Endocytosis. *Chemistry & Biology*, *20*(4), 614–618. http://doi.org/10.1016/j.chembiol.2013.03.016

Li, J., Pei, H., Zhu, B., Liang, L., Wei, M., He, Y., … Fan, C. (2011). Self-Assembled Multivalent DNA Nanostructures for Noninvasive Intracellular Delivery of Immunostimulatory CpG Oligonucleotides. *ACS Nano*, *5*(11), 8783–8789. http://doi.org/10.1021/nn202774x

Li, X., Zhang, C., Hao, C., Tian, C., Wang, G., & Mao, C. (2012). DNA Polyhedra with T-Linkage. *ACS Nano*, *6*(6), 5138–5142. http://doi.org/10.1021/nn300813w

Liang, L., Li, J., Li, Q., Huang, Q., Shi, J., Yan, H., & Fan, C. (2014). Single-Particle Tracking and Modulation of Cell Entry Pathways of a Tetrahedral DNA Nanostructure in Live Cells. *Angewandte Chemie International Edition*, *53*(30), 7745–7750. http://doi.org/10.1002/anie.201403236

Liu, D., Park, S. H., Reif, J. H., & LaBean, T. H. (2004). DNA nanotubes self-assembled from triple-crossover tiles as templates for conductive nanowires. *Proceedings of the National Academy of Sciences of the United States of America* , *101* (3), 717–722. http://doi.org/10.1073/pnas.0305860101

Liu, J. K., Teng, Q., Garrity-Moses, M., Federici, T., Tanase, D., Imperiale, M. J., & Boulis, N. M. (2005). A novel peptide defined through phage display for therapeutic protein and vector neuronal targeting. *Neurobiology of Disease*, *19*(3), 407–18. Retrieved from http://www.ncbi.nlm.nih.gov/pubmed/16023583

Long, J. M., Ray, B., & Lahiri, D. K. (2012). MicroRNA-153 Physiologically Inhibits Expression of Amyloid-β Precursor Protein in Cultured Human Fetal Brain Cells and Is Dysregulated in a Subset of Alzheimer Disease Patients. *The Journal of Biological Chemistry*, *287*(37), 31298–31310. http://doi.org/10.1074/jbc.M112.366336

Lukiw, W. J. (2007). Micro-RNA speciation in fetal, adult and Alzheimer's disease hippocampus. *NeuroReport*, *18*(3). Retrieved from http://journals.lww.com/neuroreport/Fulltext/2007/02120/Micro_RNA_speciation_in_fetal,_adult_and.20.aspx

Mangalum, A., Rahman, M., & Norton, M. L. (2013). Site-Specific Immobilization of Single-Walled Carbon Nanotubes onto Single and One-Dimensional DNA Origami. *Journal of the American Chemical Society*, *135*(7), 2451–2454. http://doi.org/10.1021/ja312191a

Mann, A. P., Scodeller, P., Hussain, S., Joo, J., Kwon, E., Braun, G. B., … Ruoslahti, E. (2016). A peptide for targeted, systemic delivery of imaging and therapeutic compounds into acute brain injuries. *Nat Commun*, *7*. Retrieved from http://dx.doi.org/10.1038/ncomms11980

Martinez-Fong, D., Navarro-Quiroga, I., Ochoa, I., Alvarez-Maya, I., Meraz, M. A., Luna, J., & Arias-Montaño, J.-A. (1999). Neurotensin-SPDP-poly-l-lysine conjugate: a nonviral vector for targeted gene delivery to neural cells. *Molecular Brain Research*, *69*(2), 249–262. http://doi.org/http://dx.doi.org/10.1016/S0169-328X(99)00114-X

McCall, R. L., Cacaccio, J., Wrabel, E., Schwartz, M. E., Coleman, T. P., & Sirianni, R. W. (2014). Pathogen-inspired drug delivery to the central nervous system. *Tissue Barriers*, *2*(4), e944449. http://doi.org/10.4161/21688362.2014.944449

Ming, X., & Laing, B. (2015). Bioconjugates for targeted delivery of therapeutic oligonucleotides. *Advanced Drug Delivery Reviews*, *87*, 81–89. http://doi.org/http://dx.doi.org/10.1016/j.addr.2015.02.002

Miñones-Moyano, E., Porta, S., Escaramís, G., Rabionet, R., Iraola, S., Kagerbauer, B., … Martí, E. (2011). MicroRNA profiling of Parkinson's disease brains identifies early downregulation of miR-34b/c which modulate mitochondrial function. *Human Molecular Genetics* , *20* (15), 3067–3078. http://doi.org/10.1093/hmg/ddr210

Miras-Portugal, M. T., Gomez-Villafuertes, R., Gualix, J., Diaz-Hernandez, J. I., Artalejo, A. R., Ortega, F., … Perez-Sen, R. (2015). Nucleotides in neuroregeneration and neuroprotection. *Neuropharmacology*. Retrieved from http://www.ncbi.nlm.nih.gov/pubmed/26359530

Mohri, K., Nishikawa, M., Takahashi, N., Shiomi, T., Matsuoka, N., Ogawa, K., … Takakura, Y. (2012). Design and Development of Nanosized DNA Assemblies in Polypod-like Structures as Efficient Vehicles for Immunostimulatory CpG Motifs to Immune Cells. *ACS Nano*, *6*(7), 5931–5940. http://doi.org/10.1021/nn300727j

Mohri, K., Nishikawa, M., Takahashi, Y., & Takakura, Y. (2014). DNA nanotechnology-based development of delivery systems for bioactive compounds. *European Journal of Pharmaceutical Sciences : Official Journal of the European Federation for Pharmaceutical Sciences*, *58*, 26–33. http://doi.org/10.1016/j.ejps.2014.03.002

Morris, P. G., & Abrey, L. E. (2009). Therapeutic challenges in primary CNS lymphoma. *The Lancet Neurology*, *8*(6), 581–592. http://doi.org/10.1016/S1474-4422(09)70091-2

Neuwelt, E. A., Bauer, B., Fahlke, C., Fricker, G., Iadecola, C., Janigro, D., … Drewes, L. R. (2011). Engaging neuroscience to advance translational research in brain barrier biology. *Nature Reviews. Neuroscience*, *12*(3), 169–82. Retrieved from http://www.pubmedcentral.nih.gov/articlerender.fcgi?artid=3335275&tool=pmcentrez&rendertype=abstract

Nickels, P. C., Ke, Y., Jungmann, R., Smith, D. M., Leichsenring, M., Shih, W. M., … Högberg, B. (2014). DNA origami structures directly assembled from intact bacteriophages. *Small (Weinheim an Der Bergstrasse, Germany)*, *10*(9), 1765–9. Retrieved from http://www.ncbi.nlm.nih.gov/pubmed/24532395

Nielsen, P. E., & Egholm, M. (1999). An Introduction to Peptide Nucleic Acid. *Current Issues Molec. Biol.*, *1*(2), 89–104.

Nielsen, P. E., Egholm, M., Berg, R. H., & Buchardt, O. (1991). Sequence-selective recognition of DNA by strand displacement with a thymine-substituted polyamide. *Science*, *254*(5037), 1497–1500. Retrieved from http://science.sciencemag.org/content/254/5037/1497.abstract

Oliveira, H., Fernandez, R., Pires, L. R., Martins, M. C. L., Simões, S., Barbosa, M. A., & Pêgo, A. P. (2010). Targeted gene delivery into peripheral sensorial neurons mediated by self-assembled vectors composed of poly(ethylene imine) and tetanus toxin fragment c. *Journal of Controlled Release*, *143*(3), 350–358. http://doi.org/http://dx.doi.org/10.1016/j.jconrel.2010.01.018

Oliveira, H., Pires, L. R., Fernandez, R., Martins, M. C. L., Simões, S., & Pêgo, A. P. (2010). Chitosan-based gene delivery vectors targeted to the peripheral nervous system. *Journal of Biomedical Materials Research Part A*, *95A*(3), 801–810. http://doi.org/10.1002/jbm.a.32874

Ortega, F. G., Fernández-Baldo, M. A., Fernández, J. G., Serrano, M. J., Sanz, M. I., Diaz-Mochón, J. J., … Raba, J. (2015). Study of antitumor activity in breast cell lines using silver nanoparticles produced by yeast. *International Journal of Nanomedicine*, *10*, 2021–2031. http://doi.org/10.2147/IJN.S75835

Østergaard, M. E., Thomas, G., Koller, E., Southwell, A. L., Hayden, M. R., & Seth, P. P. (2015). Biophysical and Biological

Characterization of Hairpin and Molecular Beacon RNase H Active Antisense Oligonucleotides. *ACS Chemical Biology*, *10*(5), 1227–1233. http://doi.org/10.1021/cb500880f

Ouyang, Y.-B., Xu, L., Yue, S., Liu, S., & Giffard, R. G. (2014). Neuroprotection by astrocytes in brain ischemia: importance of microRNAs. *Neuroscience Letters*, *565*, 53–8. Retrieved from http://www.sciencedirect.com/science/article/pii/S030439401301015X

Pardridge, W. M. (2005). Molecular biology of the blood-brain barrier. *Molecular Biotechnology*, *30*(1), 57–70. Retrieved from http://www.ncbi.nlm.nih.gov/pubmed/15805577

Pardridge, W. M. (2012). Drug transport across the blood-brain barrier. *J Cereb Blood Flow Metab*, *32*(11), 1959–1972. http://doi.org/10.1038/jcbfm.2012.126

Park, I.-K., Lasiene, J., Chou, S.-H., Horner, P. J., & Pun, S. H. (2007). Neuron-specific delivery of nucleic acids mediated by Tet1-modified poly(ethylenimine). *The Journal of Gene Medicine*, *9*(8), 691–702. http://doi.org/10.1002/jgm.1062

Platanias, L. C. (2005). Mechanisms of type-I- and type-II-interferon-mediated signalling. *Nat Rev Immunol*, *5*(5), 375–386. Retrieved from http://dx.doi.org/10.1038/nri1604

Powell, S. K., Rao, J., Roque, E., Nomizu, M., Kuratomi, Y., Yamada, Y., & Kleinman, H. K. (2000). Neural cell response to multiple novel sites on laminin-1. *Journal of Neuroscience Research*, *61*(3), 302–312. http://doi.org/10.1002/1097-4547(20000801)61:3<302::AID-JNR8>3.0.CO;2-G

Ralph, G. S., Radcliffe, P. A., Day, D. M., Carthy, J. M., Leroux, M. A., Lee, D. C. P., … Azzouz, M. (2005). Silencing mutant SOD1 using RNAi protects against neurodegeneration and extends survival in an ALS model. *Nat Med*, *11*(43), 429–433. Retrieved from http://dx.doi.org/10.1038/nm1205

Ray, A., & Nordén, B. (2000). Peptide nucleic acid (PNA): its medical and biotechnical applications and promise for the future. *The FASEB Journal*, *14*(9), 1041–1060. Retrieved from http://www.fasebj.org/content/14/9/1041.abstract

Rende, M., Giambanco, I., Buratta, M., & Tonali, P. (1995). Axotomy induces a different modulation of both low-affinity nerve growth factor receptor and choline acetyltransferase between adult rat spinal and brainstem motoneurons. *The Journal of Comparative Neurology*, *363*(2), 249–263. http://doi.org/10.1002/cne.903630207

Rinker, S., Ke, Y., Liu, Y., Chhabra, R., & Yan, H. (2008). Self-assembled DNA nanostructures for distance-dependent multivalent ligand-protein binding. *Nat Nano*, *3*(7), 418–422. Retrieved from http://dx.doi.org/10.1038/nnano.2008.164

Rogers, M.-L., Smith, K. S., Matusica, D., Fenech, M., Hoffman, L., Rush, R. A., & Voelcker, N. H. (2014). Non-viral gene therapy that targets motor neurons in vivo. *Frontiers in Molecular Neuroscience*, *7*, 80. http://doi.org/10.3389/fnmol.2014.00080

Rothemund, P. W. K. (2006). Folding DNA to create nanoscale shapes and patterns. *Nature*, *440*(7082), 297–302. Retrieved from http://dx.doi.org/10.1038/nature04586

Ruigrok, M. J. R., & de Lange, E. C. M. (2015). Emerging Insights for Translational Pharmacokinetic and Pharmacokinetic-Pharmacodynamic Studies: Towards Prediction of Nose-to-Brain Transport in Humans. *The AAPS Journal*, *17*(3), 493–505. http://doi.org/10.1208/s12248-015-9724-x

Saccà, B., & Niemeyer, C. M. (2012). DNA origami: the art of folding DNA. *Angewandte Chemie (International Ed. in English)*, *51*(1), 58–66. Retrieved from http://www.ncbi.nlm.nih.gov/pubmed/22162047

Saxena, S., & Caroni, P. (2011). Selective neuronal vulnerability in neurodegenerative diseases: from stressor thresholds to degeneration. *Neuron*, *71*(1), 35–48. Retrieved from http://www.cell.com/article/S0896627311005617/fulltext

Schapira, A. H. V, Olanow, C. W., Greenamyre, J. T., & Bezard, E. (2014). Slowing of neurodegeneration in Parkinson's disease and Huntington's disease: future therapeutic perspectives. *Lancet (London, England)*, *384*(9942), 545–55. Retrieved from http://www.thelancet.com/article/S0140673614610102/fulltext

Schulze, E. T., Geary, E. K., Susmaras, T. M., Paliga, J. T., Maki, P. M., & Little, D. M. (2011). Anatomical correlates of age-related working memory declines. *Journal of Aging Research*, *2011*, 606871. Retrieved from http://www.pubmedcentral.nih.gov/articlerender.fcgi?artid=3228338&tool=pmcentrez&rendertype=abstract

Seeburger, J. L., Tarras, S., Natter, H., & Springer, J. E. (1993). Spinal cord motoneurons express p75NGFR and p145trkB mRNA in amyotrophic lateral sclerosis. *Brain Research*, *621*(1), 111–115. http://doi.org/http://dx.doi.org/10.1016/0006-8993(93)90304-6

Seeman, N. C. (1982). Nucleic acid junctions and lattices. *Journal of Theoretical Biology*, *99*(2), 237–247. Retrieved from http://www.sciencedirect.com/science/article/pii/0022519382900029

Seeman, N. C. (1990). De Novo Design of Sequences for Nucleic Acid Structural Engineering. *Journal of Biomolecular Structure and Dynamics*, *8*(3), 573–581. http://doi.org/10.1080/07391102.1990.10507829

Seeman, N. C. (2010). Nanomaterials Based on DNA. *Annual Review of Biochemistry*, *79*, 65–87. http://doi.org/10.1146/annurevbiochem-060308-102244

Sepramaniam, S., Tan, J.-R., Tan, K.-S., DeSilva, D. A., Tavintharan, S., Woon, F.-P., … Jeyaseelan, K. (2014). Circulating MicroRNAs as Biomarkers of Acute Stroke. *International Journal of Molecular Sciences*, *15*(1), 1418–1432. http://doi.org/10.3390/ijms15011418

Setyawati, M. I., Kutty, R. V., Tay, C. Y., Yuan, X., Xie, J., & Leong, D. T. (2014). Novel Theranostic DNA Nanoscaffolds for the Simultaneous Detection and Killing of Escherichia coli and Staphylococcus aureus. *ACS Applied Materials & Interfaces*, *6*(24), 21822–21831. http://doi.org/10.1021/am502591c

Shapiro, R. E., Specht, C. D., Collins, B. E., Woods, A. S., Cotter, R. J., & Schnaar, R. L. (1997). Identification of a Ganglioside Recognition Domain of Tetanus Toxin Using a Novel Ganglioside Photoaffinity Ligand. *Journal of Biological Chemistry* , *272* (48), 30380–30386. http://doi.org/10.1074/jbc.272.48.30380

Shen, X., Jiang, Q., Wang, J., Dai, L., Zou, G., Wang, Z.-G., … Ding, B. (2012). Visualization of the intracellular location and stability of DNA origami with a label-free fluorescent probe. *Chemical Communications*, *48*(92), 11301–11303. http://doi.org/10.1039/C2CC36185J

Shen, Z., Yan, H., Wang, T., & Seeman, N. C. (2004). Paranemic Crossover DNA: A Generalized Holliday Structure with Applications in Nanotechnology. *Journal of the American Chemical Society*, *126*(6), 1666–1674. http://doi.org/10.1021/ja038381e

Shvartsman, D., Storrie-White, H., Lee, K., Kearney, C., Brudno, Y., Ho, N., … Mooney, D. J. (2014). Sustained Delivery of VEGF Maintains Innervation and Promotes Reperfusion in Ischemic Skeletal Muscles Via NGF/GDNF Signaling. *Mol Ther*, *22*(7), 1243–1253. Retrieved from http://dx.doi.org/10.1038/mt.2014.76

Singer, O., Marr, R. A., Rockenstein, E., Crews, L., Coufal, N. G., Gage, F. H., … Masliah, E. (2005). Targeting BACE1 with siRNAs ameliorates Alzheimer disease neuropathology in a transgenic model. *Nat Neurosci*, *8*(10), 1343–1349. Retrieved from http://dx.doi.org/10.1038/nn1531

Smith, D., Schüller, V., Engst, C., Rädler, J., & Liedl, T. (2013). Nucleic acid nanostructures for biomedical applications. *Nanomedicine (London, England)*, *8*(1), 105–21. Retrieved from http://www.ncbi.nlm.nih.gov/pubmed/23256495

Suburo, A. M., Wheatley, S. C., Horn, D. A., Gibson, S. J., Jahn, R., Fischer-Colbrie, R., … Polak, J. M. (1992). Intracellular redistribution of neuropeptides and secretory proteins during differentiation of neuronal cell lines. *Neuroscience*, *46*(4), 881–889. http://doi.org/http://dx.doi.org/10.1016/0306-4522(92)90191-4

Tay, C. Y., Yuan, L., & Leong, D. T. (2015). Nature-Inspired DNA Nanosensor for Real-Time in Situ Detection of mRNA in Living Cells. *ACS Nano*, *9*(5), 5609–5617. http://doi.org/10.1021/acsnano.5b01954

Tintoré, M., Eritja, R., & Fábrega, C. (2014). DNA nanoarchitectures: steps towards biological applications. *Chembiochem : A European Journal of Chemical Biology*, *15*(10), 1374–90. Retrieved from http://www.ncbi.nlm.nih.gov/pubmed/24953971

Townsend, S. A., Evrony, G. D., Gu, F. X., Schulze, M. P., Brown, R. H., & Langer, R. S. (2007). Tetanus toxin C fragment conjugated nanoparticles for targeted drug delivery to neurons. *Biomaterials*, *28*(34), 5176–5184. http://doi.org/10.1016/j.biomaterials.2007.08.011

Tyagi, S., & Kramer, F. R. (1996). Molecular Beacons: Probes that Fluoresce upon Hybridization. *Nat Biotech*, *14*(3), 303–308. Retrieved from http://dx.doi.org/10.1038/nbt0396-303

Walsh, A. S., Yin, H., Erben, C. M., Wood, M. J. A., & Turberfield, A. J. (2011). DNA Cage Delivery to Mammalian Cells. *ACS Nano*, *5*(7), 5427–5432. http://doi.org/10.1021/nn2005574

Wang, K., Park, J. O., & Zhang, M. (2013). Treatment of glioblastoma multiforme using combination of siRNA targeting EGFR and β-catenin. *The Journal of Gene Medicine*, *15*(1), 42–50. http://doi.org/10.1002/jgm.2693

Wang, K., Tang, Z., Yang, C. J., Kim, Y., Fang, X., Li, W., … Tan, W. (2009). Molecular Engineering of DNA: Molecular Beacons. *Angewandte Chemie (International Ed. in English)*, *48*(5), 856–870. http://doi.org/10.1002/anie.200800370

Watson, J. D., & Crick, F. H. C. (1974). Molecular Structure of Nucleic Acids: A Structure for Deoxyribose Nucleic Acid. *Nature*, *248*(5451), 765. Retrieved from http://dx.doi.org/10.1038/248765a0

Wen, Y., Pei, H., Shen, Y., Xi, J., Lin, M., Lu, N., … Fan, C. (2012). DNA Nanostructure-based Interfacial engineering for PCR-free ultrasensitive electrochemical analysis of microRNA. *Scientific Reports*, *2*, 867. Retrieved from http://dx.doi.org/10.1038/srep00867

Westphal, M., Hilt, D. C., Bortey, E., Delavault, P., Olivares, R., Warnke, P. C., … Ram, Z. (2003). A phase 3 trial of local chemotherapy with biodegradable carmustine (BCNU) wafers (Gliadel wafers) in patients with primary malignant glioma. *Neuro-Oncology*, *5*(2), 79–88. http://doi.org/10.1215/S1522-8517-02-00023-6

Whitehead, K. A., Langer, R., & Anderson, D. G. (2009). Knocking down barriers: advances in siRNA delivery. *Nature Reviews. Drug Discovery*, *8*(2), 129–38. Retrieved from http://dx.doi.org/10.1038/nrd2742

Williams, S., Lund, K., Lin, C., Wonka, P., Lindsay, S., & Yan, H. (2009). DNA Computing. In A. Goel, F. C. Simmel, & P. Sosík (Eds.), *DNA Computing* (pp. 90–101). Berlin, Heidelberg: Springer-Verlag. http://doi.org/10.1007/978-3-642-03076-5_8

Wood, J. N., Bevan, S. J., Coote, P. R., Dunn, P. M., Harmar, A., Hogan, P., … Wheatley, S. (1990). Novel Cell Lines Display Properties of Nociceptive Sensory Neurons. *Proceedings of the Royal Society of London B: Biological Sciences*, *241*(1302), 187–194. Retrieved from http://rspb.royalsocietypublishing.org/content/241/1302/187.abstract

Wu, J., & Chen, Z. J. (2014). Innate Immune Sensing and Signaling of Cytosolic Nucleic Acids. *Annual Review of Immunology*, *32*(1), 461–488. http://doi.org/10.1146/annurev-immunol-032713-120156

Xia, Z., Wang, P., Liu, X., Liu, T., Yan, Y., Yan, J., … He, D. (2016). Tumor-Penetrating Peptide-Modified DNA Tetrahedron for Targeting Drug Delivery. *Biochemistry*, *55*(9), 1326–1331. http://doi.org/10.1021/acs.biochem.5b01181

Xie, N., Huang, J., Yang, X., Yang, Y., Quan, K., Wang, H., … Wang, K. (2016). A DNA tetrahedron-based molecular beacon for tumor-related mRNA detection in living cells. *Chemical Communications*, *52*(11), 2346–2349. http://doi.org/10.1039/C5CC09980C

Yang, Y., Han, D., Nangreave, J., Liu, Y., & Yan, H. (2012). DNA Origami with Double Stranded DNA as a Unified Scaffold. *ACS Nano*, *6*(9), 8209–8215. http://doi.org/10.1021/nn302896c

Yang, Z.-Z., Zhang, Y.-Q., Wang, Z.-Z., Wu, K., Lou, J.-N., & Qi, X.-R. (2013). Enhanced brain distribution and pharmacodynamics of rivastigmine by liposomes following intranasal administration. *International Journal of Pharmaceutics*, *452*(1–2), 344–354. http://doi.org/http://dx.doi.org/10.1016/j.ijpharm.2013.05.009

Yuan, A., Rao, M. V, Veeranna, & Nixon, R. A. (2012). Neurofilaments at a glance. *Journal of Cell Science*, *125*(14), 3257–3263. Retrieved from http://jcs.biologists.org/content/125/14/3257.abstract

Zadeh, J. N., Steenberg, C. D., Bois, J. S., Wolfe, B. R., Pierce, M. B., Khan, A. R., … Pierce, N. A. (2011). NUPACK: Analysis and design of nucleic acid systems. *Journal of Computational Chemistry*, *32*(1), 170–173. http://doi.org/10.1002/jcc.21596

Zhang, B., & Farwell, M. A. (2008). microRNAs: a new emerging class of players for disease diagnostics and gene therapy. *Journal of Cellular and Molecular Medicine*, *12*(1), 3–21. http://doi.org/10.1111/j.1582-4934.2007.00196.x

Zhang, D. Y., & Seelig, G. (2011). Dynamic DNA nanotechnology using strand-displacement reactions. *Nat Chem*, *3*(2), 103–113. Retrieved from http://dx.doi.org/10.1038/nchem.957

Zhang, H., Chao, J., Pan, D., Liu, H., Huang, Q., & Fan, C. (2012). Folding super-sized DNA origami with scaffold strands from long-range PCR. *Chemical Communications*, *48*(51), 6405–6407. http://doi.org/10.1039/C2CC32204H

Zhang, Q., Jiang, Q., Li, N., Dai, L., Liu, Q., Song, L., … Du, Y. (2014). DNA Origami as an In Vivo Drug Delivery Vehicle for Cancer Therapy. *ACS Nano*, *8*(7), 6633–6643. http://doi.org/10.1021/nn502058j

Zhao, Y.-X., Shaw, A., Zeng, X., Benson, E., Nyström, A. M., & Högberg, B. (2012). DNA Origami Delivery System for Cancer Therapy with Tunable Release Properties. *ACS Nano*, *6*(10), 8684–8691. http://doi.org/10.1021/nn3022662

Zhu, G., Zheng, J., Song, E., Donovan, M., Zhang, K., Liu, C., & Tan, W. (2013). Self-assembled, aptamer-tethered DNA nanotrains for targeted transport of molecular drugs in cancer theranostics. *Proceedings of the National Academy of Sciences of the United States of America*, *110*(20), 7998–8003. http://doi.org/10.1073/pnas.1220817110

Zhu, J., Feng, X., Lou, J., Li, W., Li, S., Zhu, H., … Li, C. (2013). Accurate Quantification of microRNA via Single Strand Displacement Reaction on DNA Origami Motif. *PLoS ONE*, *8*(8), e69856. Retrieved from http://dx.doi.org/10.1371%2Fjournal.pone.0069856

Zhu, J., Wei, B., Yuan, Y., & Mi, Y. (2009). UNIQUIMER 3D, a software system for structural DNA nanotechnology design, analysis and evaluation. *Nucleic Acids Research*, *37*(7), 2164–2175. http://doi.org/10.1093/nar/gkp005